
# BRNO UNIVERSITY OF TECHNOLOGY
VYSOKÉ UČENÍ TECHNICKÉ V BRNĚ

## FACULTY OF ELECTRICAL ENGINEERING AND COMMUNICATION
FAKULTA ELEKTROTECHNIKY
A KOMUNIKAČNÍCH TECHNOLOGIÍ

## DEPARTMENT OF CONTROL AND INSTRUMENTATION
ÚSTAV AUTOMATIZACE A MĚŘICÍ TECHNIKY


# AUTONOMOUS ROBOTIC GAMMA RADIATION MEASUREMENT
AUTONOMNÍ ROBOTICKÉ MĚŘENÍ ZÁŘENÍ GAMA

**MASTER'S THESIS**
DIPLOMOVÁ PRÁCE


**AUTHOR** — **Bc. Tomáš Lázna**
AUTOR PRÁCE

**SUPERVISOR** — **prof. Ing. Luděk Žalud, Ph.D.**
VEDOUCÍ PRÁCE



**BRNO 2017**

BRNO UNIVERSITY OF TECHNOLOGY
FACULTY OF ELECTRICAL ENGINEERING AND COMMUNICATION

# Master's Thesis

Master's study field **Cybernetics, Control and Measurements**
Department of Control and Instrumentation

***Student:*** Bc. Tomáš Lázna ***ID:*** 155192
***Year of study:*** 2 ***Academic year:*** 2016/17

**TITLE OF THESIS:**

## Autonomous Robotic Gamma Radiation Measurement

**INSTRUCTION:**

1. Get acquainted with a measurement of ionizing radiation, especially measurement of a gamma radiation. Concern yourself also with direction-sensitive sensors of gamma radiation in order to manage faster scanning of the area of interest.
2. Propose methods for utilization of existing sensors of gamma radiation (including the direction-sensitive ones) for fully autonomous localization of radiation sources and for mapping the area of interest.
3. Test the selected methods in simulator at first and also in real experiments with real radiation sources if it is feasible (consult with your supervisor).
4. Compare the methods and compare also the simulation results with results in real conditions. Discuss the effect of direction-sensitive detection on speed of the source localization.

**REFERENCE:**

Gamma Radiation, Edited by Feriz Adrovic, ISBN 978-953-51-0316-5, 332 pages, Publisher: InTech, Chapters published March 21, 2012

***Assigment deadline:*** 6. 2. 2017 ***Submission deadline:*** 15.5.2017

***Head of thesis:*** prof. Ing. Luděk Žalud, Ph.D.
***Consultant:***

**doc. Ing. Václav Jirsík, CSc.**
Subject Council chairman

VYSOKÉ UČENÍ TECHNICKÉ V BRNĚ
Fakulta elektrotechniky a komunikačních technologií
Ústav automatizace a měřicí techniky

**WARNING:**

The author of this Master's Thesis claims that by creating this thesis he/she did not infringe the rights of third persons and the personal and/or property rights of third persons were not subjected to derogatory treatment. The author is fully aware of the legal consequences of an infringement of provisions as per Section 11 and following of Act No 121/2000 Coll. on copyright and rights related to copyright and on amendments to some other laws (the Copyright Act) in the wording of subsequent directives including the possible criminal consequences as resulting from provisions of Part 2, Chapter VI, Article 4 of Criminal Code 40/2009 Coll.

## ABSTRACT

This thesis focuses on autonomous localization of radiological sources in a defined area of interest. Its aim is to develop localization strategies and a platform on which they can be tested. The platform is based on reconnaissance robot Orpheus-X3, scintillation detectors and a precise GNSS receiver. Algorithm for creating a radiation distribution map is extended. New methods based on directional sensitivity of proposed detection system are introduced. Initial exploration of the area of interest is done by using circular trajectories. All algorithms are tested both by simulation and real experiments. The achieved precision of localization is in order of tens of centimeters. Time efficiency is increased approximately two to five times by applying new algorithms. One of the contributions of the thesis is a development of a modular system that could be transferred and adjusted to different platforms. The advantage of the used system is a high degree of autonomy and safety for a human operator.



## KEYWORDS

gamma radiation, scintillation detectors, robotic system, RTK-GNSS, directional sensitivity, radiation filed mapping, radiation source localization



## ABSTRAKT

Tato práce se zaměřuje na autonomní lokalizaci radiologických zdrojů v definované oblasti zájmu. Jejím cílem je vyvinout lokalizační strategie a platformu, na které je bude možné vyzkoušet. Platforma je sestavena z průzkumného robotu Orpheus-X3, scintilačních detektorů a přesného GNSS přijímače. Algoritmus pro vytváření mapy distribuce radiačního pole je rozšířen. Jsou představeny nové metody založené na směrové citlivosti navrhovaného detekčního systému. Počáteční průzkum oblasti zájmu je uskutečněn pomocí kružnicových trajektorií. Všechny algoritmy byly otestována jak simulacemi, tak reálnými experimenty. Dosažená přesnosti lokalizace je v řádu desítek centimetrů. Časová efektivita je použitím nových algoritmů zvýšena přibližně dvakrát až pětkrát. Jedním z přínosů práce je vývoj modulárního systému, který může být přesunut a uzpůsoben na jiné platformy. Výhodou použitého systému je vysoký stupeň autonomie a bezpečnost pro lidského operátora.



## KLÍČOVÁ SLOVA

gama záření, scintilační detektory, robotický systém, RTK-GNSS, směrová citlivost, mapování radiačního pole, lokalizace zdrojů záření

LÁZNA, Tomáš *Autonomous Robotic Gamma Radiation Measurement*: master's thesis. Brno: Brno University of Technology, Faculty of Electrical Engineering and Communication, Department of Control and Instrumentation, 2017. 100 p. Supervised by prof. Ing. Luděk Žalud, Ph.D.



Vysázeno pomocí balíčku `thesis` verze 2.61; `http://latex.feec.vutbr.cz`

# DECLARATION

I declare that I have written my master's thesis on the theme of "Autonomous Robotic Gamma Radiation Measurement" independently, under the guidance of the master's thesis supervisor and using the technical literature and other sources of information which are all cited in the thesis and detailed in the list of literature at the end of the thesis.

As the author of the master's thesis I furthermore declare that, as regards the creation of this master's thesis, I have not infringed any copyright. In particular, I have not unlawfully encroached on anyone's personal and/or ownership rights and I am fully aware of the consequences in the case of breaking Regulation § 11 and the following of the Copyright Act No 121/2000 Sb. of the Czech Republic, and of the rights related to intellectual property right and changes in some Acts (Intellectual Property Act) and formulated in later regulations, inclusive of the possible consequences resulting from the provisions of Criminal Act No 40/2009 Sb. of the Czech Republic, Section 2, Head VI, Part 4.

Brno ..... .....

author's signature

## ACKNOWLEDGEMENT

I would like to express my gratitude to my supervisor prof. Ing. Luděk Žalud, Ph.D. for the useful comments, remarks and engagement. I would also like to thank to other members of the Group of Robotics and AI, especially Ing. Tomáš Jílek, Ph.D. and Ing. Petr Gábrlík. Tomáš helped me with the setup of Orpheus, and above all he kept the self-localization and navigation modules working. Petr spent a lot of time drinking coffee with me and discussing my research. Both Tomáš and Petr participated in the preparation of experiments on site. Furthermore, I have to thank to Ing. Karel Katovský, Ph.D. and Ing. Jan Varmuža. They taught me much about ionizing radiation and they always made time to provide and setup radiological sources for realized experiments. A huge thank belongs to doc. Ing. Petr Sládek, Ph.D. who lend me necessary equipment for measurement. He also gave me a lot of excellent ideas. I must not forget to mention my parents and friends who have been a huge support to me. Finally, I thank to Mgr. Eva Juhasová for language correction of thesis. There are many other people who helped and supported me, and I am not able to name them all in this short acknowledgement but I am thankful to them too.


Brno ..... .....

author's signature

# CONTENTS

# LIST OF FIGURES

# LIST OF TABLES

# INTRODUCTION

In these days, new challenges occur on a daily basis. Means of the modern warfare suggest that chemical, biological, radiological and nuclear (CBRN) defense [1] will have increasing importance. The U. S. Department of Health and Human Services defines several types of terrorist attacks which involve sources of ionizing radiation [2]. One of them which is discussed in world media is a 'dirty bomb' attack [3], [4]. Such bomb may disperse radioactive material in urban zones. Since the radiological sources are commonly present in medical or scientific facilities, it is rather possible for an attacker to get them [5]. If this critical situation actually happened, it would be vital to localize and dispose of the dangerous sources as quickly as possible.

Methods for localization of radiological sources described in [6], [7], [8] and [9] utilize a network of detectors and statistical models. Their disadvantage is the immobility of detectors, hence they may not be applied very fast in a larger area. It is more convenient to mount detectors on a mobile platform. Among other disadvantages, there is a fact that the methods were tested only in simulations, not in real environment. Papers [10] and [11] introduce systems based on unmanned aerial vehicles (drones) carrying detectors. This approach enables swift exploration of the area of interest, disregarding terrain obstacles, but there is a problem with limited load of the UAVs. The higher is their distance from sources located on a terrain level, the larger volume and therefore weight of detectors is needed. Also the precision of localization is limited. There is a possibility to use a different type of airborne system, for example a helicopter [12].

Another way is to use unmanned ground vehicles, specifically reconnaissance robots. Such solution is proposed in this thesis. In comparison with a human, the robot is less prone to radiation damage and is therefore more suitable for the described type of mission. It is likely that a robot equipped with precise instrumentation locates radiological sources faster, more precisely and more safely in the first place. Some localization algorithms are suggested in [13] but the system is designed and tested in a very small area (60x60 cm). System for localization in real conditions can be found in [14]. The disadvantage is its considerably limited autonomy.

The primary aim of this thesis is to develop and test algorithms for fully autonomous localization of radiological sources in defined area of interest. The first objective is a background research of detection principles in order to choose suitable detectors. The next objective is a development of complex system based on robotic platform that would allow to run the algorithms. It should provide directional sensitivity of the sensory system which may represent an advantage for localization. All the algorithms need to be tested in simulations first. The final objective is an evaluation of proposed algorithms in actual conditions with real radiological sources.

# 1 DETECTION OF GAMMA RADIATION

This chapter discusses interaction of ionizing radiation with matter and is followed by an overview of common detector types. Primary focus is on scintillation detection systems. [15], [16], [17]

## 1.1 Interaction of radiation and matter

In order to detect ionizing radiation, it has to somehow interact with matter. The measurement is based on detecting consequences of those interactions. The particles interact on atomic level. The quantum of radiation looses energy during its passage through matter in atomic and subatomic interactions and leaves free electrons and cations behind. Fate of the particle depends on its character, in case of electromagnetic radiation the photon ceases to exist after passing its energy. The situation is more complicated for particles of corpuscular radiation.

If the energy of the primary particle is high enough, it generates secondary radiation, which produces more particles and causes cascade interaction. There are many types of secondary radiation, for example Compton scattering, Cherenkov, Bremsstrahlung (breaking), annihilation or secondary gamma emission, it enriches field of primary radiation.

Excitation and ionization represent the most important interaction of a charged particle with matter. The particle passes its kinetic energy mostly by electromagnetic interaction with electrons in atoms of matter. If the energy is not high enough the electron is only transferred to higher energy level (excitation) from where it returns (de-excitation) and emits a photon. If the passed energy is high enough the electron becomes free and the atom is therefore ionized. The freed electron may have enough energy to cause secondary ionization. Ionizing effects of the particle along its track can be described by the Bragg curve. As the particle slows down its ionizing effects increase because it affects surrounding electrons for a longer period. Just before the particle is fully stopped, there is a peak in Bragg curve.

Beside those principles, there are other phenomena which usually produce secondary radiation. One of them is scattering – it can be either inelastic or elastic. The first one alters wavelength of the radiation while the latter does not. Another important phenomenon is Bremsstrahlung – breaking radiation. It is emitted during scattering of charged particles with great angle during which the vector of velocity of the particle changes rapidly. According to Maxwell equations, it leads to emission of electromagnetic radiation in form of X-ray and gamma photons. This radiation has a continuous spectrum. The phenomenon occurs mostly close to the nucleus

(the shorter distance is the greater energy Bremsstrahlung photon has). X-ray radiation is created also in form of the so-called characteristic radiation with discrete spectrum dependent on material. When the particle unbinds electron on low energy level, its place is filled by electron on higher energy level along with emission of photon of characteristic radiation.

Positronic radiation beta-plus interacts the same way as an electron and unbinds electrons from surrounding atoms. However, after it stops, it annihilates with electron. They both cease to exist and are converted into two quanta of gamma radiation with energy 511 keV [15]. The quanta starts to move in an opposite direction.

### 1.1.1 Interaction of gamma radiation

This thesis is focused on detection of gamma radiation, and therefore the mechanisms of interaction of gamma photons and matter should be described well. These effects also apply to X-ray radiation because it has the same physical principle as gamma radiation.

Quanta of gamma radiation – photons – do not have electrical charge and therefore cannot affect charged particles by electrical forces. Oscillation of electric and magnetic field by which the photon is accompanied can however pass energy to particle and cause excitation or ionization. The nucleus can also be excited by interaction with photons. For lower energies the radiation has rather wave character and affects the whole atom while for higher energies the radiation has rather corpuscular character and interacts mainly with individual electrons.

Some interactions taking place between gamma radiation and matter do not have ionizing character – namely Thompson-Rayleigh scattering, Thomson scattering and electron excitation. It is possible that there is no interaction at all when light material and hard radiation are considered. These phenomena have very little importance regarding the radiation physics.

There are four basic types of interactions. Three of them are showed in figure 1.1. The first one is a photoelectric effect during which the photon passes all its energy to electron in an electron cloud of atom. This electron is emitted with kinetic energy given by difference between passed energy and bond energy. The unbound electron will act like particle of beta-minus radiation and may ionize other atoms. Another electron de-excites to created free place and emits characteristic radiation which can further interact with electron cloud and free the so-called Auger electron. Probability of photoelectric effect is proportional to fifth power of proton number and inversely proportional to energy of the photon. Therefore, the effect does not occur much for energies greater than 1 MeV.

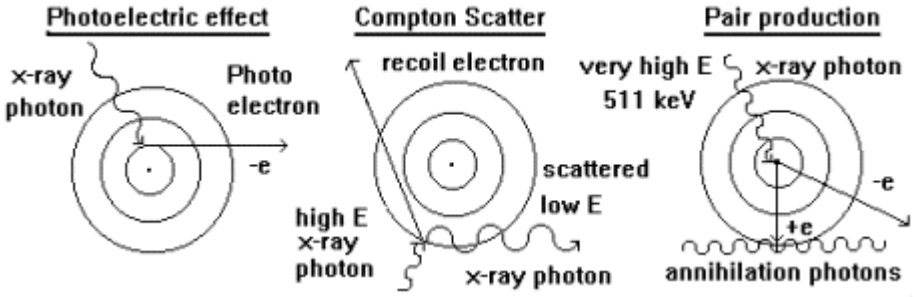


Fig. 1.1: Interactions of gamma radiation [18]

When the photon collides with free or lightly bounded electron, the Compton scattering takes place. It is inelastic scattering during which the photon looses only part of its energy and alters its direction by angle $\theta$. The electron is accelerated by this collision and is able to further ionize. Probability of the interaction is proportional to a density and proton number and inversely proportional to energy of photon.

If the energy of photon is greater than 1.022 MeV, it can be converted to electron and positron in result of electromagnetic interaction with strong field of nucleus. The threshold for this interaction is given by a sum of invariant energy of created particles, that is 511 keV [15] for both of them. Under some circumstances, the pair generation may take place in electron cloud as well. Positron eventually annihilates and secondary gamma radiation is emitted. For high energies of photon this is the dominant interaction.

When the energy is even higher (at least 2.23 MeV – threshold energy for deuterium [17]), it is possible that nuclear photoelectric effect occurs. During the process, nuclear reaction is initiated and either proton or neutron is unbound from the nucleus. The resulting nucleus may be radioactive due to so-called gamma-activation.

## 1.2 Inverse square law

The intensity of radiation may be characterized by its flux – a number of particles passing through a unit area per unit time. It is inversely proportional to the square of distance from a point source. There are no point sources in fact but common sources can be approximated by them if the distance is high in relation with dimensions of the source. This law is extremely important for radiation detection. All quantities used for description of radiation intensity, such as dose rate, are dependent on flux and therefore are inversely proportional to square of distance. The dose

rate produced by a known gamma ray source in distance $d$ from it can be simply calculated from the following equation [19]:

$$\dot{D} = \frac{\Gamma}{3,7 \cdot 10^8} \frac{A}{d^2} \qquad [\mathrm{mGy \cdot h^{-1}; R \cdot cm^2 mCi^{-1} h^{-1}, Bq, m}] \qquad (1.1)$$

$A$ stands for activity, it is a number of radioactive transformations per second and $\Gamma$ is exposure rate constant, its value for different radionuclides can be found in [19]. The inverse square law is very limiting, especially in case of radiation map measurement and source localization.

It is important to mention that this law is generally valid only in vacuum. In other environments the interaction of radiation with matter takes place and the radiation is attenuated. However, attenuation coefficient in air is nearly equal to one.

## 1.3 Detector types

There are three basic types of detectors that are able to measure instantaneous intensity of ionizing radiation and are widely used. First, there are gas-filled detectors, then semiconductor detectors and finally scintillation detectors. A separate section is dedicated to scintillation detectors, first two types are described in this section.

### 1.3.1 Gas-filled detectors

Ionizing chambers, proportional detectors and Geiger-Müller tubes belong to this category. There are also spark and corona detectors [20]. Their common principle is a generation of ion pairs in gas. Ionizing chambers usually work in current mode. They are based on a collection of charge generated by a passage of radiation quantum. Cations and free electrons are charge carriers. They recombine quickly and therefore the collection has to be fast. High intensity electric field is used to do so. The particles are attracted to electrodes, and generate electric current. Its size is proportional to the intensity of incident radiation. Ionizing chambers are typically used in standard handheld dosimeters and are sensitive to energies greater than 100 keV. They are also suitable for calibration of radiation sources due to their good time stability.

Proportional detectors (counters) work almost exclusively in pulse mode. They take advantage of an avalanche effect and therefore are able to detect even a low intensity of radiation compared to ionizing chambers. If the electric field is intense enough, the freed electrons may gain enough energy to cause secondary ionization. The secondary electrons create tertiary ones and the avalanche goes on until all free

electrons are collected by anode. A resistor is in series with detector and the voltage drop on it causes the avalanche to stop. A voltage pulse is measurable. These detectors work in proportional region of a current–voltage characteristic when amplitude of the pulse is proportional to energy of the radiation. Therefore, they can be used for spectroscopy. Typically, the detector is formed of cylindrical cathode with a thin anode wire in its axis. The advantage of this form is a narrow localization of the avalanche – it leads to shorter dead time in comparison to GM tubes. Proportional counters are suitable for detection of gamma radiation with energy lower than 100 keV. With increasing energy the probability of interaction rapidly drops.

Geiger-Müller tubes use the avalanche effect as well and also have a similar geometric form. High internal gain is their advantage because often it is not necessary to use external amplifier which would only cause additional noise. In GM tube, one primary particle usually invokes more than one avalanche due to a chain reaction. The chain reaction is stopped after enough cations are present to reduce the electric field. Number of needed cations is rather constant and therefore the amplitude of measured pulse is always the same. It means that Geiger-Müller tubes do not have spectrometric abilities. It takes quite a long time until cations are collected, and during this period avalanches are not created, and therefore another ionizing particle cannot be detected. The phenomenon is called dead time. Geiger-Müller tubes operate in region of current–voltage characteristic where plateau occurs. GM tubes are used in dosimetry application for example in planar form as a detector of surface contamination.

### 1.3.2 Semiconductor detectors

Utilization of solid state for detection of ionizing radiation has many advantages. They are superior to gas filled detectors in case of high energy radiation due to their higher density. Scintillation detectors also have this advantage but compared to semiconductor detectors they have worse energy resolution due to lower quantum efficiency.

Electron–hole pairs serve as charge carriers in semiconductor detectors. They are generated by a passage of primary charged particle or by a secondary charged particle generated by interaction with photon. The movement of charge carriers in applied electric field creates output signal. Besides better energy resolution, semiconductor detectors are also more compact and have fast response.

For a description of these detectors, ionizing energy is an important parameter. It determines an average amount of energy which is necessary to deliver to electron to jump from valence to conduction band. Typically, it has value 3 eV (ten times less in comparison to gas filled detectors). With this knowledge one is able to calculate

the energy of incident radiation from measured charge. Therefore, semiconductor detectors are suitable for spectroscopy. Ionizing energy depends on temperature. It is almost independent on the type of radiation.

The depleted region of PN junction serves as sensitive volume for detection. The junction operates in reverse mode to enlarge the depleted region and collect generated charge carriers before recombination. Thermal generation of electron-hole pairs is a considerable issue. Silicon detectors may operate in room temperature but germanium detectors have to be always cooled due to their lower band gap.

It is possible to use detectors in current mode and it is convenient especially in high rate situations. They have good linearity up to several amperes. There is another operation mode – the so-called photovoltaic. The detector in this mode works without voltage supply, it uses internal electric field only. But the efficiency is very low.

For the detection of gamma radiation PIN diode is more suitable. Major part of its volume is made of intrinsic semiconductor I in which electron-hole pair generation takes place. Beside standard semiconductor detector, there are also avalanche detectors. They are analogic to proportional counters.

## 1.4 Scintillation detectors

Scintillators are based on converting energy of incident radiation particles into photons in visible spectrum. These photons are then measured using photodetectors which will be described later in this chapter. There are two categories of scintillation detectors – inorganic and organic – their mechanism of conversion slightly differs. In general, a particle in the detector is excited to higher energy level and during its relaxation a photon of visible light is emitted. This principle of detection is widely used and even suitable for spectroscopy. Although the efficiency of scintillation typically ranges from 10 % to 15 %, it is possible to develop highly efficient detector thanks to the photodetectors.

### 1.4.1 Scintillation mechanism

In organic scintillators, the whole molecules are excited and therefore they can be found in solid, liquid and also gaseous states. Basic energy level of electrons is $S_0$ ground level ($S$ for singlet). Absorption of energy causes their transition to $S_1$ band, i.e. $S_1$ ground state and its vibrational levels. Through radiationless transitions all electrons eventually end in $S_1$ ground state. Then they fall back to the $S_0$ ground and vibrational levels, causing emission of photons. The whole process takes only a few nanoseconds and it is called fluorescence. A typical energy diagram is shown

in Fig. 1.2. Due to the energy loss of electrons transitioning from vibrational levels, Stoke's shift takes place causing a shift of peak of absorption and emission spectrum. Consequently, the re-absorption of scintillation photons in material is lower.

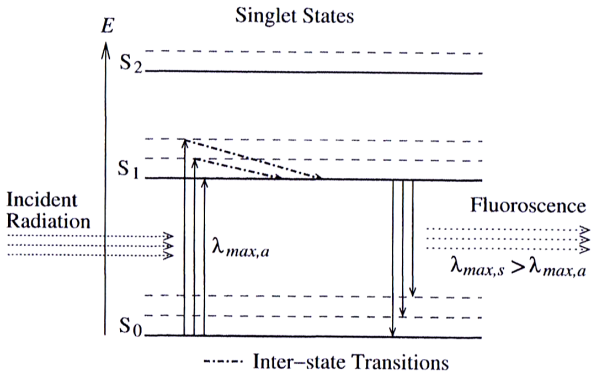


Fig. 1.2: Fluorescence in organic scintillators [16]

Electrons in $S_1$ band can also relax to metastable $T_1$ band ($T$ for triplet). Eventually all electrons fall back to the $S_0$ band with emission of light. But this process known as phosphorescence typically lasts more than 100 milliseconds and therefore creates a parasitic signal. Energy diagram can be found in Fig. 1.3.

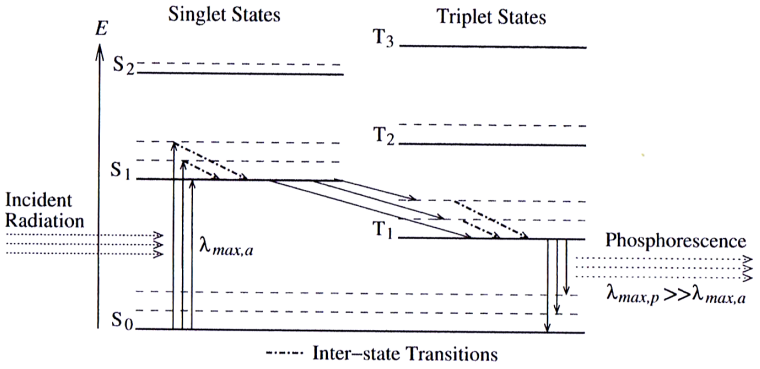


Fig. 1.3: Phosphorescence in organic scintillators [16]

Inorganic scintillators are found in crystalline structure and only individual electrons are excited. Generally, they have higher density and atomic number, therefore they are more suitable for detection of gamma radiation.

These scintillators are basically insulators with wide gap between valence and conduction band. Inside the gap, luminescence and recombination centers can be found. Their presence is caused by dopants (activators) which are required for emission of photons in visible spectrum. If the absorbed energy is greater than band

gap, the electron moves to the conduction band leaving a hole in valance band. After some short amount of time, the electron jumps to the energy level of luminescence center (essentially excited level of activator). Following de-excitation to the recombination center (ground level of activator) can produce emission of photon. Alternatively, energy is dissipated by non-radiation transfer into heat. That is undesirable because it leads to an information loss – quenching. The described process of instant light emission is called fluorescence (analogy with organic detectors).

Another possibility for the electron in the conduction band is to jump to a metastable energy state called electron trap. Presence of traps is caused by impurities and defects of the crystal. For a trapped electron it is impossible to recombine with the hole but is able to return to the conduction after receiving typically thermal energy. Then electron may cause delayed light emission – phosphorescence. Energy diagram of scintillation in inorganic material is shown in Fig. 1.4.

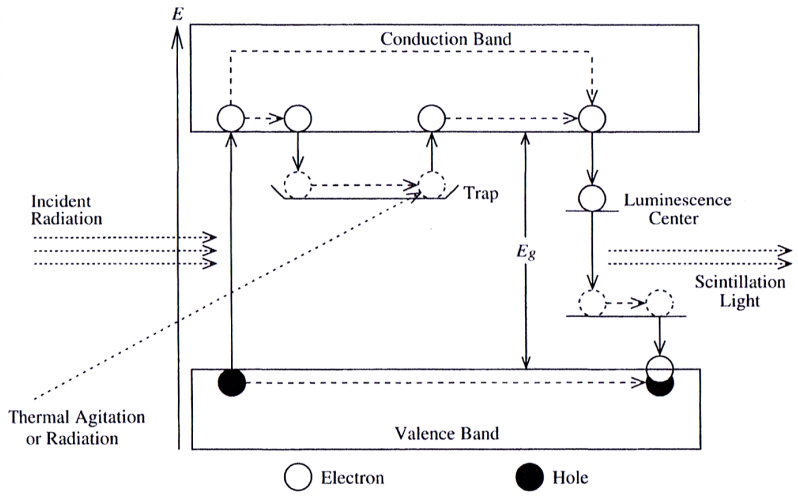


Fig. 1.4: Diagram of inorganic scintillators [16]

### 1.4.2 Basic parameters

The most important parameter of the scintillator is light yield. Low light yield causes insufficient signal-to-noise ratio and is critical especially in spectroscopic applications. It is usually measured in number of emitted photons per MeV of absorbed radiation. Tens of thousands of photons per MeV is not an uncommon value. Light yield depends mostly on the scintillation material, type of incident particles, energy of particles and temperature. The energy dependence worsens energy resolution of the system and is caused by secondary excitation of electrons.

Other important parameters are rise and decay times. Both scintillation rise and decay have exponential character but their time constants may differ rapidly. While typical rise time is less than one nanosecond, decay time ranges from a few nanoseconds to several milliseconds. Long decay time is causing lower efficiency of the system, especially in high rate situations. Decay time constant varies for different types of incident particle. For example, alpha-particles due to their high stopping power cause that more electrons end in the metastable energy states and therefore cause significant delayed emission. Usually, the average decay constant can be found in technical literature.

### 1.4.3 Plastic scintillators

Plastic detectors are fabricated by homogenously mixing base monomer material and scintillator with concentration about 1 %. The mixture is then polymerized. In result it is chemically stable and optically homogenous. It also can be easily fabricated in any shape. Because the photons emitted by scintillator usually have short attenuation lengths (typically few millimeters), a combination of more scintillation materials is used. The main scintillator called primary fluor emits ultraviolet photons with larger attenuation length. The secondary fluor works as a wavelength shifter and converts ultraviolet photons typically to blue light.

Although these detectors have rather varied properties, generally they are not suitable for spectroscopy. Usually they have high light yield but it is dependent on type and energy of radiation and climatic conditions. The major problem is the nonlinearity of light output. The material is also unsuitable for measurement of high radiation fields because of extensive delayed glow effect. The scintillation and optical properties can be altered by changing concentrations of primary and secondary fluors.

### 1.4.4 Inorganic scintillators

The most typical material in this category is thallium doped sodium iodide – NaI(Tl). It is also the most widely used scintillator thanks to its features. It has light yield higher than 40,000 photons per MeV and low self-absorption of scintillation photons. Photons of blue light with wavelengths coinciding with common photomultiplier tubes are emitted. Large area crystals can be produced and the production cost is low. It is also suitable for spectroscopy. The biggest disadvantage of NaI(Tl) is hygroscopicity which makes material vulnerable to moisture. Therefore, the crystal has to be sealed well.

Other typical inorganic scintillators are sodium doped cesium iodide (CsI(Na)), thallium doped cesium iodide (CsI(Tl)) and bismuth germanate (BGO). The first one has similar light yield and emission like NaI(Tl) but is less hygroscopic. CsI(Tl) has light yield over 65,000 photons per MeV, is mechanically stable and non-hygroscopic. Its emission coincides with common photodiodes. Bismuth germanate has large energy resolution, short decay time and is mechanically stable. It also has high absorption efficiency for photons of gamma radiation and is therefore commonly used for gamma spectroscopy.

### 1.4.5 Light guides

It is not always feasible to attach the scintillator directly to a photodetector with large enough area. Therefore, light guides are employed. Their purpose is to transmit scintillation photons to the photodetector with minimal loss. Light guides are based on either simple reflection or total internal reflection. The latter is more convenient because it offers lower photon loss. Typical guide materials have refractive index about 1.5 and are surrounded usually by air. That gives critical angle larger than 42°. Fulfilling of this condition for total reflection is guaranteed by proper geometry, usually the so-called fish-tail shape is used. If the path from detector to photodetector is large, optical fibers are utilized.

## 1.5 Photodetectors

There are two basic types of photodetectors – photodiodes (PDs) and photomultiplier tubes (PMTs). The latter are widely used because of good signal-to-noise ratio and fast response. On the other hand, they are more mechanically sensitive.

### 1.5.1 Photomultiplier tubes

The amount of photons emitted by the scintillator is not very large, and without some form of amplification signal-to-noise ratio would be very poor. Photomultiplier tube serves as an amplifier, it converts photons into a large number of electrons. Typical PMT consists of photocathode, electron multiplication structure composed from dynodes and readout anode. Good sensitivity, time response and signal-to-noise ratio are advantages of these devices. Schematic picture can be found in Fig. 1.5

Photocathodes are able to emit electrons thanks to photoelectric effect. The maximal wavelength of photons to be converted is given by work function of photocathode material. The quantum efficiency of conversion usually ranges from 10 %

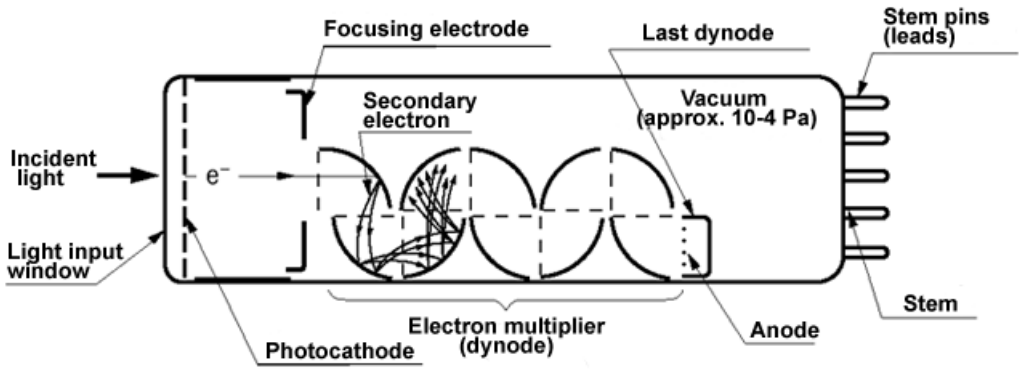


Fig. 1.5: Scheme of a photomultiplier tube [21]

to 30 %. It depends strongly on the wavelength of photons. The dependency has a plateau and beyond it the efficiency drops rapidly. Therefore, scintillation spectrum of the detector has to overlap with this plateau, its peak should be located somewhere in the middle of the plateau. There are two ways to make photocathode – it can be either transmissive or reflective. The first one allows transmission of photoelectrons through it and is usually constructed as a thin layer on the entrance window. Some materials have good quantum efficiency but are opaque to photoelectrons. However, it is possible to use them in reflection mode. Such photocathode is constructed as a thin layer on a metal electrode inside the tube. Bialkali materials (e.g. SbRbCs) are the most common because they are sensitive to blue light emitted by NaI(Tl) scintillators. Their quantum efficiency reaches 30 % and they are also thermally stable. Other materials for photocathodes are for example AgOCs, GaAs(Cs) and $SbCs_3$.

The electrons are then collected by the first dynode. Due to low efficiencies, it is essential to collect as many photoelectrons as possible. When fast timing is required all electrons should have the same transit time. To fulfill those requirements, electron focusing structure is often utilized in photomultiplier tubes.

The electron yield is then increased by multiplication structure. Cascade of metal electrodes, called dynodes, is used. They have an ability to emit electrons after interaction with an electron that have enough energy. The amount of emitted electrons is larger than the amount of incident electrons. The conversion process has a high linearity. To provide electrons with energy, they are accelerated by electric field. Each dynode has higher potential than the previous one. The potential difference between photocathode and anode is typically hundreds of volts. Geometry of dynodes is crucial because it is needed to focus electron flux to the next dynode. Some photomultiplier tubes are very sensitive to mechanical jitters which causes a

non-linearity. There are many different dynode geometries, some of them are even less prone to mechanical instability, for example: linear, box and grid, circular cage, venetian blind, mesh, micro-channel plate and others. High potential gradient is provided by voltage divider. The photocathode is usually connected to the ground. Stabilization capacitors are usually connected to the last few dynodes because large signal current could alter inter-dynode voltage.

The anode has a form of metallic grid located very close to the last dynode. Collection of electrons before they reach the last dynode by anode is not considerable due to the spaces in its grid. Secondary electrons from the last dynode are not accelerated to next one, and therefore create a space charge which is quickly collected by anode. Output current can be measured at the anode but it is preferable to convert it into voltage at a load resistor. The voltage is then amplified to achieve good signal-to-noise ratio.

To prevent loss of electrons, the multiplication structure has to be kept in vacuum. The enclosure is usually made of glass. The material of entrance window is important because it has to be well transparent for wavelength produced by the scintillator. Fused silica is commonly used, other possible materials are lime glass, lithium fluoride and sapphire.

There are numerous parameters to describe efficiency of photomultiplier tube. Overall detection efficiency is composed of quantum efficiency of the photocathode and collection efficiency of dynodes. It is defined as ratio of average number of measured pulses to average number of incident photons. Some types of sensitivities are also often quoted by manufacturers. First there is radiant sensitivity – ratio of photoelectric current to incident radiant power [A/W]. Cathode luminous sensitivity is ratio of photoelectric current to flux from a tungsten filament operated at 2856 K, similarly anode luminous sensitivity is defined as ratio of anode current to the flux [A/lm].

Photomultiplier tube is also characterized by gain $\mu$ which carries information of how effectively the photoelectrons are converted into output signal. It is defined as ratio of the anode current to the photoelectric current. Every dynode is characterized by secondary emission ratio defined by equation [16]:

$$\delta = AV_{dy}^{\alpha} \tag{1.2}$$

$V_{dy}$ is the dynode voltage, $\alpha$ is geometrical and material constant, its typical value ranges from 0.7 to 0.8. Finally $A$ is a proportional constant. Assuming the tube has $n$ dynodes with the same secondary emission ratio and even voltage distribution

with supply voltage $V$, overall gain can be computed as [16]:

$$\mu = \frac{A^n}{(n+1)^{\alpha n}} V^{\alpha n} \tag{1.3}$$

Typical gain of PMTs is in order of $10^5$ or $10^6$. When dynodes have different parameter, the overall gain has value [16]:

$$\mu = \prod_{i=1}^{n} \delta_i \tag{1.4}$$

Another desired feature is the uniformity of photocathode. Usually it is needed to cover large area and the response should not depend on position of incident photon. Generally the sensitivity of photocathode drops with increasing distance from center. For timing applications time and frequency response is important. Frequency response is characterized by cutoff frequency which is dependent primarily on the external circuitry. Time constant is defined by effective load resistance and total capacitance of the output. Time response is given by the electron multiplication structure because the secondary electron emission is a statistical process. Even if the photon pulse is rectangular, the resulting anode pulse has exponential spread. Linear focused tubes have superior time response over other types.

In general, energy resolution of photomultiplier tubes is poor. Again it is implied by Poisson distribution of secondary electron emission. The spread in the number of electrons is therefore inversely proportional to the square root of average number of emitted electrons. The only way to improve energy resolution is to provide dynodes with very high gain $\delta$. Scintillators themselves have good energy resolution, therefore semiconductor photodetectors are often utilized to improve resolution of the whole detection system.

There are two different operating modes for photomultiplier tube. In the first one – digital mode – individual pulses are counted. That requires incident photons to be well separated in time. When the pulses overlap, it is necessary to work in the analog mode in which average anode current is measured. The measurement is always burdened by noise. Among noise sources it is possible to find thermally agitated electron emission, glass scintillation, leakage current or mechanical instability. Photocathodes usually have low work function and therefore they are able to emit electrons after absorbing thermal energy. This noise can be minimized by cooling or by decreasing photocathode area. Thermal emission along with leakage current caused by imperfection in insulations are the main sources of the so-called dark current. It is current measurable even if no photons are entering the photomultiplier tube. The resulting signal noise is also affected by readout electronics. The noise is a problem mainly when measurement of pulses' amplitude is needed –

in analog mode and in spectroscopic applications. If the device works purely in a counting mode, the noise is suppressed by discriminators. PMTs are also sensitive to a magnetic field which can alter the trajectory of electrons in the multiplication structure.

### 1.5.2 Photodiode detectors

In some circumstances, using a semiconductor photodetector can be more convenient. These photodetectors have very high quantum efficiency compared to PMTs and are also more compact, mechanically stable and insensitive to magnetic field. Usually, they have worse time response. However, modern technologies improve parameters of photodiodes. Several types of diodes such as PIN diode, heterojunction diode or Schottky diode can be used as photodiodes. They just need to be optimized to work in visible spectrum.

PIN diode is made of thin entrance P layer, followed by depleted I region and closed by N layer. Incident photon in depleted region produces an electron–hole pair which is collected by preamplifier thanks to the applied voltage. The generated and measured charge is of the same order as number of incident photons, so it is much lower than in photomultiplier tubes. Photodiodes have therefore worse signal-to-noise ratio. There are two types of noise – serial and parallel. The first one appears at the input of preamplifier and its magnitude is proportional to capacity of the diode. The smaller dimensions of diode are the higher its capacity is. Diodes with area lower than 1 $cm^2$ are unsuitable. The parallel noise corresponds with the leakage current and increases with the increasing dimensions of the diode. The noise is affected also by a time constant of the readout circuitry. As the time constant increases, the serial noise is decreasing but the parallel noise is increasing and vice versa. Because of these conflicting requirements, it is always necessary to search for a compromise. Dark current is also significant parasitic effect, it has identical meaning as dark current in PMTs. Especially silicon diodes have higher noise level than a similar photomultiplier tube, its utilization in higher temperature is almost impossible. More suitable material for photodiodes is for example mercury iodide. The noise also makes photodiodes unsuitable for large area scintillators, matrix semiconductor photodiodes have not proved good. Another problem is that the particle of ionizing radiation could interact directly with photodetector's sensitive volume and cause significant parasitic signal. Therefore, the diode has to be as thin as possible – again it is conflicting requirement.

### 1.5.3 Avalanche photodetectors

An even better solution is to use avalanche photodiodes (APDs). They use similar multiplication effect as proportional gas detectors. Incident photon generates electron–hole pair and the electron is accelerated by applied high voltage. If the energy of electron is at least three times greater than the band gap of the material, it is able to produce secondary charge pairs. The secondary electrons are again accelerated and may produce tertiary charge pairs and so on. In result, the number of produced charge pairs is much higher than in conventional photodiodes. The current is proportional to energy of incident photons and the signal-to-noise ratio is also good, therefore avalanche detectors are suitable for spectroscopic applications.

There are some desirable features that APDs should have. Small leakage current is required. It causes dark current which can cause unwanted avalanches that may induce non-linearity to response. High and stable gain is also wanted to achieve good signal-to-noise ratio and linearity. Typical APDs have gain of the order of $10^4$ but can reach up to $10^8$. Finally, good frequency response comparable to the response of photomultiplier tubes is desirable especially in high rate situations.

The gain is proportional to the applied high voltage and is very sensitive to any change of this voltage, therefore well stabilized voltage source is required. The applied voltage is higher than in case of PIN diodes, however must not be too high because it could cause breakdown of the diode. In a typical form the entrance window is made of thin P layer to which negative voltage is applied. Bulk made of lightly doped semiconductor of P type follows, the charge multiplication takes place here. The structure is closed by P layer and N layer to which positive voltage is applied.

The avalanche diode can work either in linear or Geiger mode. In the latter, the amplitude of charge pulse is not proportional to incident photon energy and therefore is used only as counting device, similarly as the photomultiplier tube in digital mode.

## 1.6 Direction-sensitive detection

When a lost radiation source is searched, it can be assumed that information about direction would be helpful. To get that type of information, a direction-sensitive detection system is needed. One possible way to achieve this goal is to assemble the system from multiple independent detectors. The idea is inspired by [22]. An option with two detectors is discussed further below.

The basic idea is that the source located outside of axis of symmetry of two-detector system has larger distance from one detector than from the other. For

some angles, also collimation takes place. The radiation is attenuated in closer detector before reaching the further. It is possible to even intensify the effect by placing shielding between the detectors.

The angular dependence of distance can be expressed analytically. Geometry of the system can be seen in Fig. 1.6. Ratio $R$ of total count measured by both detectors should carry information about source direction. Measured total count is inversely proportional to square of distance. Assuming detectors have same sensitivity $K$, the ratio can be expressed as:

$$R = \frac{\frac{K}{d_1^2}}{\frac{K}{d_2^2}} = \frac{d_2^2}{d_1^2} \tag{1.5}$$

Square of distance can be expressed from the law of cosines as a function of anglular distance of the source from detectors' axis of symmetry $\phi$.

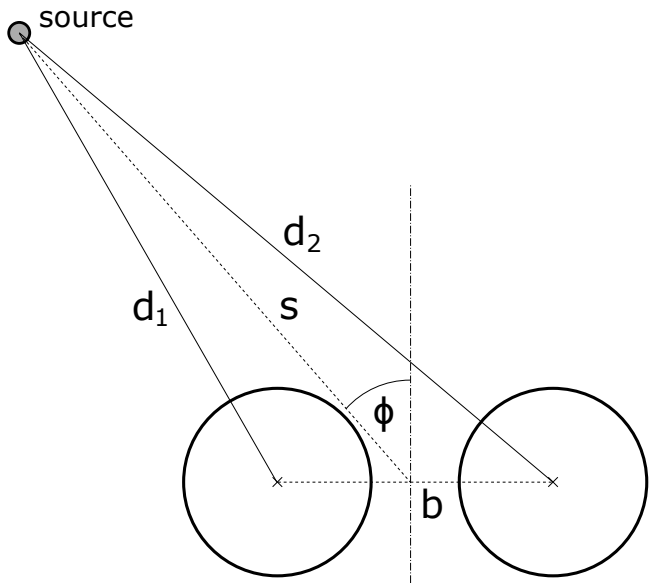


Fig. 1.6: Geometry of the two-detector system

$$d_1^2 = s^2 + \left(\frac{b}{2}\right)^2 - 2s\left(\frac{b}{2}\right)\cos\left(90 - \phi\right) = s^2 + \left(\frac{b}{2}\right)^2 - 2s\left(\frac{b}{2}\right)\sin\phi \tag{1.6}$$

$$d_2^2 = s^2 + \left(\frac{b}{2}\right)^2 - 2s\left(\frac{b}{2}\right)\cos\left(90 + \phi\right) = s^2 + \left(\frac{b}{2}\right)^2 + 2s\left(\frac{b}{2}\right)\sin\phi \tag{1.7}$$

Expressions containing $s$ or $b$ can be replaced by contants $c_0$ and $c_1$. The ratio dependence of angular distance has therefore shape of function:

$$R = \frac{d_2^2}{d_1^2} = \frac{c_0 + c_1 \sin\phi}{c_0 - c_1 \sin\phi} \tag{1.8}$$

A comparison of the shape of a function for different values of parameter $s$ is in Fig. 1.7. It is obvious that with increasing distance of source the shape is more similar to sine wave and its amplitude is decreasing. The low amplitude present a problem because of bad signal-to-noise ratio of measurement of distant sources. Utilization of shielding between detectors could be helpful.

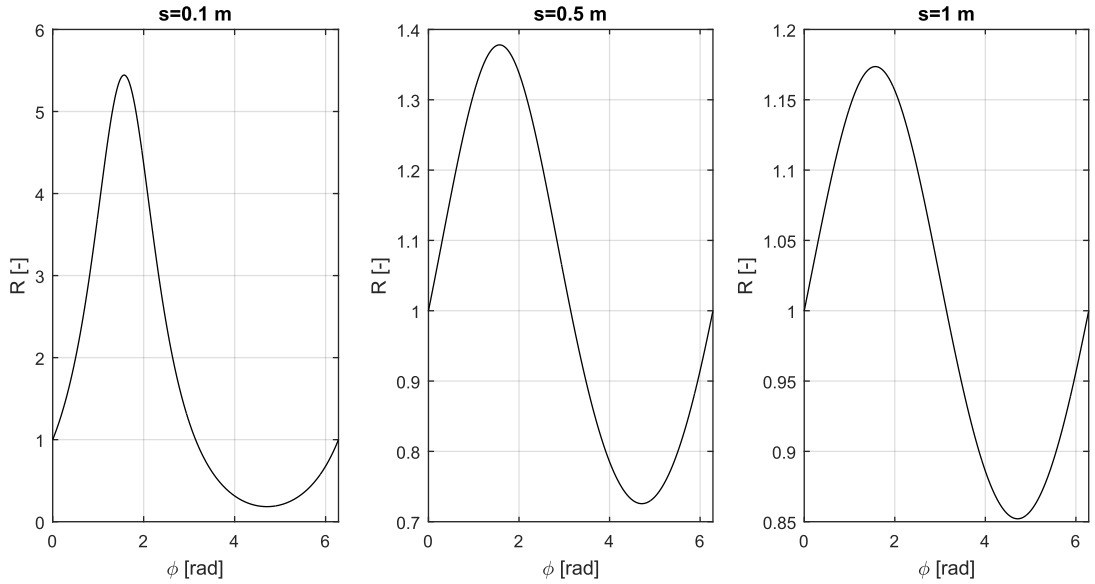


Fig. 1.7: Parametrized shape of the ratio dependence of angle

# 2 TECHNICAL EQUIPMENT

This thesis introduces a system consisting of a mobile robot equipped with precise global navigation satellite system (GNSS) receiver and a radiation detection device. It can be controlled remotely through custom wireless interface.

## 2.1 Robotic platform

Civil reconnaissance robot Orheus-X3 is used for experimenting. It was developed by Group of Robotics and AI at the Faculty of Electrical Engineering and Communication, Brno University of Technology. It is a four-wheeled mid-size robot equipped with sensory head carrying cameras. The head is unnecessary for radiation mapping, therefore it is not used. The robot has the ability to carry both the GNSS receiver with two antennas and gamma detectors with counting electronics. Basic parameters of the robot are shown in Tab. 2.1. A schematic picture of robot carrying key equipment is in Fig. 2.1. PC can be found inside robot's body. All sensors are connected to this PC via Ethernet. The robot also provides power supply for sensors.

Tab. 2.1: Parameters of the robot Orpheus-X3 [23]

| **Parameter** | **Value** |
|---|---|
| Dimensions | $950 \times 590 \times 415$ mm |
| Weight | 51 kg |
| Operation time | 120 min |
| Drive type | Differential |
| Maximal speed | 15 km·h$^{-1}$ |

## 2.2 GNSS receiver

For a precise measurement of position of the robot Orpheus-X3, two real time kinematic (RTK) GNSS receivers Trimble BX982 [24] are used. One of them serves as stationary base station, the other one is located on the robot in rover configuration. The stationary module uses one antenna input and sends correction data to the rover module. The latter one has dual input for primary and vector antenna. That enables measurement of azimuth. An overview of basic receiver parameters is in Tab. 2.2. Whole GNSS configuration is shown in Fig. 2.2.

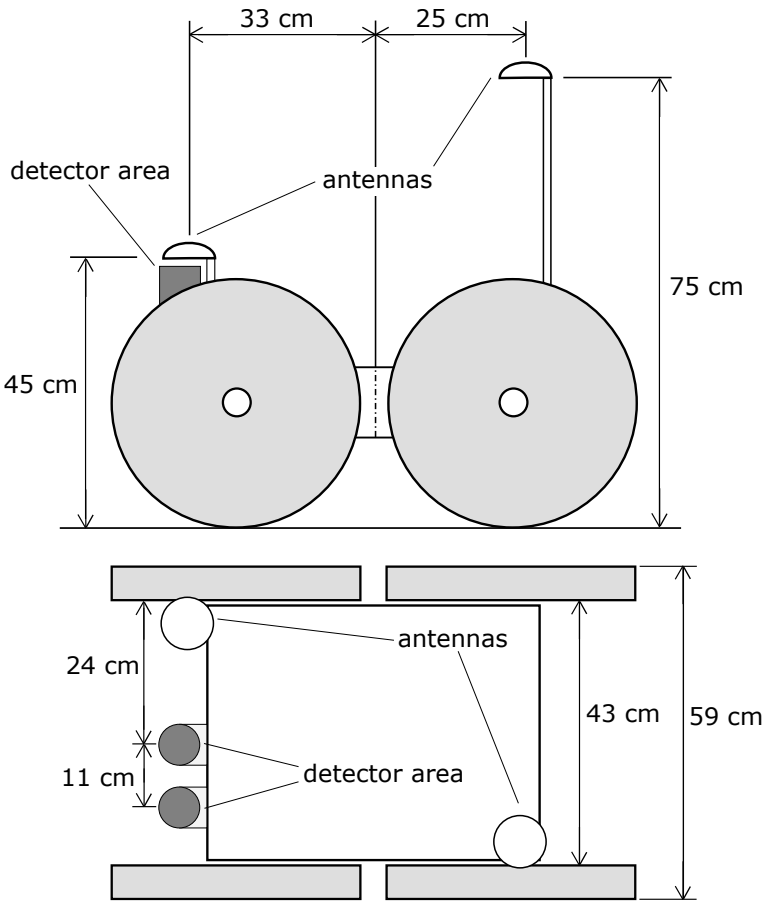


Fig. 2.1: Schematic picture of Orpheus-X3

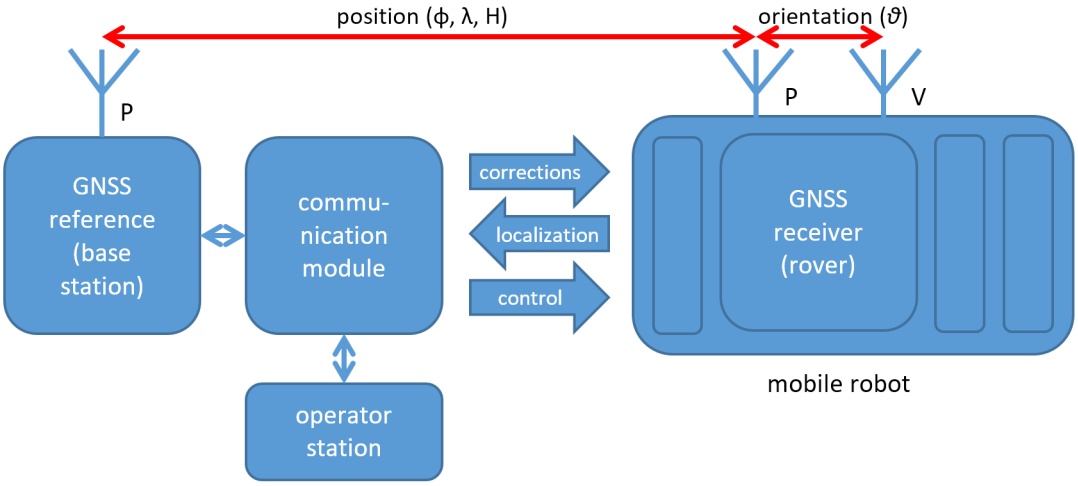


Fig. 2.2: GNSS configuration [23]

Tab. 2.2: Parameters of a GNSS receiver Trimble BX982 [23]

| **Parameter** | **Value** |
|---|---|
| Number of channels | 220 |
| GNSS supported | GPS, GLONASS |
| RTK | supported |
| Dual input for azimuth calculation | supported |
| Power | 9–28 V DC, max 5 W |
| Weight | 1.6 kg |
| Dimensions | 264 × 140 × 55 mm |
| Operating temperature | –40 °C to +70 °C |

Tab. 2.3: Description of a GGA message [25]

| **Field** | **Example** | **Meaning** |
|---|---|---|
| 0 | GPGGA | Message identifier |
| 1 | 172814.0 | UTC of position fix in *hhmmss.ss* format |
| 2 | 3723.46587704 | Latitude in *ddmm.mmmm* format |
| 3 | N | Direction of latitude – N (North) or S (South) |
| 4 | 12202.26957864 | Longitude in *ddmmm.mmmm* format |
| 5 | W | Direction of longitude – E (East) or W (West) |
| 9 | 18.893 | Orthometric height (MSL reference) |
| 10 | M | M – unit of measure for orthometric height is meters |
| 11 | -25.669 | Geoid separation |
| 12 | M | M – unit of measure for geoid separation is meters |

Communication works in a mode where the PC serves as aserver and the receiver connects to it. IP address of the computer and port have to be configured prior to the measurement. UDP packets are used for transmission. Measurement frequency and data format can also be set. In PC it is only required to listen on the selected port and then receive data periodically.

Data are being sent in NMEA-0183 message format. These messages are prefaced with `$` character and terminated by characters `\r` and `\n`. Values are separated by a comma. There is also a checksum at the end of the message, separated by `*` character. The checksum is the 8-bit XOR of all characters in the message, including the commas between fields, but not including the `$` and `*` delimiters. The hexadecimal result is converted to two ASCII characters (0–9, A–F). For a proposed

measurement system, GGA and PTNL-AVR messages are used. Message type is distinguished by an identifier. Example of GGA message [25]:
`$GPGGA,172814.0,3723.46587704,N,12202.26957864,W,2,6,1.2,18.893,M,-25.669,M,2.0,0031*4F`

An overview of important values can be found in Tab. 2.3. Example of PTNL-AVR message [26]:
`$PTNL,AVR,181059.6,+149.4688,Yaw,+0.0134,Tilt,,60.191,3,2.5,6*00`

Important values are shown in Tab. 2.4. Update rate of 10 Hz is sufficient for proposed application.

Tab. 2.4: Description of a PTNL-AVR message [26]

| **Field** | **Example** | **Meaning** |
|---|---|---|
| 0, 1 | PTNL,AVR | Message identifier |
| 2 | 181059.6 | UTC of vector fix in *hhmmss.ss* format |
| 3 | +149.4688 | Yaw angle in degrees |
| 5 | +0.0134 | Tilt angle in degrees |

Coordinates provided by the GNSS receiver correspond to the position of the main antenna in the front of the robot. In order to get coordinates of a radiation detector, transformation has to be performed. The situation is illustrated in Fig. 2.3. Points $A_1, A_2$ represent the center of the main and vector GNSS antennas. Point $D$ represents center of detector. Angle $\alpha$ is an azimuth of a line connecting the antennas, $\phi$ is an angle between this line and an asix of the robot. Given these angles and coordinates of $A_1(x_a, y_a)$, coordinates of $D(x_d, y_d)$ may be computed as:

$$x_d = x_a + |A_1D| \cos\beta = y_a + |A_1D| \cos\left(180° + \phi - \alpha\right) \tag{2.1a}$$

$$y_d = y_a + |A_1D| \sin\beta = y_a + |A_1D| \sin\left(180° + \phi - \alpha\right) \tag{2.1b}$$

## 2.3 Gamma radiation detection system

Detection system is composed of scintillation detectors and measuring electronics. A pair of 2-inch NaI(Tl) detectors is used as scintillators. Detectors are integrated with photomultiplier tubes equipped with standard 14-pin base. Multichannel analyzers NuNA MCB3 [27] manufactured by company NUVIA a.s. are used as electronics. The analyzers provide high voltage source, a preamplifier, ADC sampling and processing. Data transfer is possible via USB or Ethernet. An overview of basic

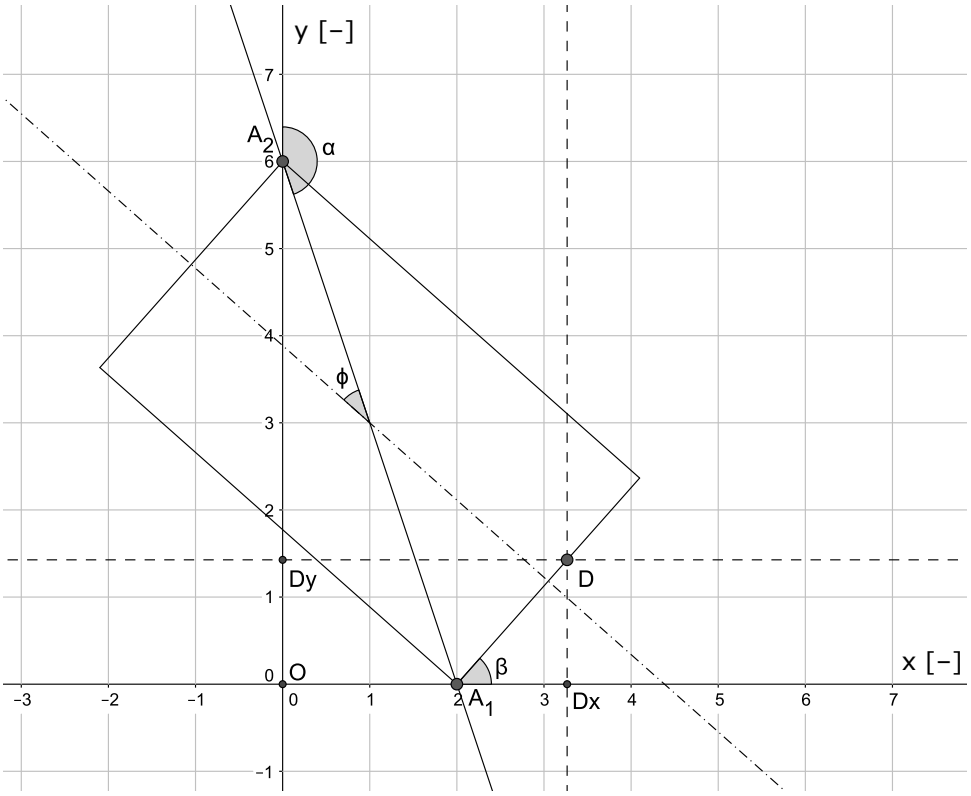


Fig. 2.3: Transformation of coordinates

analyzer parameters is in Tab. 2.5. A detector together with an analyzer is denoted as *detector tube*.

Detector tubes are equipped with lead shielding. One half of each spherical detector is covered with 2 mm thick lead layer in direction to the other one. The reason is to intensify directional sensitivity of resulting detection system.

Both the detector tubes are fixed to the robot by custom mounting. The mounting is composed of aluminum L profile and two sets of components printed on a 3D printer from polylactic acid (PLA). A model of complete mounting is in Fig. 2.4. Detector located closer to a center of the robot is denoted as *main detector*, the other one is *secondary detector*. The complete system consisting of robot, GNSS receiver and detector tubes is shown in Fig. 2.1

Tab. 2.5: Parameters of a multichannel analyzer NuNA MCB3 [28]

| **Parameter** | **Value** |
|---|---|
| Dimensions | $60 \times 60 \times 112$ mm |
| Weight | 340 g |
| Power | 9 to 30 V DC, 4 W |
| Operating environment | −30 to 55 °C, max. 80% humidity |
| Spectral resolution | 256, 512, 1024, 2048 or 4096 channels |
| Fine gain | 0.8 to 2.0 |
| Dead time correction | Error <5 % up to 50 000 CPS |
| High voltage source | 0 to 1100 V DC, step 1 V |

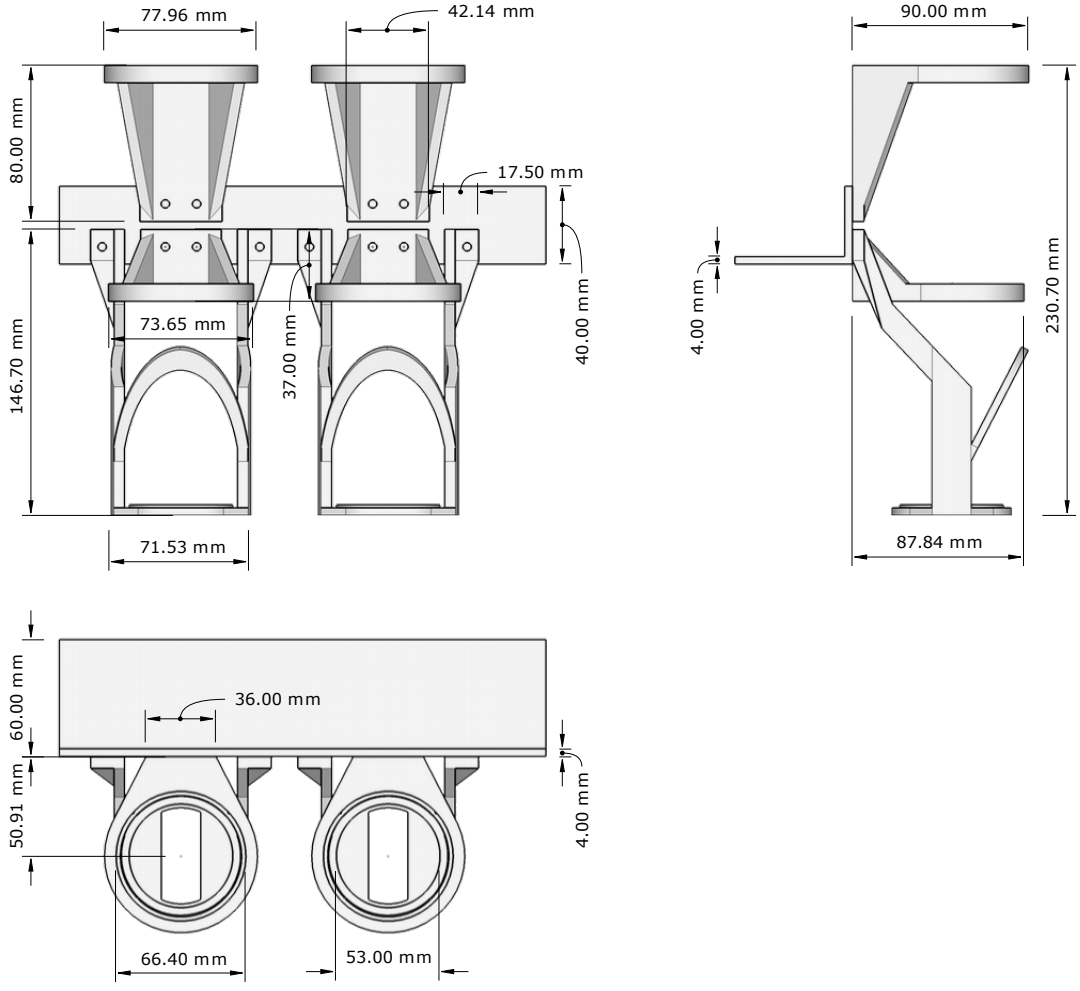


Fig. 2.4: Mounting for detector tubes

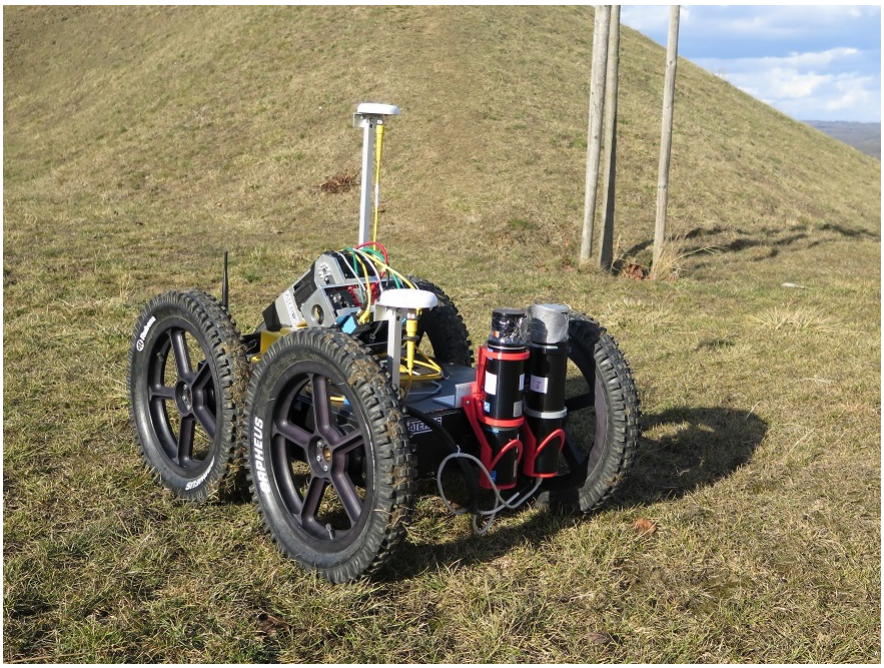


Fig. 2.5: Robot Orpheus-X3 carrying equipment for gamma radiation measurement

Proprietary communication protocol is used for communication with analyzers [28]. No data are sent from the device without asking. Communication packet has the following structure:
`| NextB_H | NextB_M | NextB_L | DevAdr | Cmd | Data | Checksum |`
where `NextB` (3 bytes) determines number of following bytes, `DevAdr` is reserved for communication via RS-485, `Cmd` is command code, and data are block of bytes. Checksum is two's complement of 8-bit sum of all packet bytes. Device response has the same command code as request if there is no error. Code 0xE0 is returned if an error occurs. The following commands are important for measurement.

**cmLink – 0x01**

Serves for initiating a communication. PC does not send any data bytes, string containing brief description of device is returned.

**cmGetSpectrum – 0x03**

Serves for spectrum acquisition from the device. PC sends only commands without data. The device responds with a data block (all values have the most significant byte first):

| | | |
|---|---|---|
| 1. | B | status of spectrum acquisition and compression<br>bit 0–3 – number of bytes per channel<br>bit 7 – spectrum acquisition is/is not in progress |
| 2.–3. | B | first channel defined by lower level discriminator (LLD) |
| 4.–5. | B | last channel defined by upper level discriminator (ULD) |
| 6.–9. | B | current Real time in 0.01 s |
| 10.–13. | B | current Live time in 0.01 s<br>(difference between Real and Live time represents dead time) |
| 14.–15. | B | conversion gain – number of channels |
| 16.–19. | B | timestamp – MCB3 does not have RTC; it sends 0xFFFFFFFF |
| 20.–*n*. | B | pulse values in each channel |

The number of data bytes is determined by a number of channels in range LLD–ULD, and also by a compression level.

**cmStart – 0x05**

Serves for starting the spectrum acquisition. Device responds with one data byte:

| | |
|---|---|
| 1 | spectrum acquisition started |
| 0 | spectrum acquisition is already running |

**cmStop – 0x06**

Serves for stopping the spectrum acquisition. Device responds with one data byte:

| | |
|---|---|
| 1 | spectrum acquisition stopped |
| 0 | spectrum acquisition is not running |

**cmClr – 0x07**

Serves for clearing spectrum buffer. If successful, data byte with value 0x01 is returned.

**cmSetTimers – 0x08**

Serves for setting duration of spectrum acquisition. Resolution is 1 millisecond, values have the LSB first. If successful, data byte with value 0x01 is returned. PC sends the following data block:

| | | |
|---|---|---|
| 1.–4. | B | requested Real time |
| 5.–8. | B | requested Live time |

**cmSwitchHV – 0x0B**

Serves for switching on/off the high voltage source. PC sends one data byte with requested HV state. The device also responds with one data byte with actual HV state.

1 switch on HV source
0 switch off HV source

**cmSetHV – 0x0C**

Serves for setting high voltage value. PC sends two data bytes with requested HV value (the LSB first). If successful, data byte with value 0x01 is returned.

**cmGetHV – 0x0D**

Serves for getting high voltage value. PC sends command only. The device responds with data block (values have the LSB first):

1. B 0 – HV source switched off, 1 – HV switched on
2.–3. B set HV value
4.–5. B actual HV value

## 2.4 Navigation module

Navigation module is a PC program responsible for a control of robot motion. It was developed by Ing. Tomáš Jílek, Ph.D. within his PhD thesis [29]. One of its submodules is a self-localization module. It takes data from GNSS receivers, odometry and others in order to get precise position in selected coordinate system – World Geodetic System 1984 (WGS-84) is used [30]. To define a trajectory of the robot, a sequence of waypoints is used. The rotation center of the robot is navigated to current waypoint. When the waypoint is reached or detected as unreachable, the next waypoint is loaded. Ride along a rhumb line (loxodrome) is used for navigation.

The module can be controlled by commands sent through UDP protocol. The structure of commands comes out from NMEA messages:
`$DVMSG,it1,it2,...,itn*CH[CR+LF]`
where `DV` is device code, `MSG` is message code, `it#` are message items and `CH` is checksum. For basic control the following commands are used (delimiters, device code and checksum are omitted):

```
1 LST,id,lat,latNS,lon,lonWE,lat_err,lon_err
2 LST,END
3 ACT,id
4 CLR
5 SES,state
```

Command 1 allows setting of sequence of waypoints. Each message includes one waypoint defined by latitude and longitude (and their direction) along with ID which determines the order in the sequence. The second command follows the last item of sequence. Command 3 serves for setting which waypoint should be navigated to. Command 4 clears all waypoints. The last command sets the navigation state – either `IDLE` or `GOFORWARD`. The following messages can be sent by a navigation module:

```
1 WPT,id,lat,latNS,lon,lonWE,lat_err,lon_err
2 GET,id
```

The first one informs which waypoint is currently navigated to. The second serves for requesting lost or invalid waypoint.

## 2.5 Control software

In order to manage data collection and control the robot's trajectory (measurement trajectory), a software was developed using C# language and .NET Framework. Several libraries were also developed to assist the main program. Their brief description now follows.

### 2.5.1 Description

*McbConnector* is responsible for communication with MCB modules. It implements a protocol described in Sec. 2.3. Communication is managed by two TCP clients, one of them is used for sending commands to the device and the other is asynchronously receiving any returned data. Those are then parsed and if valid, an event is invoked to inform the superior software components. Both sent and received messages are stored in a communication log.

*McbTimer* settles with periodic acquisition of spectrum data from all connected MCB modules. The time synchronization is provided by data from GNSS receiver, which include precise time information. Desired measurement period is 1 second, therefore spectrum data are requested if current time has integer seconds. Data are logged along with the corresponding position information. Also the library can be

used for measurement when GNSS signal is not available (e. g. for calibration of detectors in laboratory), then the synchronization is provided by an internal timer.

*GnssConnector* is used for reception of position data from GNSS receiver. UDP client is set to listen on selected port and receives data asynchronously. For parsing the NMEA messages library *BX982NMEA* developed by Ing. Tomáš Jílek, Ph.D. is used. All received data are logged and also stored in buffer until it is extracted by a superior module. *GnssConnector* provides synchronization for *McbTimer*.

*NavConnector* is responsible for communication with the navigation module. It implements a protocol described in Sec. 2.4. Communication is managed by a pair of UDP clients. When information about current waypoint is received, it is validated and passed to the superior module through an event.

*MapTransform* serves for transforming coordinates into different coordinate systems. It is important for planning the measurement trajectory, which is done in Cartesian system, while navigation module works in polar coordinates.

*RMath* provides mathematical background for other modules. It deals mostly with analytic geometry.

*MeasConfig* is responsible for configuration of the whole system. Configuration is parsed from an XML file and stored in defined structures where it is accessible to other modules.

*MeasMaster* is the most important and superior module. Among other things, it interconnects all previously introduced components. Before any experiment can take place, all components have to be set to the desired state and tested if they work correctly. During the experiment, this module is responsible for an eventual update of measurement trajectory.

A flowchart of experiment control is shown in Fig. 2.6. First five steps fall into preparation. If any of them fails, the experiment is interrupted. The flowchart is then divided into two branches. The left one represents communication with the navigation module. Some waypoints are marked in a sense that measurement trajectory should be revised after they are reached. If there are no more waypoints left, the experiment is either completed or have failed, and control program can be stopped.

The right branch represents acquisition of position and spectrum data. When current time has zero millisecond component, spectrum data are requested. Data are received asynchronously from two MCB modules which are distinguished by ID. The program has to wait until data from both modules are correctly received. Then the measurement trajectory may be revised. The control program is stopped after some stop condition is fulfilled.

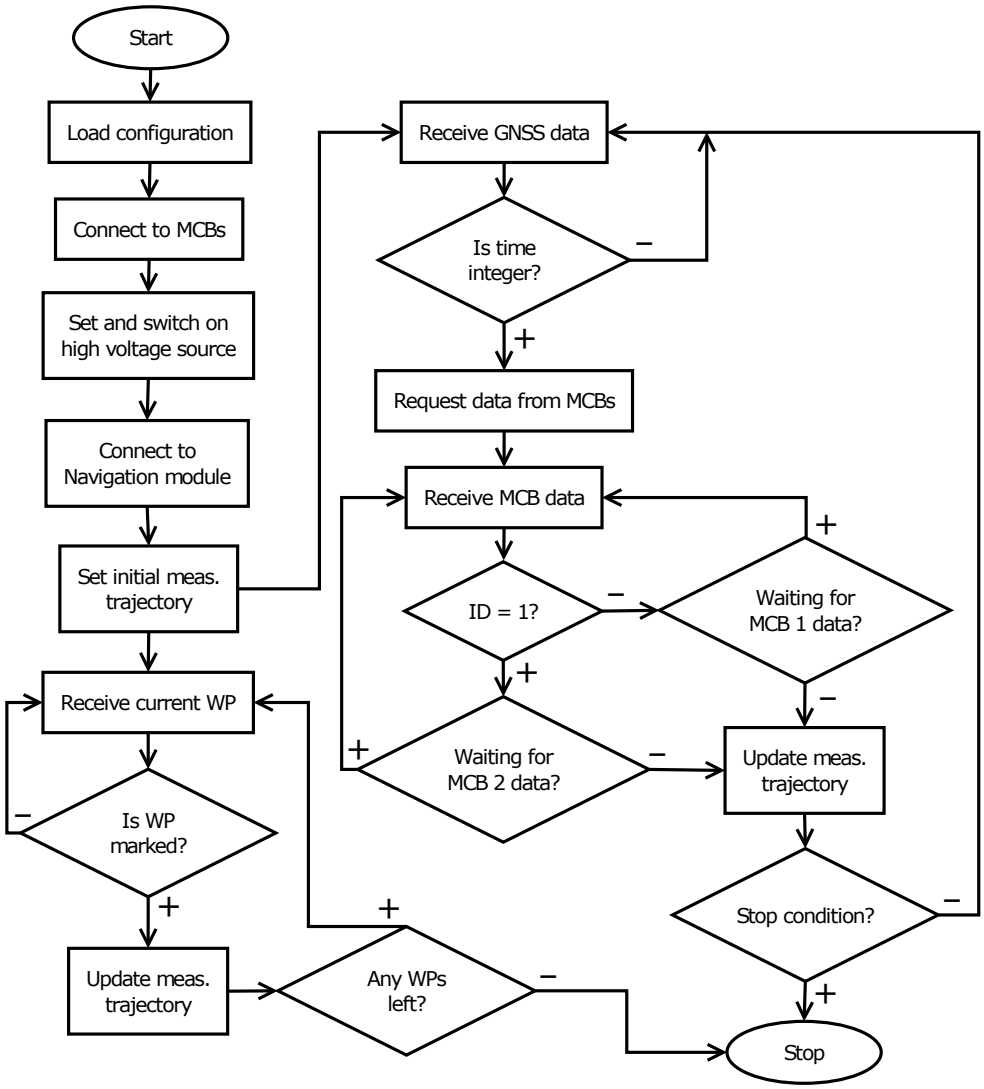


Fig. 2.6: Flowchart of the control software

### 2.5.2 Configuration

The whole system can be configured by XML file with defined nodes. The main node *radiation-config* contains at least seven inner nodes. Four of them serve for setting the gamma radiation detection system. Node *system-type* defines arrangement of a detection system, currently only *TwoDetector* system is supported. Pair of *detector-config* nodes store information about IP address, port, high voltage value and sensitivity for both the main and secondary detectors. Node *timer-config* contains measurement period and measurement time. The value of the first has to correspond with the update rate of GNSS receiver and is declared in milliseconds. The latter is set to inner timers of MCB modules and determines maximal spectrum acquisition time in seconds.

Another node, *gnss-config*, stores information for self-localization. Inner nodes define communication port and expected update rate. One of them also defines correction of measured yaw in degrees. If an axis of the robot and an axis of antennas form non-zero angle, the correction needs to be added to the measured value in order to get a value of yaw of the robot. In case of used arrangement, the correction value is $-30°$.

Node *navigation-config* serves for setting communication with navigation module. It contains IP address and port, identification code of the system and allowed navigation error. The last mandatory node, *measurement-mode* defines type of control algorithm. Other nodes are dependent on the algorithm and will be described in the following chapter. An example of configuration file can be found in the Appendix A.

# 3 ALGORITHMS FOR SOURCE LOCALIZATION

This charter introduces several algorithms that can be utilized for autonomous localization of gamma radiation sources using technical equipment described earlier. Some of them are not dependent on an arrangement of a detection system, others rely on directional sensitivity provided by the proposed two-detector system. All algorithms use total count for quantification of radiation intensity.

## 3.1 Mapping algorithm

Algorithm termed as mapping is an elementary algorithm for measurement of environmental quantities in the area of interest. Mapping is described in several papers, e. g. [12], [31] and [32]. The idea is to pass the whole area along parallel equidistant lines and measure the desired quantity periodically. If the line spacing and the robot's velocity are small enough, even subtle changes in the measured quantity can be noticed. In terms of radiation source localization – even weak sources can be found. That is apparently an advantage of the mapping. The disadvantage is that time requirements increase rapidly with size of the measured area. Schematic example of mapping trajectory in pentagonal area is shown in Fig. 3.1.

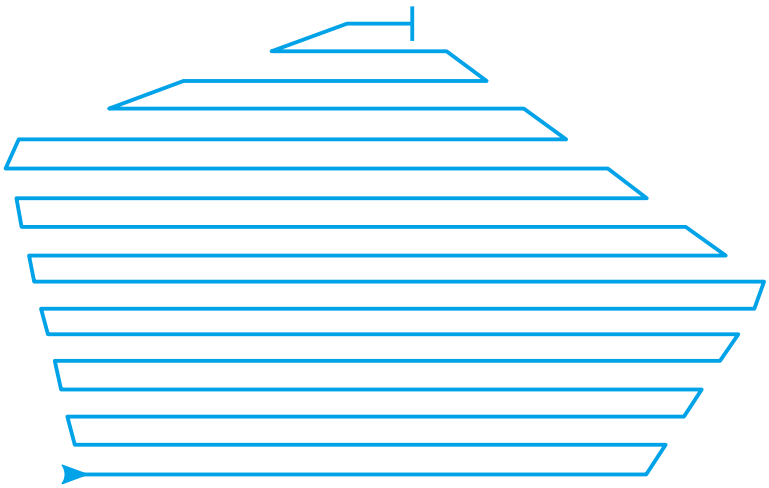

Fig. 3.1: Schematic of the mapping trajectory

Node *meas-trajectory* has to be added to the configuration file in order to set parameters for mapping. The measured area is defined by node *polygon* which contains a sequence of coordinates of polygon's vertices. The minimal count of vertices is three for triangular area. It is assumed that the sequence is ordered. Those coordinates are complemented by coordinates of the base station. Another parameter is

line spacing. Optimal value of spacing $d$ can be chosen based on the parameters of the weakest source to be found. In the worst case, the source is located exactly in the middle between two mapping lines. Dose rate generated by the source measured on the line should be at least three times higher than the background. Typical background rate is 0.17 µGy·h$^{-1}$(the value has been measured in designed experimental site), and therefore the source should generate approximately 0.5 µGy·h$^{-1}$in distance $\frac{d}{2}$. The following formula can be deduced:

$$d = 2\sqrt{\frac{\dot{D}_1}{0.5 \cdot 10^{-6}}} \qquad [\mathrm{m}; \mu\mathrm{Gy} \cdot \mathrm{h}^{-1}] \tag{3.1}$$

where $\dot{D}_1$ stands for dose rate generated by the weakest searched source in a distance of 1 meter – can be calculated from 1.1. For example, if cobalt-60 ($^{60}$Co) with activity 215 kBq should be found, $\dot{D}_1$ is equal to 79.6 nGy·h$^{-1}$, an therefore the spacing parameter should be 0.8 m.

The last parameter to be set determines the spacing of generated waypoints. It should be a value ranging from 0.2 to 1.0 meters.

### 3.1.1 Generation of waypoints

At first, waypoints are generated in local Cartesian coordinate system. Its x-axis is parallel to cirles of latitude, east is the positive direction. The y-axis is parallel to meridians, north is the positive direction. Points in WGS-84 have coordinates $(\phi, \lambda)$ where $\phi$ is latitude and $\lambda$ is longitude. Point in the local system have coordinates $(x, y)$. The z-coordinate is omitted because the problem is solved in plane.

The proposed transformation is based on rhumb lines [33]. Rhumb line is a path of constant bearing which crosses all meridians at the same angle and is a straight line in Mercator projection. Coordinates of the base station in WGS-84 are $(\phi_0, \lambda_0)$ and (0, 0) in the local system. The transformed point have coordinates $(\phi_1, \lambda_1)$ in WGS-84 and $(x_1, y_1)$ in the local system. When coordinates are transformed from WGS-84 to the local system, the x-coordinate is rhumb-line distance between base station and point at same latitude.

$$x_1 = \cos\phi_0 \cdot (\lambda_1 - \lambda_0) \cdot R \qquad [\mathrm{m}; \mathrm{rad}, \mathrm{rad}, \mathrm{rad}, \mathrm{m}] \tag{3.2}$$

where $R$ is Earth's radius and is equal to 6,371,008 m [34]. Similarly the y-coordinate is rhumb-line distance between base station and point at the same longitude.

$$y_1 = (\phi_1 - \phi_0) \cdot R \qquad [\mathrm{m}; \mathrm{rad}, \mathrm{rad}, \mathrm{m}] \tag{3.3}$$

When coordinates are transformed from the local system to WGS-84, coordinates are equal to coordinates of the destination point along rhumb line given distance and bearing from base station. Longitude is given as:

$$\lambda_1 = \lambda_0 + \frac{x_1}{R \cdot \cos\phi_0} \qquad [\text{rad}; \text{rad}, \text{m}, \text{m}, \text{rad}] \tag{3.4}$$

And latitude is given as:

$$\phi_1 = \phi_0 + \frac{y_1}{R} \qquad [\text{rad}; \text{rad}, \text{m}, \text{m}] \tag{3.5}$$

The goal is to find equations of parallel lines with set spacing, then find their intersections with polygon, and finally split line segments defined by the intersections into waypoints and order them. Coordinates of vertices are given in WGS-84 and have to be transformed first. Then it is possible to find equations of polygon's edges. Fundamental principles of the analytic geometry are taken from [35]. A majority of the following equations is deduced by the author of this thesis.

All lines in this thesis are described by a general form of equation of a line, that is: $ax + by + c = 0$, where $[a, b]$ is a normal vector of the line. Given two vertices $(x_1, y_1)$ and $(x_2, y_2)$, the corresponding edge is described as:

$$a = y_1 - y_2 \tag{3.6a}$$

$$b = x_2 - x_1 \tag{3.6b}$$

$$c = -ax_1 - by_1 = -ax_2 - by_2 \tag{3.6c}$$

The edge defined by first two vertices is denoted as *base line*. The first vertex represent a point where the measurement trajectory begins. The next step is to find the vertex that is farthest from the base line. Distance of point $(x_1, y_1)$ from line can be calculated by the following formula:

$$d = \frac{|ax_1 + by_1 + c|}{\sqrt{a^2 + b^2}} \tag{3.7}$$

The last parallel line should pass through this farthest vertex. If the distance is not integer multiple of desired line spacing, there are two options. The distance of some two lines will differ from others, or all lines will be equidistant with slightly different spacing. The latter option is used here. A line perpendicular to base line given by $[a_1, b_1, c_1]$ passing through point $(x_1, y_1)$ is found as:

$$a = b_1 \tag{3.8a}$$

$$b = -a_1 \tag{3.8b}$$

$$c = a_1 y_1 - b_1 x_1 \tag{3.8c}$$

The intersection of lines given by $[a_1, b_1, c_1]$ and $[a_2, b_2, c_2]$ has the following coordinates:

$$y = \frac{c_1 a_2 - c_2 a_1}{b_2 a_1 - b_1 a_2} \tag{3.9a}$$

$$x = \frac{-c_1 - b_1 y}{a_1} \tag{3.9b}$$

If the denominator in Eq. 3.9a is equal to zero, intersection does not exist. In this case, it has to exist because the lines are perpendicular. The line segment between points $(x_1, y_1)$ and $(x_2, y_2)$ can be easily splitted into $n$ equidistant points. If the length of the line segment is $d$ and desired point spacing is $s$, the number of points is:

$$n = \left\lfloor \frac{d}{s} \right\rfloor + 1 \tag{3.10}$$

Coordinates of $i$-th point where $0 \leq i < n$ are given by these equations:

$$x_i = x_1 + i\frac{x_2 - x_1}{n - 1} \tag{3.11a}$$

$$y_i = y_1 + i\frac{y_2 - y_1}{n - 1} \tag{3.11b}$$

Then perpendicular lines passing through each of these points using Eq. 3.8. These lines are parallel to the base line, and are equidistant. In order to find intersections of the line and polygon, it is necessary to examine if intersections exist for each edge. The edge is a line segment described by line equation and two distint end points $(x_1, y_1)$ and $(x_2, y_2)$. Intersection with the line $(x, y)$ can be gained from Eq. 3.9. Intersection with the line segment exists under the following condition:

$$x_1 \leq x \leq x_2 \wedge y_1 \leq y \leq y_2 \tag{3.12}$$

assuming $x_1 < x_2 \wedge y_1 < y_2$. The problem is solved analogically for other relations between end points. Knowing the intersections, parallel line segments may be splitted to sequences of waypoints with desired spacing according to Eq. 3.10 and Eq. 3.11. The waypoints have to be ordered in a way so that neighboring sequences of waypoints have opposite directions. Finally, the waypoints are transformed to WGS-84.

Proposed algorithm for generation of waypoints is generally applicable for all convex polygons. It can be used also for some concave polygon when all lines parallel to the base line have maximally two intersections with the polygon. Therefore, it depends not only on the shape of the polygon but also on choice of the base line.

### 3.1.2 Interpolation of the source position

Set of scattered points is a result of the mapping. Those are not very suitable for visualization and further map processing, e.g. conversion to 3D point cloud. Therefore, calculation of radiation intensity (either total count or dose rate) in points in regular grid is needed. This can be done for example through Delaunay triangulation [36]. This interpolation is implemented in `scatteredInterpolant` class in MATLAB. One of three interpolation methods may be specified – either linear, nearest neighbor or natural neighbor interpolation. The linear one is used in this thesis. After performing interpolation, the data can be visualized and position of sources can be marked manually.

Automatic computation of the position consists of three steps. First, local maxima need to be found. To eliminate false positive detections, custom 2D peak detector is used and tuned with data from real experiments. Basically, each point from data set is compared to its neighborhood in a manner shown in Fig. 3.2, and its absolute value is compared to a threshold. Distance between cells is 0.04 m. Value of parameter $k$ is chosen in range from 0.95 to 1.00, parameter $Th$ is set to double of the lowest measured intensity.

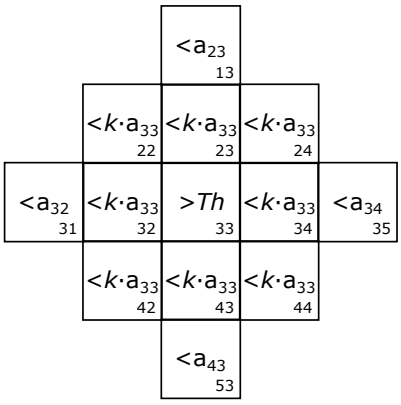


Fig. 3.2: A scheme of kernel for peak detection

Afterwards, measured data points within defined radius around each maximum are selected for further processing. These points are then fitted with suitable function. Theoretical dependency of measured radiation intensity on distance from source located in the $(x_s, y_s)$ is described as:

$$I = \frac{K}{(x - x_s)^2 + (y - y_s)^2 + h^2} \tag{3.13}$$

where $K$ is constant and $h$ represents height of the detector above surface. In real measurement the function is distorted by dead time and other effects. It is

possible to use paraboloid (quadratic function) as a rough approximation because the fitting can be easily performed analytically, using least squares method [37]. The approximation in 2D is illustrated in Fig. 3.3. The similarity of both function should be sufficient to provide satisfactory result within limited radius.

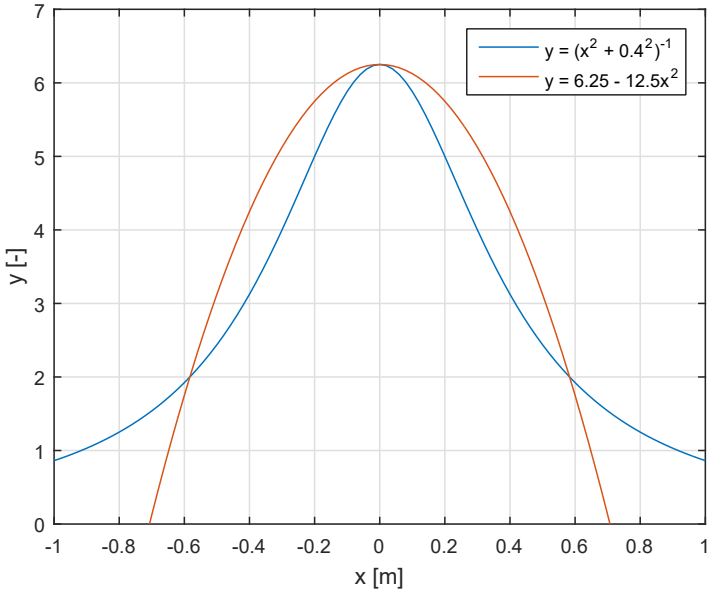


Fig. 3.3: A comparison with fitting function

Paraboloid is given by the following formula [38]:

$$z = f(x, y) = p_1 + p_2 x + p_3 y + p_4 x^2 + p_5 xy + p_6 y^2 \tag{3.14}$$

With set of points $(x, y, z)$ where $z$ is intensity parameters of paraboloid can be calculated by solving matrix equation [38]:

$$p = \begin{bmatrix} p_1 \\ p_2 \\ p_3 \\ p_4 \\ p_5 \\ p_6 \end{bmatrix} = \begin{bmatrix} \mathbf{1} & \boldsymbol{x} & \boldsymbol{y} & \boldsymbol{x^2} & \boldsymbol{xy} & \boldsymbol{y^2} \end{bmatrix}^{-1} \boldsymbol{z} \tag{3.15}$$

where components of the matrix on the right side are column vectors composed of points' coordinates. The condition for extreme is where partial derivatives with respect both to $x$ and $y$ are equal to 0.

$$\frac{\partial z}{\partial x} = \frac{\partial z}{\partial y} = 0 \tag{3.16}$$

From these equations it is possible to deduce formulas for computing $x$ and $y$ coordinates of the maximum of paraboloid described by equation 3.14. They also correspond with coordinates of the searched source.

$$x_{max} = \frac{p_3 p_5 - 2p_2 p_6}{4p_4 p_6 - p_5^2} \tag{3.17}$$

$$y_{max} = \frac{p_2 p_5 - 2p_3 p_4}{4p_4 p_6 - p_5^2} \tag{3.18}$$

## 3.2 Strong source search algorithm

In situation when finding only one source is required and timing is important following algorithm may be used. It is based on dynamic change of trajectory in accordance with measured data. It is assumed that the source is strong enough to be detectable in considerable part of the scanned area.

First, the same trajectory as in case of map building is planned. After the robot reaches end of a line the data are searched for peak in radiation intensity. Peak is defined as data point which has higher total count than its neighbouring points and also $k$ times higher total count than the line's minimum (peak has to exceed radiation background). If peaks are found in two neighbouring lines and their positions correspond, then the trajectory is altered and new waypoints are generated in direction perpendicular to current line passing through center of peak projections to this line. A projection is given by intersection (3.9) of the line which it is projected to and a perpendicular line (3.8) passing through the peak. The robot follows the line in the new direction denoted as *normal line* until another peak in measured radiation intensity occurs.

Afterwards, final sequence of waypoints denoted as *loop* is generated. The purpose of a loop is to get data for more precise interpolation of the source position. That is achieved if data lines form approximately right angle and have intersection close to the source. Waypoints for a loop are generated within radius that can be set through configuration file. The radius should correspond to an interpolation radius. A schematic example of the measurement trajectory is shown in Fig. 3.4

## 3.3 Characteristics of a direction-sensitive system

To verify directional sensitivity of proposed two-detector system, following experiments were set. In the first experiment the detectors were placed in vertical position with 8 cm distance of its centers. As a radiation source $^{60}$Co with activity approximately 50 kBq was used. Such a weak source was picked in order to measure

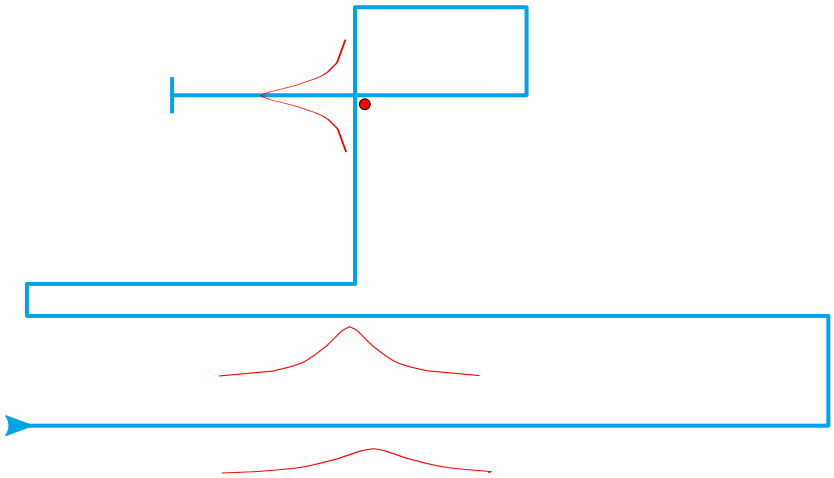

Fig. 3.4: Schematic of the strong source search trajectory

multiple characteristics in the laboratory safely. The experiment was performed with the source located in angular distances from 0° to 330° with 30° step and in 17.5 cm distance from center of the system. All measurements lasted 40 s with sampling period 1 s.

Angular dependence of the ratio of second detector readings to first detector reading can be found in picture 3.5. Two curves are plotted there – the orange one represents measurement during which 4 mm thick lead plate was present between detectors. Usage of shielding is inspired by [39]. The spread of values in the worst case scenario for shielded option is also charted. The shape of a function resembles the theoretical one satisfyingly. The directional sensitivity is better with shielding, it is therefore used in further experiments.

The second experiment was performed with detectors mounted on the robot. The purpose was to quantify how much radiation is attenuated by the robot's body. A stronger source was used – caesium-137 ($^{137}$Cs) with activity approximately 1 MBq. The source was located in angular distances from 0° to 350° with 10° step and in 120 cm distance from the first, and afterwards also from the second detector. Again, all measurements lasted 40 s with sampling period 1 s.

Directional characteristic of the used radiation detection system was evaluated. It is shown in polar plot in Fig. 3.6. The robot's forward direction is denoted as 0°, number of mean measured counts relative to forward direction is at radial axis in percent. Thanks to system geometry and shielding lead layer, both detectors are differently sensitive to radiation coming in different incident angles. The radiation coming from angles around 180° (through the robot) is notably attenuated.

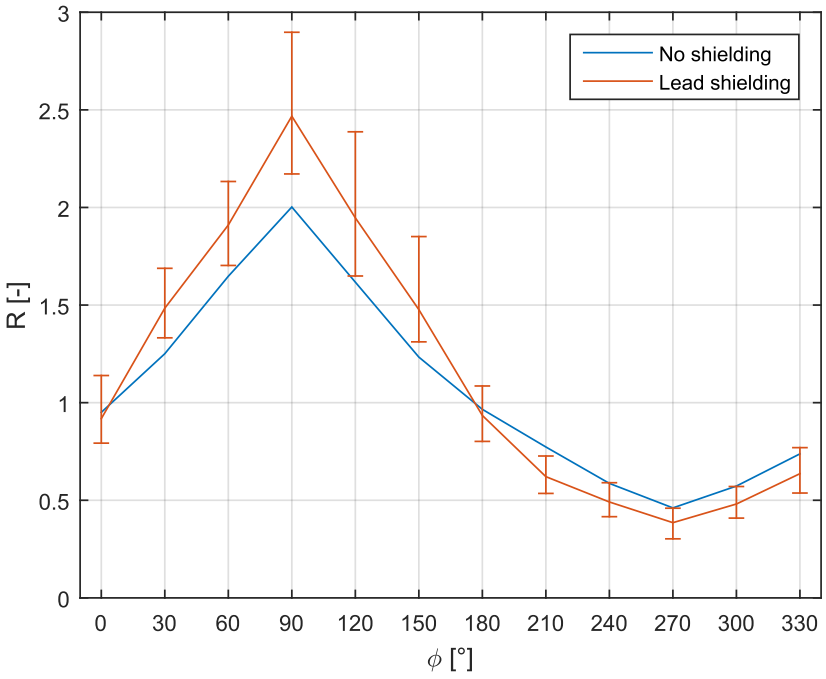


Fig. 3.5: Angular dependence of the ratio of values measured by detectors

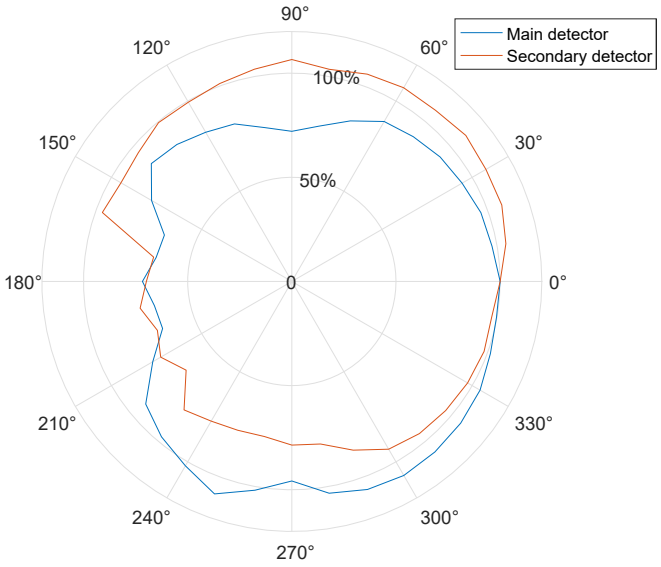


Fig. 3.6: Directional characteristics of the used detectors

## 3.4 Circular algorithms

When a robot rides through a closed loop, all possible angles between detectors and radiation sources are taken. The resulting data set has greater information value about position of sources than single measurement. The basic shape of a closed

loop is a circle. The idea behind these algorithms is exploration of the area of interest through riding circles. The data from circles can be evaluated in order to get estimation of direction in which the source should be searched for, or even estimation of the source's location. It is worthwhile to develop algorithms incrementally from easy cases to the more exacting ones. Elements common to all proposed circular algorithms are described first.

### 3.4.1 Generation of waypoints

A standard form for the equation of circle is used to describe all circles in this thesis.

$$(x - x_c)^2 + (y - y_c)^2 = r^2 \tag{3.19}$$

Where $(x_c, y_c)$ are coordinates of circle center and $r$ is its radius. Parameters of a circle can be described by a vector $[x_c, y_c, r]$. The waypoints are generated in counterclockwise direction, therefore the main detector is aimed outside of a circle and the secondary detector inside. It is convenient for a robot to approach the circle along its tangent, because when it reaches the circle, no additional maneuvers are needed. First it is necessary to find points of tangency for a line passing through the current position of robot $R(x_R, y_R)$. The points are given as intersections of a circle and the polar line to point $R$. They can be obtained by solving the following system of equations:

$$x^2 + y^2 = r^2 \tag{3.20a}$$

$$(x_R - x_c)x + (y_R - y_c)y - r^2 = 0 \tag{3.20b}$$

Where Eq. 3.20b represent equation of a polar line. The solution leads to quadratic equation.

$$\left[1 + \frac{(x_R - x_c)^2}{(y_R - y_c)^2}\right] x^2 - \left[\frac{2r^2(x_R - x_c)}{(y_R - y_c)^2}\right] x + \left[\frac{r^4}{(y_R - y_c)^2} - r^2\right] = 0 \tag{3.21}$$

The $y$ coordinates are defined by:

$$y = \frac{r^2 - (x_R - x_c)x}{(y_R - y_c)} \tag{3.22}$$

Afterwards it is needed to select point of tangency which is located in the right half-plane. It has to satisfy following inequality:

$$(y_R - y_c)x + (x_c - x_R)y - (y_R - y_c)x_R - (x_c - x_R)y_R < 0 \tag{3.23}$$

The generation of waypoints between current position and a point of tangency is described by Eq. 3.10 and Eq. 3.11. It is reasonable to omit the first half of waypoints in order to provide the robot with a maneuvering space because it is not probable that it has a proper yaw. When the current position of robot is inside the circle, it is not possible to approach the circle along tangent. The most convenient way is then using an arc. A minimal difference between the robot's yaw at the end of arc and at the beginning of circle should be achieved. The robot lies inside circle when inequality is satisfied:

$$(x - x_c)^2 + (y - y_c)^2 < r^2 \tag{3.24}$$

The arc lies on some circle which needs to be defined first. A ray with current position as an initial point and current yaw as a direction is found. Then intersection of the ray and circle is calculated. Half of a distance between current position and the intersection is going to be the radius of the arc circle. Coordinates of the current point are then translated by the radius in a direction perpendicular to current yaw. The new point can be the center of the arc circle if intersections between the original circle and potential arc circle exists. If the intersections do not exists, the radius is increased and the process is repeated until suitable arc center is found. Intersections of circle $[x_1, y_1, r_1]$ and circle $[x_2, y_2, r_2]$ exist if the following quadratic equation has solution:

$$\left[1 + \frac{(x_2 - x_1)^2}{(y_2 - y_1)^2}\right] x^2 - \left[\frac{(x_2 - x_1)c}{(y_2 - y_1)^2}\right] x + \left[\frac{c^2}{4(y_2 - y_1)^2} - r_1^2\right] = 0 \tag{3.25}$$

where

$$c = r_1^2 - r_2^2 + (x_2 - x_1)^2 + (y_2 - y_1)^2 \tag{3.26}$$

The $y$ coordinates are then given by:

$$y = \frac{c - 2(x_2 - x_1)x}{2(y_2 - y_1)} \tag{3.27}$$

When the arc circle is known so are the endpoints of the arc (current position $(x_1, y_1)$ and intersection of the circles $(x_2, y_2)$), waypoints along the arc may be generated. Angular coordinate of a point at circle $[x_c, y_c, r]$ is given by function:

$$\phi(x, y) = \begin{cases} \arccos \frac{x - x_c}{r}, & \text{if } y \leq y_c \\ \arccos \frac{x_c - x}{r}, & \text{otherwise} \end{cases} \tag{3.28}$$

Count of the waypoints between endpoints is:

$$n = \left\lfloor \frac{|\phi(x_2, y_2) - \phi(x_1, y_1)|r}{s} \right\rfloor + 1 \tag{3.29}$$

where $s$ is waypoint spacing. Coordinates of $i$-th point where $0 \leq i \leq n$ are given by these equations:

$$\phi_i = \phi(x_1, y_1) + i\frac{|\phi(x_2, y_2) - \phi(x_1, y_1)|}{n} \tag{3.30a}$$

$$x_i = x_c + r\cos\phi_i \tag{3.30b}$$

$$y_i = y_c + r\sin\phi_i \tag{3.30c}$$

Finally, waypoints at the circle are generated in the same manner as in case of the arc, the only difference is that start and end points are identical. The start point is either a point of tangency in case the current position is outside circle, or an end point of arc otherwise. Obviously, the waypoints need to be transformed to WGS-84 in the end.

When the area of interest is explored from multiple circles, the preceding procedure is repeated for each one. The nearest one of the remaining circles is selected for processing, assuming the current position is equal to the end point of the previous circle. An example of generated sequence of waypoints (before they are transformed to WGS-84) for six circles and initial position $(48, -24)$ and initial yaw 210° is shown in Fig. 3.7.

### 3.4.2 Estimation of direction

Assuming the robot maintains a constant speed once it reaches a circle, a cyclic signal with equidistant data points is result of the measurement. According to theory, measured total count coming from a source should be highest in intersection of the circle and the ray connecting the circle center with position of the source (*directional point*). Total count measured in neighboring points should be smaller because of their larger distance from the source. Also, the ratio of total count measured by main and by secondary detector should be extreme in the directional point. Either way, it is necessary to find dominant peaks in selected quantity – sum or ratio of total counts. Utilization of sum of total counts is assumed further in the text.

Once the peaks are identified, it is convenient to fit its neighborhood by appropriate function. There are several reasons for doing that. First, due to dead time, the point in right direction may not have the maximal total count. Also, it is

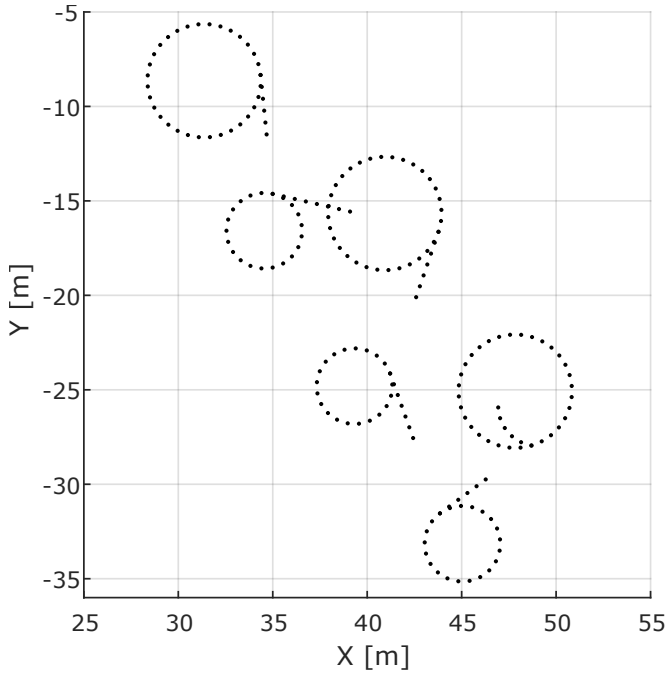


Fig. 3.7: Generated sequence of waypoints for six circles

probable that the actual maximum is somewhere between the samples. An interpolation provides subsample precision. For similar reasons as in Sec. 3.1.2 a quadratic function is used.

Neighborhood for interpolation is defined by a threshold which is relative to peak value. First endpoint is a first point on the left from a peak which has lower value than the threshold, analogically second endpoint is a first point on the right from a peak which has lower value than the threshold. When the endpoints cannot be found, no source is detected from the circle. Parameters of the interpolation function $ax^2 + bx + c$ is computed by the least squares method [40].

$$\begin{bmatrix} a \\ b \\ c \end{bmatrix} = \begin{bmatrix} \sum_{i=1}^{n} x_i^4 & \sum_{i=1}^{n} x_i^3 & \sum_{i=1}^{n} x_i^2 \\ \sum_{i=1}^{n} x_i^3 & \sum_{i=1}^{n} x_i^2 & \sum_{i=1}^{n} x_i \\ \sum_{i=1}^{n} x_i^2 & \sum_{i=1}^{n} x_i & n \end{bmatrix}^{-1} \begin{bmatrix} \sum_{i=1}^{n} y_i x_i^2 \\ \sum_{i=1}^{n} y_i x_i \\ \sum_{i=1}^{n} y_i \end{bmatrix} \tag{3.31}$$

where index of point in measured sequence represents its $x$ value, and $n$ is count of points. Index of maximal value of the quadratic function $i_{max}$ is given as:

$$i_{max} = -\frac{b}{2a} \tag{3.32}$$

Due to asymmetric directional characteristics of detectors and fact that measurements are took in motion, there is a shift between the computed and actual

maximum. It can be compensated by adding peak shift correction value $i_{corr}$ to $i_{max}$. A position of directional point $(x_d, y_d)$ can be get by linear interpolation:

$$i_d = i_{max} + i_{corr} \tag{3.33a}$$

$$x_d = x(\lfloor i_d \rfloor) + (i_d - \lfloor i_d \rfloor)[x(\lceil i_d \rceil) - x(\lfloor i_d \rfloor)] \tag{3.33b}$$

$$y_d = y(\lfloor i_d \rfloor) + (i_d - \lfloor i_d \rfloor)[y(\lceil i_d \rceil) - y(\lfloor i_d \rfloor)] \tag{3.33c}$$

If the total count measured by the main detector in peak is higher than the corresponding value measured by a secondary detector, the source is located outside the circle. Then its direction from the directional point can be expressed using Eq. 3.28. Otherwise the source lies inside the circle and its direction is opposite.

### 3.4.3 Navigation to source

Once the initial point and direction are known, it is possible to navigate the robot towards the source. Trajectory is denoted as *directional line*, although it is not a line because the direction is altered as new data are being measured.

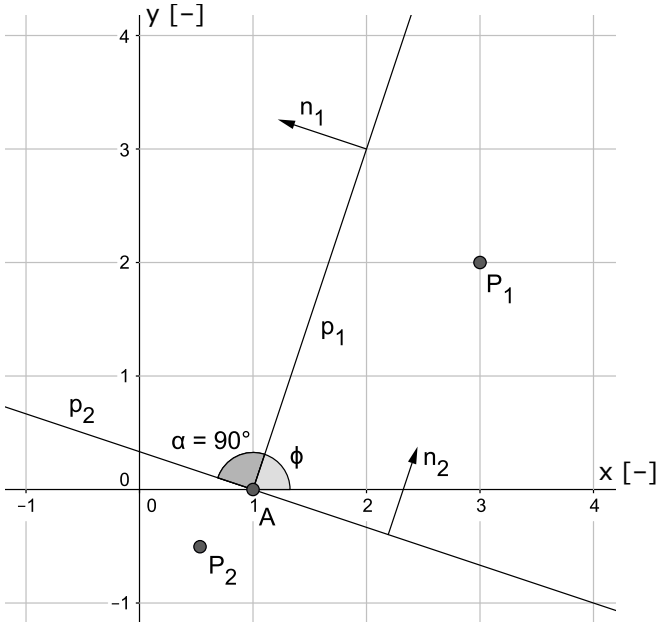


Fig. 3.8: Determining a direction of point

Basic geometric primitive which is used here is a ray which is described by initial point $A(x_a, y_a)$ and direction $\phi$. There is no analytic expression for a ray, it may be described by an equation of a line $p_1$ at which the ray lies, and auxiliary

perpendicular line $p_2$ passing through the initial point. Both lines are shown in Fig. 3.8. Their equations may be expressed as:

$$p_1 : \tan(\phi)x - y + y_d - \tan(\phi)x_d = 0 \tag{3.34a}$$

$$p_2 : \begin{cases} -x - \tan(\phi) + \tan(\phi)y_d + x_d = 0, & \text{if } -90° < \phi < 90° \\ x + \tan(\phi) - \tan(\phi)y_d - x_d = 0, & \text{if } 90° < \phi < 270° \end{cases} \tag{3.34b}$$

$$\tag{3.34c}$$

Purpose of the auxiliary line is in determining if a point lies in the same half-plane as the ray ($P_1$) or in the opposite one ($P_2$). If the following inequality is satisfied, both point and ray are in same half-plane.

$$p_2(x_p, y_p) > 0 \tag{3.35}$$

The reason is that the point lies in a direction of normal vector of the auxiliary line. Using this technique, it is possible to find intersection of a ray and polygon. Initial directional line is composed of waypoints generated between the directional point $(x_d, y_d)$ and intersection with polygon in corresponding direction $\phi$. It is thereby assured that no waypoint is generated outside polygon which must not be left by the robot. One extra waypoint is generated in the opposite direction in order to provide the robot with maneuvering space so it reaches the beginning of the directional line with correct yaw. Coordinates of this waypoint are defined by:

$$x = x_d + d\cos\phi \tag{3.36a}$$

$$y = y_d + d\sin\phi \tag{3.36b}$$

where $d$ is desired distance from the directional point. Since the first data point is measured at the directional line, a relative direction of the source is evaluated with each following measurement. Given current readings from the main detector $M(t)$ and from secondary detector $S(t)$, as well as the previous readings $M(t-1)$, $S(t-1)$, it is possible to decide whether the source is located in front of the robot or whether it is on the right, resp. on the left. When the following condition is fulfilled, the source is detected on the right:

$$[M(t) \geq K \cdot S(t)] \wedge [M(t-1) \geq S(t-1)] \wedge \left[\frac{M(t)}{S(t)} \geq \frac{M(t-1)}{S(t-1)}\right] \tag{3.37}$$

where $K$ represents insensibility which should suppress influence of noise. Condition for detecting the source on the left is analogical:

$$[S(t) \geq K \cdot M(t)] \wedge [S(t-1) \geq M(t-1)] \wedge \left[\frac{S(t)}{M(t)} \geq \frac{S(t-1)}{M(t-1)}\right] \tag{3.38}$$

Both conditions are appended by a secondary one.

$$[M(t) + S(t)] \geq [M(t+1) + S(t+1)] \tag{3.39}$$

which assures that in case that the robot already passed the source, trajectory is not updated. The reason is that previous conditions could fail when the source is behind a robot due to deformation of the directional characteristics. When both primary and secondary conditions are fulfilled, direction is updated by $+\Delta\phi$, resp. $-\Delta\phi$. Then a new sequence of waypoints is generated from current position to intersection with polygon in the new direction.

There are two terminating conditions for this partial algorithm. The first one is fulfilled when the source has been provably passed by the robot. In that case it is possible to interpolate data points measured at direction line with quadratic function in a similar way as in Sec. 3.4.2. Afterwards, the source is marked as *found*, and the final loop may be planned in a manner described in Sec. 3.2. It is possible to omit loops in configuration file.

The second terminating condition is fulfilled when the source could not be found within allowed distance. If the source is located outside the circle, navigation is terminated when final generated waypoint at an edge of the polygon has been reached. Otherwise, the maximal allowed distance is equal to a diameter of the circle. Either way, the source is marked as *not found*.

### 3.4.4 First circular algorithm

The simplest situation is when only one radiation source is present in the area of the interest, and the area is small enough to be covered by single circle. This algorithm represents an alternative to strong source search algorithm presented in Sec. 3.2. Since only one peak is expected in circle data points, it can be easily found as the maximal value in data set. After the direction is estimated, the source is navigated to using the described continuous update of trajectory. Schematic example of such measurement trajectory is shown in Fig. 3.9. Actual location of the source is marked by the red point, the black line represents initial estimation of direction.

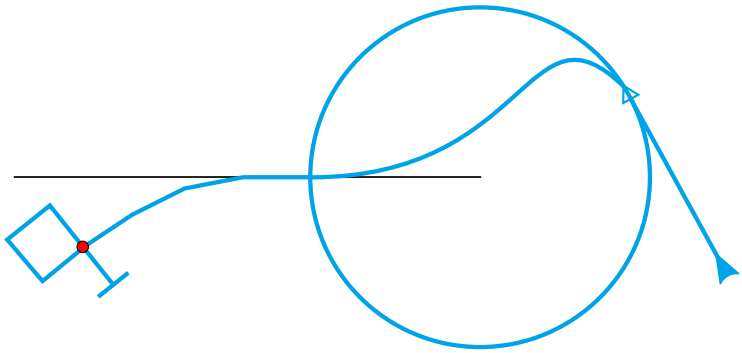

Fig. 3.9: Schematic of the first circular algorithm trajectory

### 3.4.5 Second circular algorithm

A slightly more complicated is a case when multiple source are present in the area of interest, but all of them may be detected from a single circle and are sufficiently separated by angle. Therefore, development of peak detector is needed. Real data are very noisy, thus the detector needs to be robust. *Simple peak* is defined as a point which has value (in this case total count) greater than its two neighboring points. A large amount of simple peaks could be detected in real data, most of them would not match actual radiation source. What is needed to be searched for are *prominent peaks*.

Algorithm integrated in MATLAB's `findpeaks` function is adapted [41]. Exemplary cyclic signal can be seen in Fig. 3.10 and the peak detection will be illustrated on it. The signal has three simple peaks (1, 2, 3) and three valleys (a, b, c). Peaks are evaluated using a reference level that has to be defined first. In order to find it, the following steps are repeated for each peak:

1. Extend a horizontal line from the peak to the left and right until the line crosses the signal (a point with greater or equal value is crossed).
2. Find the minimum of the signal in each of the two intervals defined in Step 1. This point is one of the valleys.
3. The higher of two interval minima specifies the reference level.

Peaks shown in Fig. 3.10 would have the following reference levels:

1: a
2: c
3: c

If the peak amplitude is greater or equal to the reference value multiplied by desired relative prominence, the peak is accepted as prominent. If the relative prominence matches the threshold for interpolation by quadratic function, it is assured the interpolation may be done.

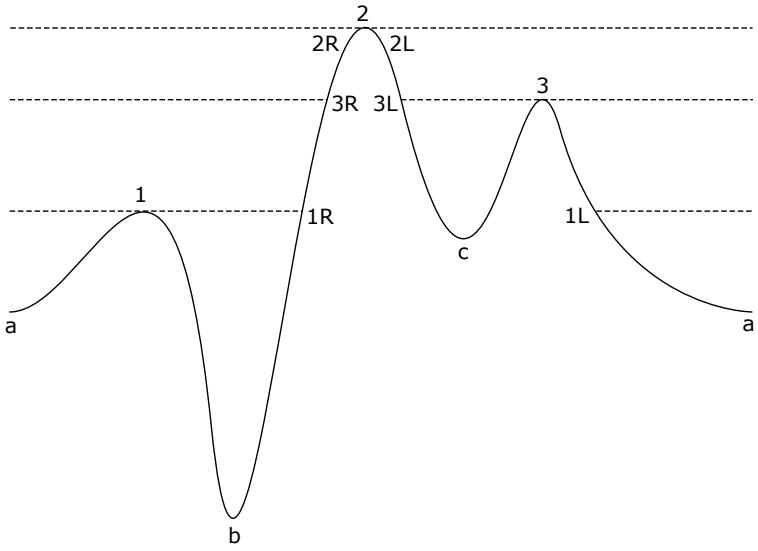


Fig. 3.10: Illustration for finding peaks

After all peaks are evaluated, direction of multiple sources can be estimated. The estimations may be ordered for example by the matching peak amplitude. Higher amplitude corresponds to either stronger source or closer source. In first case, stronger sources are located first. In other case, it is convenient to detect closer sources first, because the robot has to return to the circle after a source is found.

Localization of the sources is performed in sequence using the earlier described navigation to source algorithms for each one. After one source is marked as found or not found, the robot returns to the beginning of another directional line located on the circle. Algorithm ends when all potential sources are explored. Schematic example of such trajectory can be seen in Fig. 3.11.

### 3.4.6 Third circular algorithm

Third algorithm is concerned with a situation when the area of interest cannot be explored by single circle, therefore multiple circles are employed. However, an important simplification is assumed – the sources do not interfere with each other. In other words, every source evokes prominent peak on only one circle.

First, the robot rides round all the circles. The data are then evaluated in a familiar way – directions of sources are estimated and then each of the potential sources is tried to be located. Once the source is (or is not) located, it is convenient to proceed with a source that has directional point with the lowest distance from the current position. An example of such trajectory is shown in Fig. 3.12.

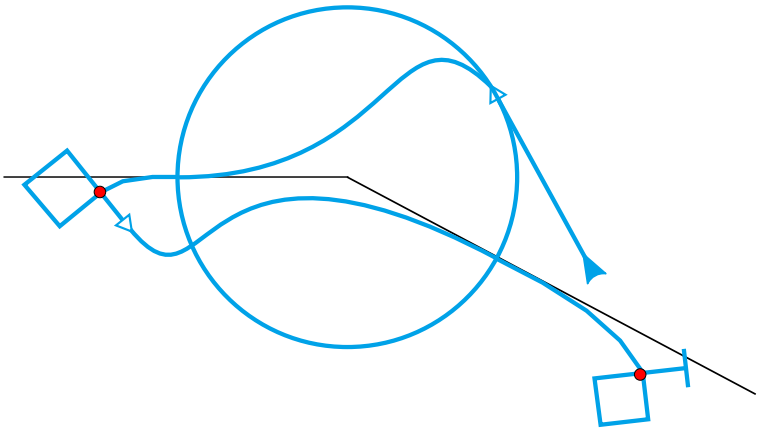

Fig. 3.11: Schematic of the second circular algorithm trajectory

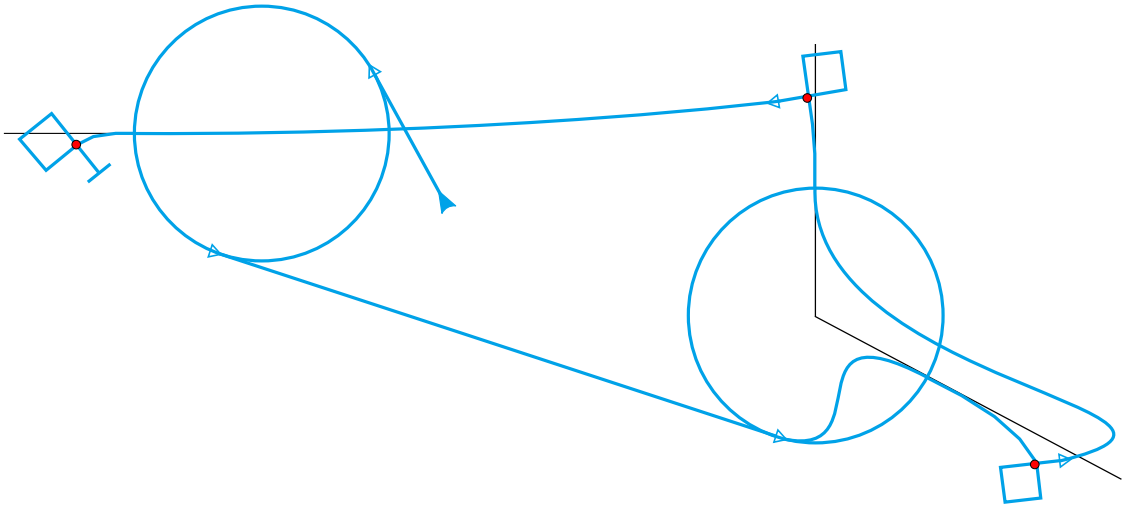

Fig. 3.12: Schematic of the third circular algorithm trajectory

### 3.4.7 Fourth circular algorithm

The last proposed algorithm covers the most general case – the area of interest is explored from multiple circles, while several sources are present and interfere with each other. That, on the other hand, allows development of algorithm which estimates the location of the source, not only its direction.

The algorithm is described using a situation illustrated in Fig. 3.13. It can be seen that three circles denoted as 1, 2 and 3 are present, as three radiation sources. Seven peaks are found on the circles in total. Each of them has corresponding ray marking the direction of source, these rays are illustrated by black lines. Estimation of the location of the sources may be divided into the following steps:

1. For each ray, intersections with other rays are found.

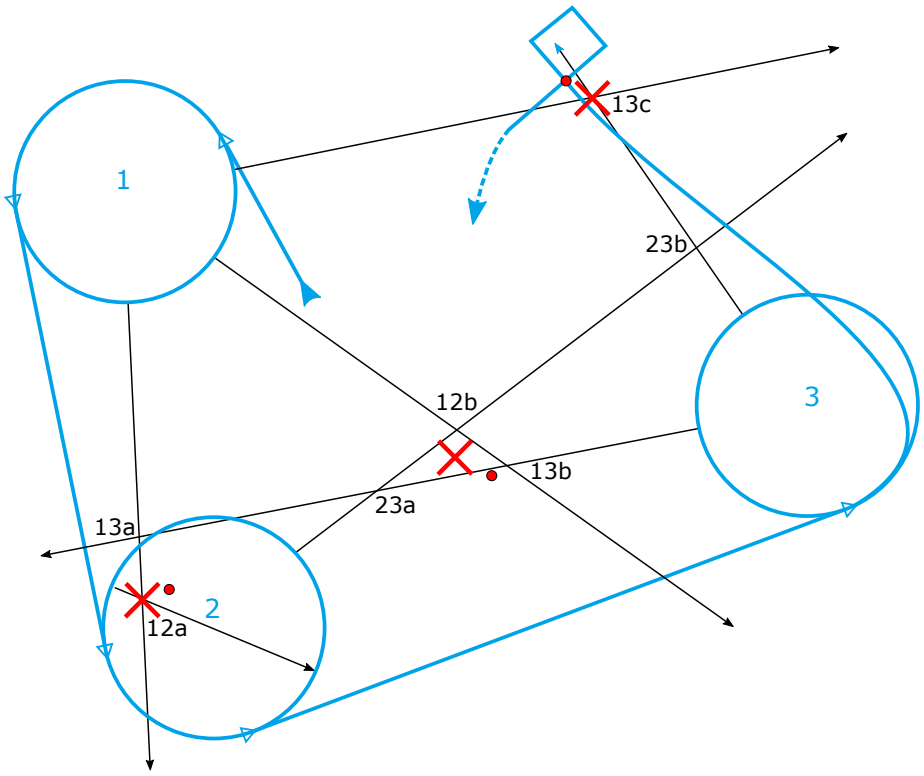


Fig. 3.13: Schematic of the fourth circular algorithm trajectory

2. Discard all intersections located outside the area of interest.
3. If some ray corresponds to the source detected inside the circle, discard its intersections outside the circle.
4. For each pair of rays, accept only one intersection that is nearest to one of theirs initial points and second nearest to the other one at most.

The area of interest is defined by ordered sequence of polygon vertices as it was stated earlier in Sec. 3.1. To examine whether a point $A$ lies inside or outside polygon, an algorithm called ray casting may be utilized [42]. First, a ray originating in the examined point is found. Then, all intersection of this ray and polygon are counted using Eq. 3.9, Eq. 3.12 and Eq. 3.35. If the number of intersections is even, the point lies outside a polygon. Otherwise, it is inside. All intersections satisfying this conditions are marked in Fig. 3.13, using code *cc*#, where *cc* are labels of two circles where the intersecting rays are originated on, and # is order in sequence. Result of the selection algorithm is shown in Tab. 3.1.

After an application of the algorithm, there are still five intersections left although only three sources are present in the area. The reason is that intersection 12b, 13b and 23a mark the same source but, due to inaccuracy in measurement, the matching rays do not intersect in a single point. A possible solution is to iteratively

Tab. 3.1: Overview of found intersections

| **Intersection** | **Accepted/discarded** |
|---|---|
| 12a | Accepted. |
| 12b | Accepted. |
| 12c | Discarded because it lies outside circle 2. |
| 13a | Discarder because intersections 13b and 23a are nearer to the initial point on circle 3. |
| 13b | Accepted. |
| 13c | Accepted. |
| 23a | Accepted. |
| 23b | Discarded because intersections 23a and 12b are nearer to the initial point on circle 2. |

replace intersections which have a distance lower than some threshold $D_{min}$ by theirs average coordinates until all intersections are well separated.

1. Intersections 12b and 13b are united into point $P_1$.
2. Intersection 23a and point $P_1$ are united into point $P_2$.
3. All remaining intersections and points have mutual distance greater than $D_{min}$.

Final estimations of sources' position are marked with red crosses. In order to maintain the figure well arranged, only one directional line with matching loop is displayed. After the source is found, the robot would proceed to another one and finally to the third one.

It is possible that some source is located somewhere nearby the edge of the area and is detectable from only one circle. In that case, direction of the source is still known and it can be found by means presented in the previous three algorithms. Flowchart describing whole algorithm is shown in Fig. 3.14.

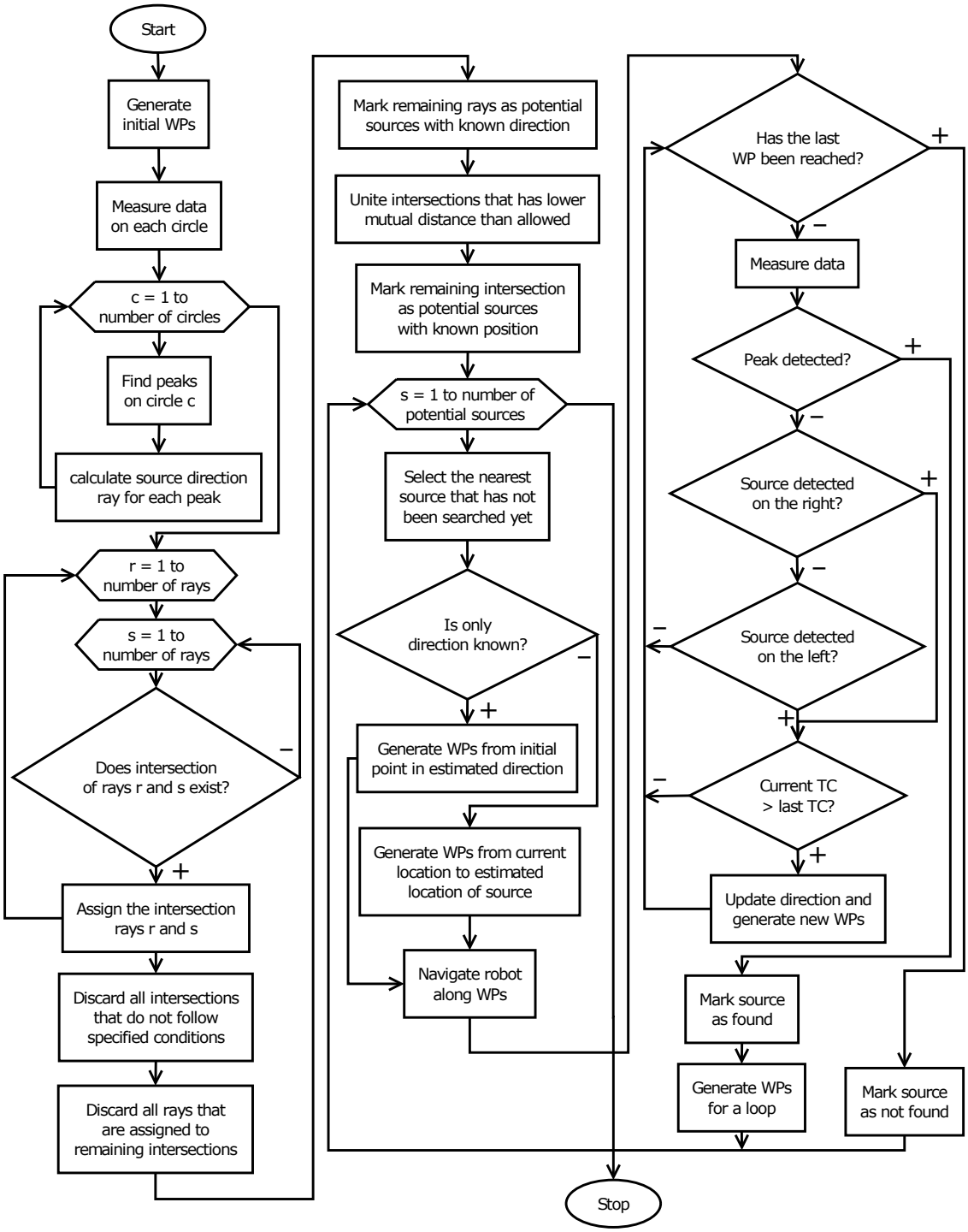


Fig. 3.14: Flowchart of the fourth circular algorithm

# 4 SIMULATION OF PROPOSED ALGORITHMS

In order to find parameters that influence applicability of proposed algorithms, a series of simulations are performed. The simulations are not complete – among other things, kinematics of the robot is not considered because it is not important in relation to the localization algorithms. Responses of detectors are simulated only in points of interest, for example a movement between lines is not considered in case of mapping algorithm. System MATLAB has been used to realize simulations.

## 4.1 Simulation of detector response

A model of a source of ionizing radiation may be described by vector $\boldsymbol{\theta}_r = [x_r, y_r, \lambda_r]$ where $x_r$ and $y_r$ are coordinates of the source and $\lambda_r$ is its intensity represented by mean emission of particles (photons in case of gamma radiation). Given $R$ sources, individual models can be joined into a single vector $\boldsymbol{\theta} = [\boldsymbol{\theta}_1, \boldsymbol{\theta}_2, \cdots, \boldsymbol{\theta}_r]^{\mathrm{T}}$. Radioactive decay of a source is a random process that can be described by Poisson distribution [43]. The probability of emission of $x$ particles is given by:

$$p(x = X) = \mathcal{P}(x; \lambda) = \frac{e^{-\lambda}\lambda^x}{x!} \tag{4.1}$$

Making a simplifying assumption that conversion efficiency of detectors is 100 %, the number of emitted particles correspond to measured total count.

Another source of particles that has to be considered is natural radiation background. Since the background comes not only from natural radionuclides but also from cosmic radiation and other sources, it is not feasible to model it precisely. It has been empirically discovered that contribution of radiation background in the area where all experiments took place ranges between 100 and 160 counts per second. For modeling, a continuous uniform distribution has been used. This distribution is used by function `rand` in MATLAB. Total count detected by a detector $k$ can be obtained from equation [6]:

$$\lambda_k(\boldsymbol{\theta}) = \lambda_B + \sum_{r=1}^{R} c_k(\boldsymbol{\theta}_r) \tag{4.2}$$

where $\lambda_B \leftarrow \mathcal{U}([100, 160])$ is the contribution by background, and $c_k(\boldsymbol{\theta}_r)$ is a count rate due to source $r$. Its theoretical value is given by integral [6]:

$$c_k(\boldsymbol{\theta}_r) = a_r \int_0^T \frac{\mathrm{d}t}{||\boldsymbol{x}_k - \boldsymbol{x}_r + \dot{\boldsymbol{x}}_k t||^2} \tag{4.3}$$

where $a_r \leftarrow \mathcal{P}(\lambda_r)$, $T$ is sampling period, $\boldsymbol{x}_k$ is position of detector $k$, $\boldsymbol{x}_r$ is position of source $r$, and $\dot{\boldsymbol{x}}_{\boldsymbol{k}}$ is velocity of detector $k$. Since the $\lambda$ values are typically in order

of thousands and the Poisson distribution is numerically stable for order of tens at most, it is necessary to use approximation by Normal distribution [44]. Therefore $a_r \leftarrow \mathcal{N}(\lambda_r, \lambda_r)$. The integral may be solved analytically but it provides a model which is too much precise. Sufficient approximation is provided by formula:

$$c_k(\boldsymbol{\theta}_r) = \frac{a_r}{||\boldsymbol{x}_k(t+T) - \boldsymbol{x}_r||^2} \tag{4.4}$$

Another effect that has not been discussed yet is a directional characteristics of the detector. That has been measured and presented in Sec. 3.3. Height of the detector above terrain $h$ should be considered as well. The previous equation therefore has to be updated to:

$$c_k(\boldsymbol{\theta}_r) = \frac{K_k(\phi_{k,r})a_r}{||\boldsymbol{x}_k(t+T) - \boldsymbol{x}_r||^2 + h^2} \tag{4.5}$$

where $K_k(\phi)$ is sensitivity in direction $\phi$, and $\phi_{k,r}$ is an angular coordinate of source $r$ in a coordinate system of detector $k$. That can be calculated as:

$$\phi_{k,r} = \begin{cases} \arctan \frac{y'_r}{x'_r}, & \text{if } x'_r > 0 \\ \arctan \frac{y'_r}{x'_r} + 180°, & \text{otherwise} \end{cases} \tag{4.6}$$

where

$$x'_r = (x_r - x_k)\sin\alpha + (y_r - y_k)\cos\alpha \tag{4.7a}$$

$$y'_r = (y_r - y_k)\sin\alpha - (x_r - x_k)\cos\alpha \tag{4.7b}$$

where $\alpha$ is an azimuth of the robot carrying the detector. Assuming constant velocity between two sampling points, coordinates of detector $\boldsymbol{x}_k = [x_k, y_k]$ in time $(t+T)$ are given by:

$$x_k(t+T) = x_k(t) + ||\dot{\boldsymbol{x}}_k(t)||T\cos(90° - \alpha) \tag{4.8a}$$

$$y_k(t+T) = y_k(t) + ||\dot{\boldsymbol{x}}_k(t)||T\sin(90° - \alpha) \tag{4.8b}$$

## 4.2 Mapping algorithm

Mapping of the area of interest is simulated first. For both simulations and real experiments, a site near Faculty of Electrical Engineering and Communication in Brno has been chosen. An ortophoto of the site with the marked polygonal area is shown in Fig. 4.1. A position of the base station is displayed there as well. The chosen polygon has area of 438 m$^2$.


Fig. 4.1: Ortophoto of the experimental site [45]

A result of simulation using line separation of 1 meter can be seen in Fig. 4.2. Function `scatter` is used to display individual measured data points. Theirs color corresponds to a sum of counts per second measured by both detectors according to color bar displayed in the figure on the right. Logarithmic scale is used because CPS values are spanned over multiple decades. An interpolated map is presented using fuction `contourf` in Fig. 4.3. It is obvious that one strong and two weak sources are present in the polygon. Theirs estimated positions are displayed by using black crosses.

In order to find parameters for estimation of the position, the simulation was repeated fifty times for each value of parameter within defined range. An optimal value for parameter can be selected using conveniently chosen criterion. First, parameter $k$ mentioned in Sec. 3.1.2 was sought. The following criterion is defined to evaluate optimality:

$$J_1 = |n_E - n| \tag{4.9}$$

where $n_E$ is estimated count of sources, and $n$ is the actual count. Dependence of criterion $J_1$ on value of parameter k is shown in Fig. 4.4 (left). The optimal value is 0.996. Second parameter to be found is a radius $r$ within which data points should be interpolated in order to get more precise estimation of the position. Sum of

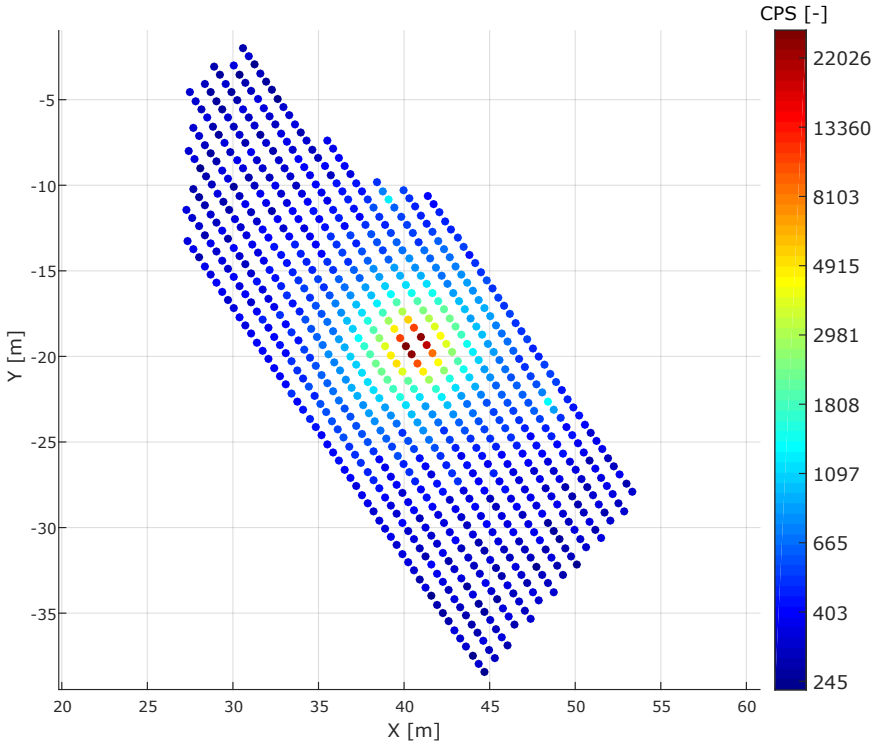


Fig. 4.2: Simulation result of mapping

distances between actual and estimated positions is used as optimality criterion:

$$J_2 = \sum_{r=1}^{R} \sqrt{(x_{E,r} - x_r)^2 + (y_{E,r} - y_r)^2} \tag{4.10}$$

Dependence of criterion $J_2$ on the value of parameter $r$ can be seen in Fig. 4.4 (left). There are two valleys in the dependence. The first one probably corresponds with the weak sources, the other one with the strong source. Value 1.5 is chosen as optimal.

## 4.3 Strong source search algorithm

A possible result of simulation of strong source search algorithm is illustrated in Fig. 4.5. Peaks detected in the individual lines are marked by using red crosses. It can be seen in the figure that no peak has been found in the first line, but the next two lines have corresponding peak. That results in alternation of the original trajectory. Part of final loop is displayed as well, and it shows where it is crossing the perpendicular line leading to the source (black cross).

Parameter $d$ needs to be set. It defines maximal allowed distance of neighboring peaks in which the trajectory is altered. Optimality criterion is defined as a multiple

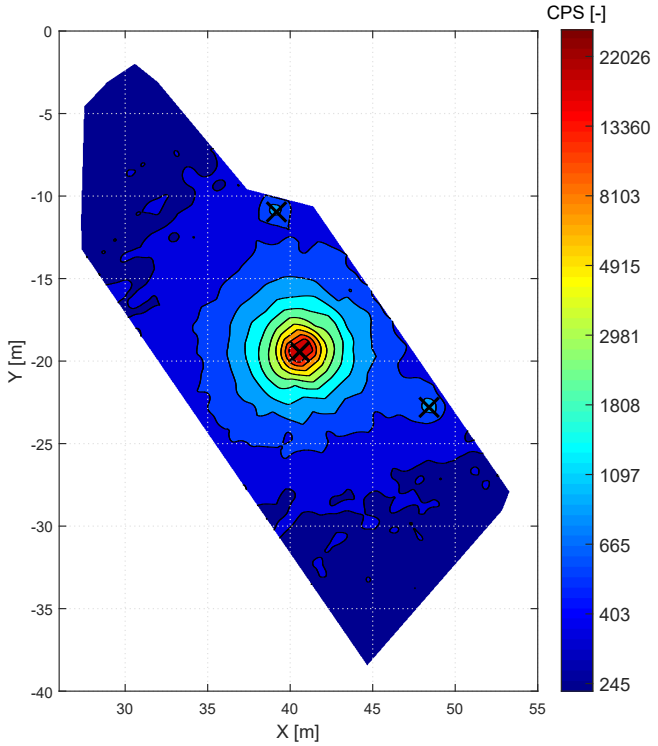


Fig. 4.3: Interpolated map

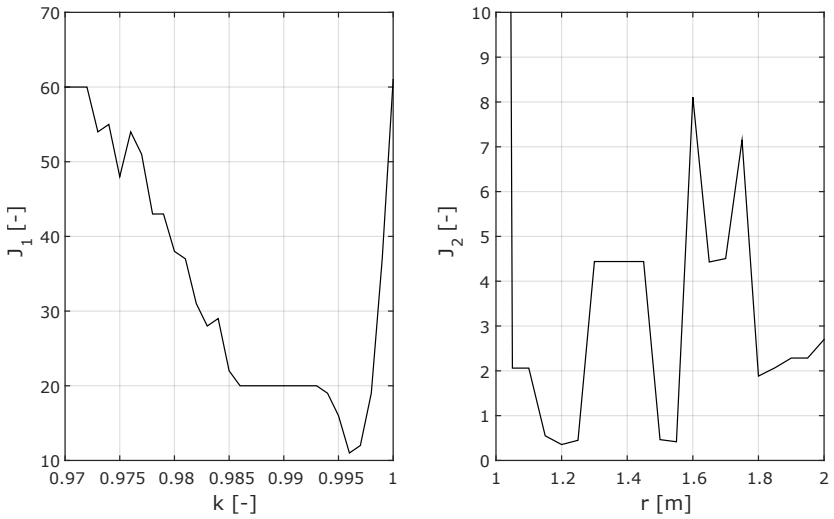


Fig. 4.4: Optimality criteria for mapping parameters

of the number of basic lines $l$ and distance between position of the source and the loop crossing.

$$J_3 = l\sqrt{(x_S - x_L)^2 + (y_S - y_L)^2} \tag{4.11}$$

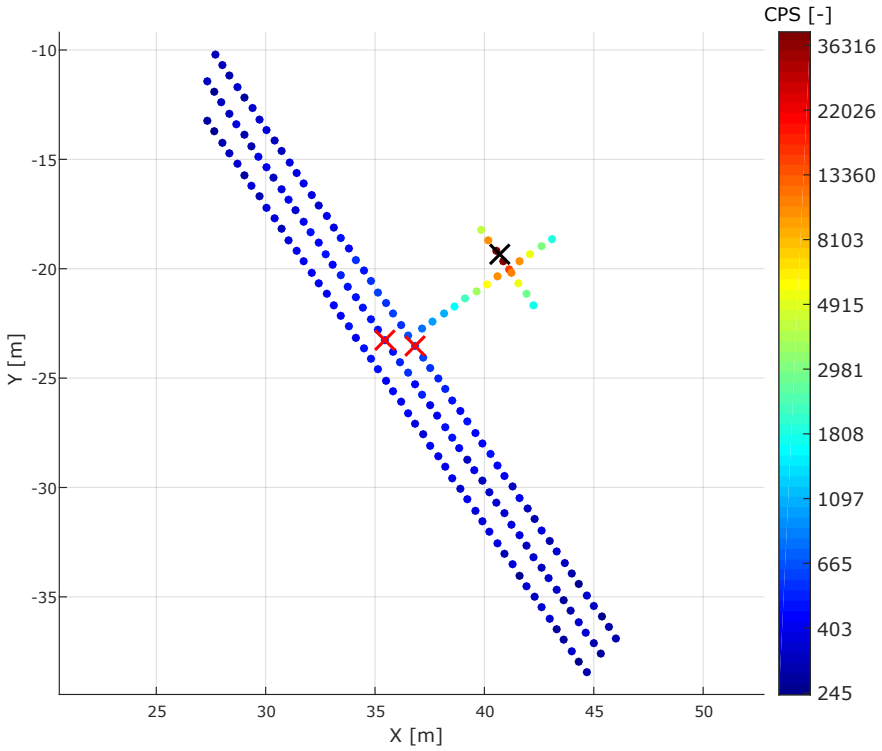


Fig. 4.5: Simulation result of the strong source search

Dependence of criterion $J_3$ on parameter d is shown in Fig. 4.6. The optimal value is ambiguous, eventually 1.4 was chosen.

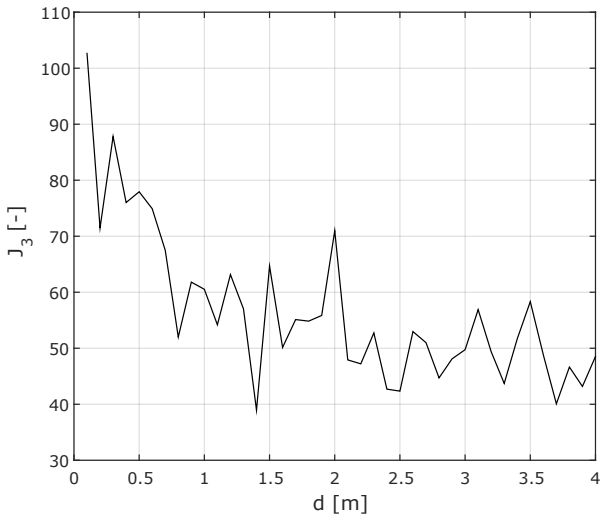


Fig. 4.6: Optimality criterion for a peak distance parameter

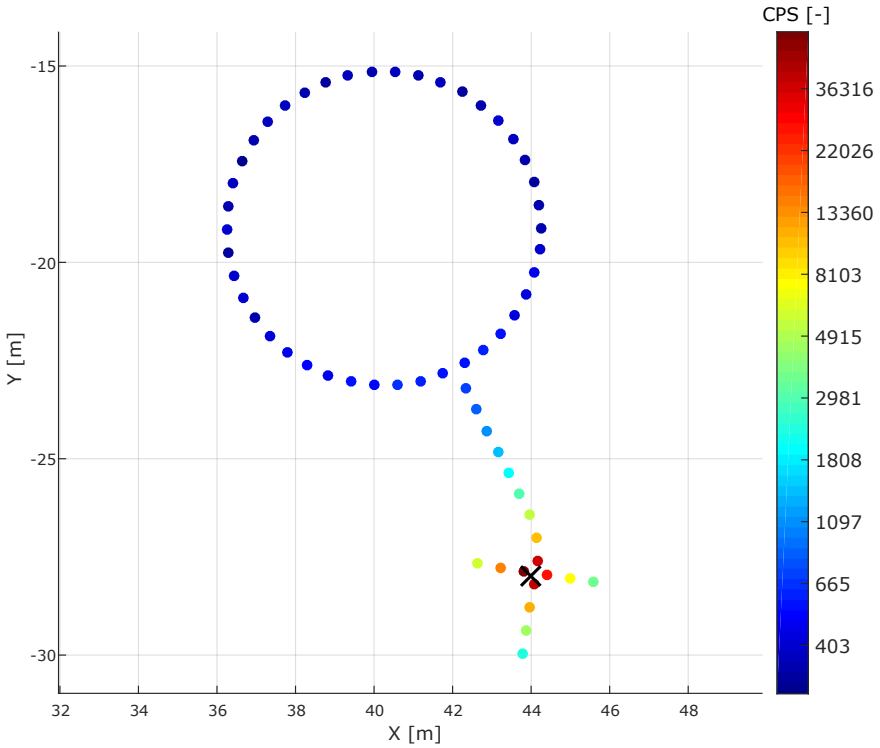


Fig. 4.7: Simulation result of the first circular algorithm

## 4.4 First circular algorithm

A result of the simulation of the first circular algorithm is shown in Fig. 4.7. The circle has radius of 4 meters. After the data along circle are measured, direction of the source may be estimated. Accuracy of estimation depends on a choice of parameter $p$ – shift between interpolated and actual maximum. As optimality criterion a distance of the source and a line passing through circle center and directional point is used.

$$J_4 = \frac{ax_S + by_S + c}{\sqrt{a^2 + b^2}} \tag{4.12}$$

where $[a, b, c]$ are parameters of the line. Dependence of criterion $J_4$ on parameter $p$ can be seen in Fig. 4.8. The optimal value is 0.7. Once the direction is found, algorithm proceeds to navigation to the source. There are two more parameters that need to be set. One of them is coefficient $K$ which determines how much data from both detectors must differ in order to enable an update of the direction. The second parameter $\Delta\phi$ determines how much the direction is altered. Both parameters have common optimality criterion – distance of loop crossing and the

actual source position.

$$J_5 = J_6 = \sqrt{(x_S - x_L)^2 + (y_S - y_L)^2} \tag{4.13}$$

Dependence of criteria $J_5$ and $J_6$ on respective parameters is shown in Fig. 4.9. The optimal value of $K$ is 1.04, optimal value of $\Delta\phi$ is approximately 18°.

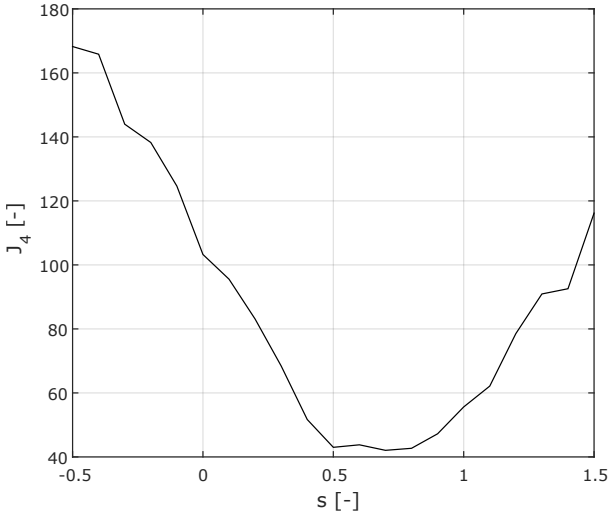


Fig. 4.8: Optimality criterion for a peak shift parameter

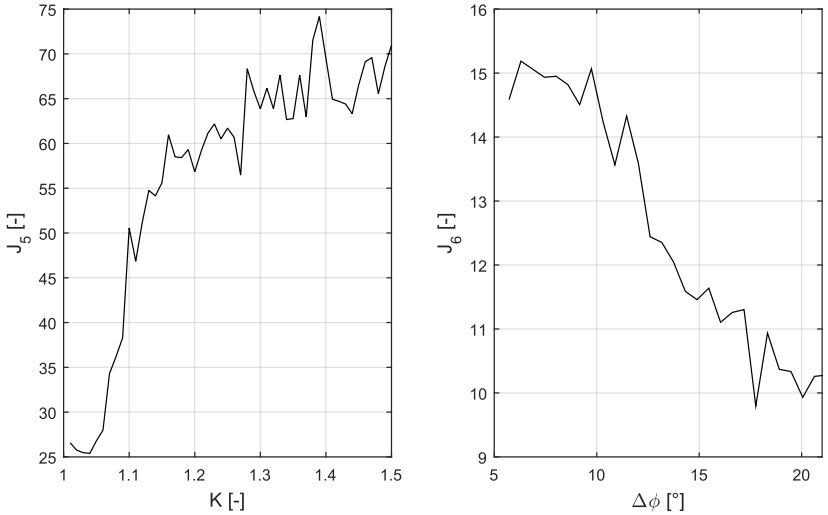


Fig. 4.9: Optimality criteria for navigation to source parameters

## 4.5 Second circular algorithm

A difference between this and previous algorithms is only in number of sources detectable from the circle. Data simulated along a circle compose a signal shown in Fig. 4.10 (left). Since the signal is very noisy it may not be apparent that two prominent peaks should be there. Relative peak prominence $p$ which helps to filter those peaks corresponding only to the sources needs to be found. Optimality criterion is simple – a difference between the expected and detected number of peaks $n_D$.

$$J_7 = |n_D - n| \tag{4.14}$$

Dependence of criterion $J_7$ on peak prominence $p$ can be seen in Fig. 4.10 (right). The optimal value is 0.8. A complete result of simulation of this algorithms is then shown in Fig. 4.11. Both sources have been localized successfully.

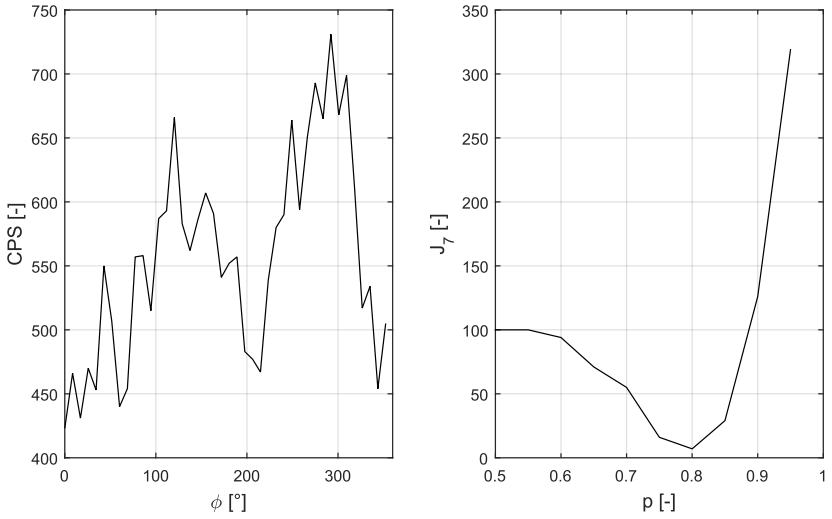


Fig. 4.10: Finding peaks on a circle

## 4.6 Third circular algorithm

This time, the whole area of polygon has to be covered using multiple circles. A possible solution is illustrated in Fig. 4.12. It is assumed that the sources are detectable 4 meters away from circles. Circle $c_1$ has radius of 3.5 m, other two circles have radius of 4 m. Therefore, the inner area of all circles is covered. Covering of outer areas is sketched using dashed circles. Some small regions are outside the detectable area, but in real conditions the range has not sharp borders. Sources within these peripheral regions would be probably detected as well.

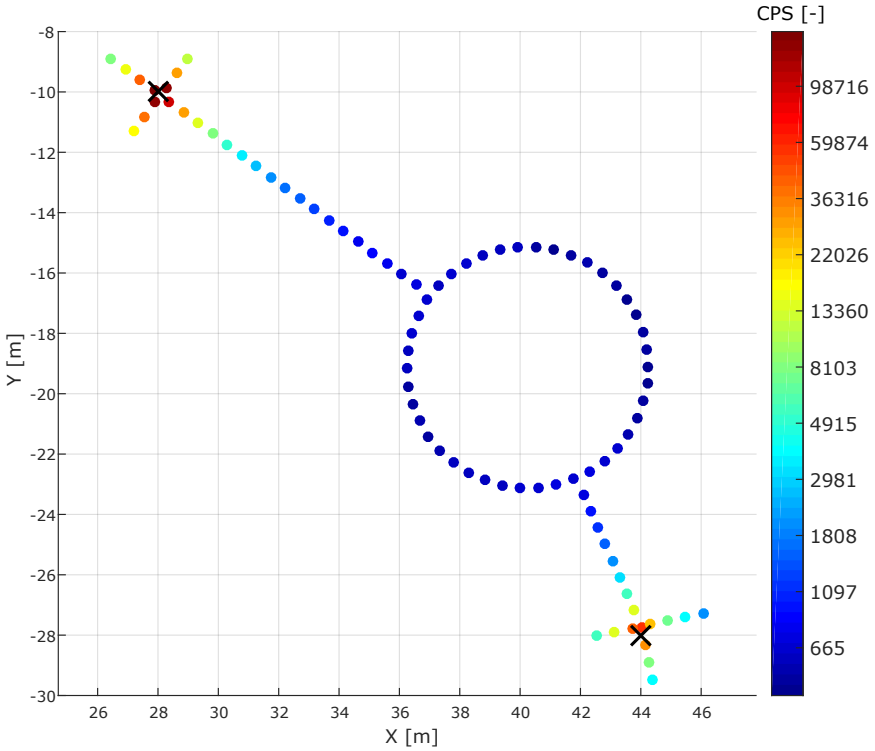


Fig. 4.11: Simulation result of the second circular algorithm

A result of simulation is shown in Fig. 4.13. It is worth noticing that one source lies very close to circle $c_3$, and for that reason the final loop is omitted – the circle provides additional data for interpolation.

## 4.7 Fourth circular algorithm

The polygon may be completely covered by using a higher number of smaller circles. A possible solution is illustrated in Fig. 4.14. As in the previous section, it is assumed that sources can be detected within 4 meter radius. Three larger circles have radius of 3 m, the others have radius of 2 m .

First, only circle data are simulated in order to test algorithm for filtering intersections of directional rays. A result of this simulation with marked rays is shown in Fig. 4.15. There are two intersections inside circle $c_5$. The intersection that is nearer to the source is accepted, the other one is discarded according to presented rules. Three intersections that are near to the source in the middle of the figure are united into a single point. Choice of respective parameter $D_{min}$ is not critical here because all sources are well spatially separated. Its value may be set for example to 1.5 m. The last visible intersection is caused by false positive detection of the

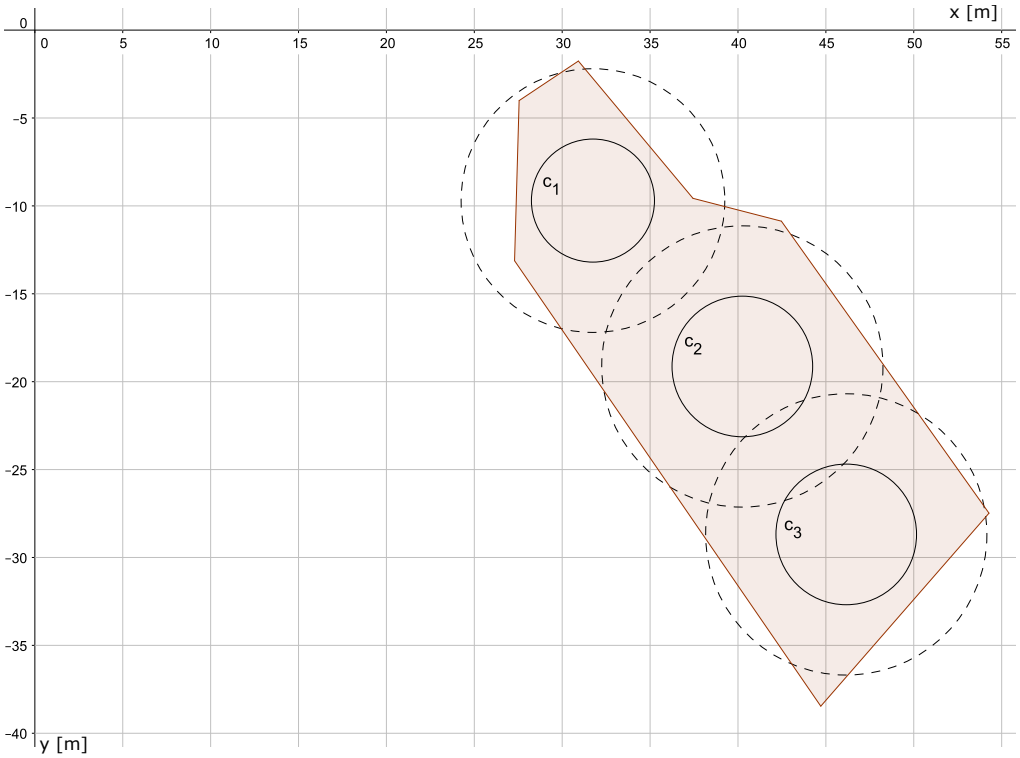


Fig. 4.12: Layout of circles for the third circular algorithm

peak on circle $c_2$. Because the corresponding intersection is discarded, the ray would be classified as a potential source with known direction and the robot would have tried to find it inside circle $c_2$. The last source have only one matching ray, and is therefore also classified as a potential source with a known direction.

A complete result of simulation can be seen in Fig. 4.16. The black crosses represent the actual position of the sources, the red crosses and the red ray represent estimations. In order to maintain the figure well arranged, search of detected non-existing potential source is not displayed – it would have added more data points inside respective circle. The upper left potential source is being approached from the circle, the other two sources are being approached from a point where localization of a previous source have ended. Only a part of data points is visualized – those in which update of direction is allowed.

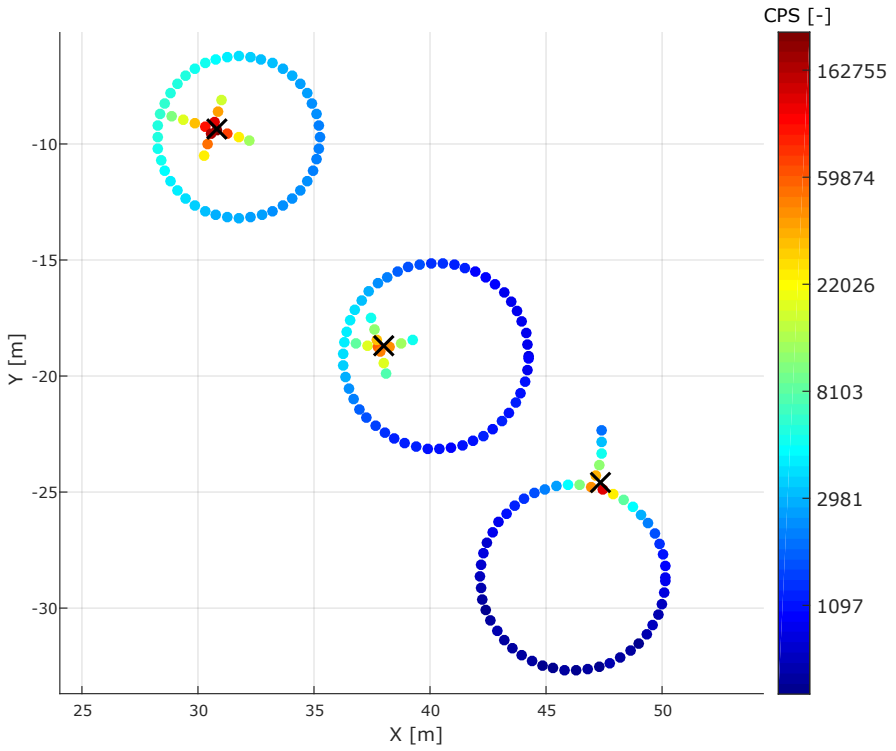


Fig. 4.13: Simulation result of the third circular algorithm

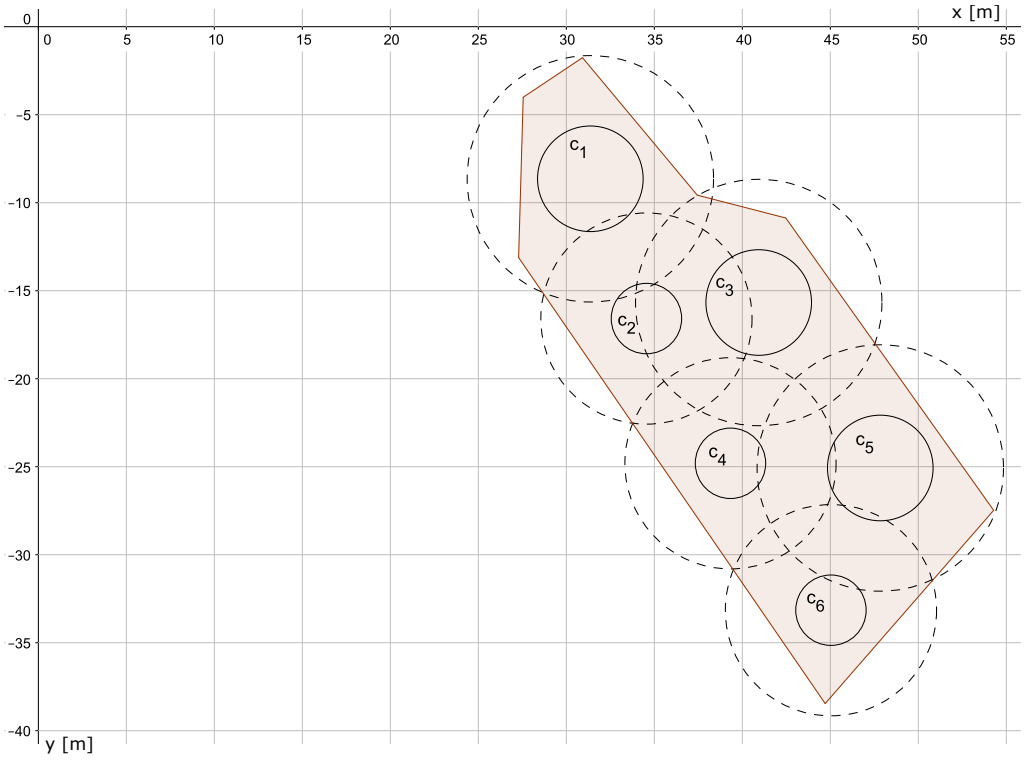


Fig. 4.14: Layout of circles for the fourth circular algorithm

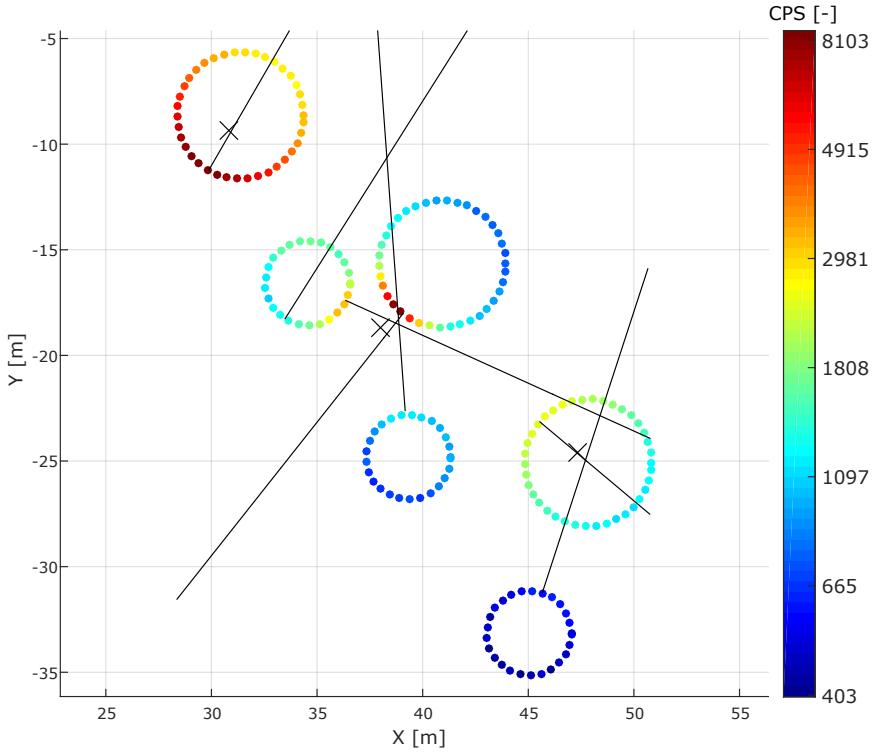


Fig. 4.15: Simulation of direction rays

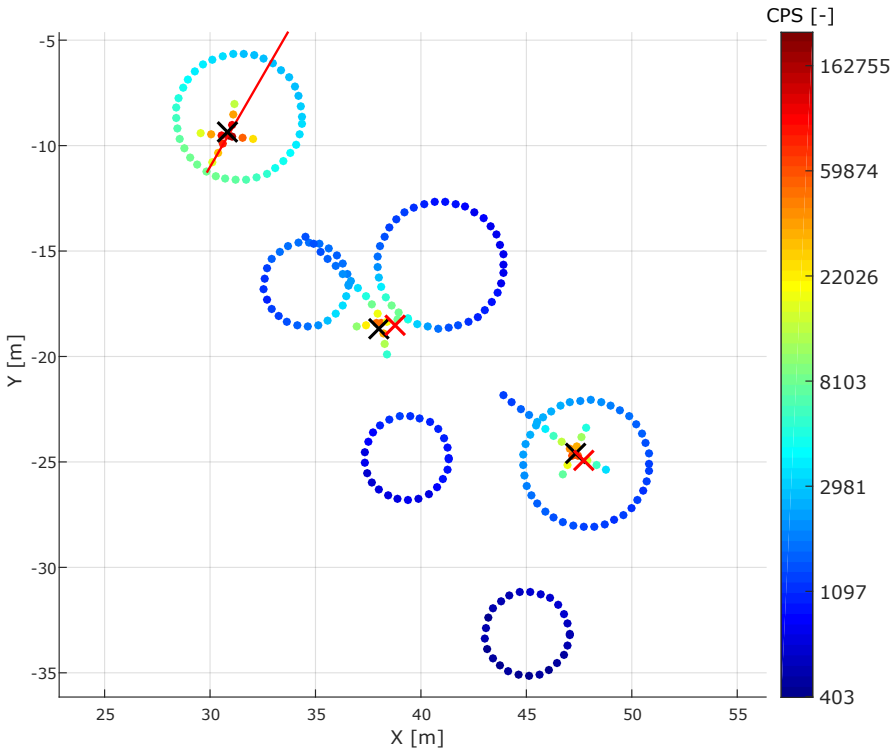


Fig. 4.16: Simulation result of the fourth circular algorithm

# 5 EVALUATION OF RESULTS

All algorithms were tested by using real radiological sources. In the first part of this chapter, the most successful results are presented. They are compared to simulations previously introduced in this thesis. In the second part of this chapter, results of different algorithms are compared to each other. The experiments were realized with reconnaissance robot Orpheus-X3 introduced in Sec. 2.1.

Stated activities of all sources are valid to date when the corresponding experiment was performed. The activity is given by a calibration value to a specified date and a radioactive decay. An example of a calibration protocol for one of the used sources can be found in the Appendix B. Activity $A$ in time $t$ is defined by formula [46]:

$$A = A_0 e^{-\frac{t}{T_{1/2}\ln(2)}} \qquad [\mathrm{Bq}; \mathrm{Bq}, \mathrm{y}, \mathrm{y}] \tag{5.1}$$

where $A_0$ is activity in time $t = 0$, and $T_{1/2}$ is a half-life of given radionuclide. The half-life and time may be expressed by arbitrary time unit but both by the same. Half-life of the used radionuclide is: 30.021 years for $^{137}$Cs and 5.275 years for $^{60}$Co [47]. For example, used $^{60}$Co source had activity 100 MBq to 5th December 2013. The first experiment has been performed 2nd March 2017. Activity to this date is therefore:

$$A = 100 e^{-\frac{3.241}{5.275\ln(2)}}\ \mathrm{MBq} = 41.2\ \mathrm{MBq} \tag{5.2}$$

Activities of other sources to other dates may be calculated analogically.

## 5.1 Experimental results

Setup of mapping experiment can be seen in Tab. 5.1. It is very similar to the setup of simulation in order to provide better comparison. An unprocessed result of mapping is shown in Fig. 5.1. It might be rather difficult to realize that three sources are present in the polygon, because the weak sources are effaced by the strong one. However, after the interpolation is performed, individual sources can be easily identified. Autonomous localization is performed as well using parameters gained in simulation. The interpolated map with marked computed positions of sources is shown in Fig. 5.2. The parameters were well-chosen, an error of computed position is of the order of centimeters.

Two different setups were used for testing the strong source search algorithm. Their overview is in Tab. 5.2. The result of the experiment with the second setup is shown in Fig. 5.3. The actual position of the source is marked by a black cross.

Tab. 5.1: Setup of the mapping experiment

| | $S_1$ | $S_2$ | $S_3$ |
|---|---|---|---|
| Radionuclide | $^{60}$Co | $^{137}$Cs | $^{60}$Co |
| Activity | 8.0 MBq | 220 kBq | 350 kBq |
| Position (relative to BS) [m] | $[40.6, -19.3]$ | $[39.1, -10.7]$ | $[48.5, -22.8]$ |

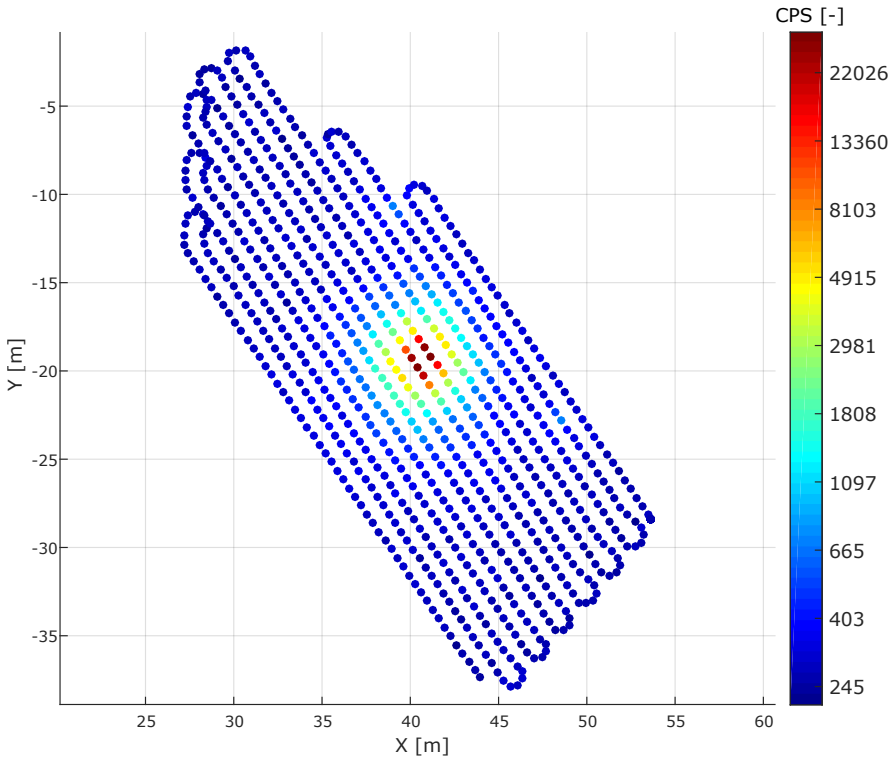


Fig. 5.1: Experimental result of mapping

Data from the first two lines were sufficient to estimate direction of source with enough precision. An error of computed position is also of the order of centimeters. It is important to use the final loop. In case of the first setup, initial estimation of direction was less precise but thanks to looping, position could be determined well.

Setups of experiments with first and second circular algorithms are in Tab. 5.3. For both experiments a common circle was used – its parameters are the same as parameters of circle $c_2$ in Tab. 5.4. The experimental result of the first circular algorithm is shown in Fig. 5.4. The robot approached the circle along tangent as planned and then went round the whole circle. It has been discovered that the choice of value of parameter $p$ (peak shift) according to simulation is not correct. In real situation, the peak shift is better characterized by $p = -0.2$. After a correction

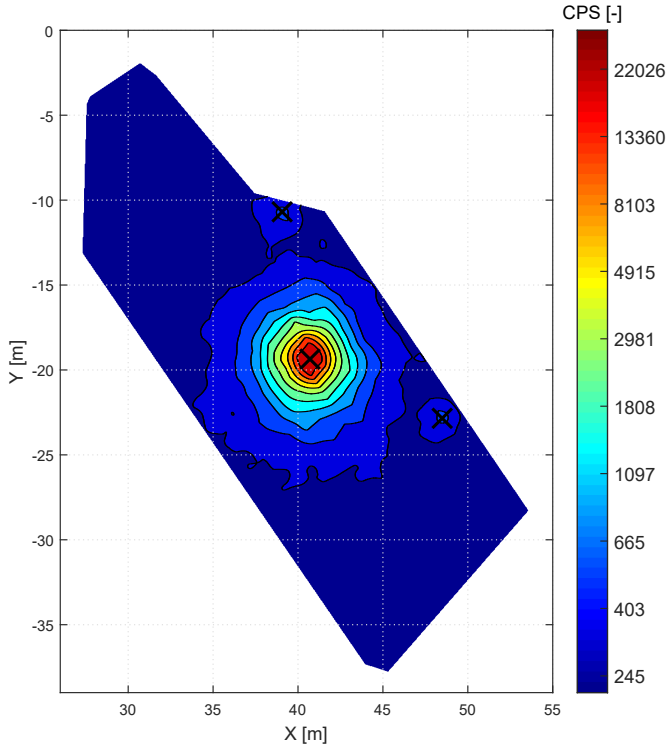


Fig. 5.2: Interpolated radiation map

of the parameter, the experiment could be repeated. Thanks to proximity of the source to the circle and its intensity, the initial estimation of direction was precise enough and there was almost no need to update direction during approach to the source.

The experimental result of the second circular algorithm can be seen in Fig. 5.5. Localization of the source $S_1$ was not a problem, the result is very similar to the previous experiment. Regarding the other source, due to its higher distance to the circle, initial estimation of a direction was very inaccurate – approximately 15° error. During the first attempt the control algorithm was not able to navigate the robot to the source correctly due to a problem in updating the direction. It was necessary to alter values of respective parameters $K$ and $\Delta\phi$ in order to manage smoother change of direction. New values of parameters are: $K = 1.1, \Delta\phi = 9°$. After that change, the source $S_2$ was successfully located as well.

A setup for the third circular algorithm is divided into Tab. 5.4 and Tab. 5.5. The experimental result is shown in Fig. 5.6. The robot explores sequentially circles $c_3$, $c_2$ and $c_1$, and for each source the direction is estimated. Then the source $S_1$ is approached along directional line and is closer explored by using the loop. Source $S_2$ is explored in the same way. Source $S_3$ is passed, and its position is evaluated

Tab. 5.2: Setup of the strong source seach experiment

| | Setup 1 | Setup 2 |
|---|---|---|
| Radionuclide | $^{60}$Co | $^{137}$Cs |
| Activity | 8.0 MBq | 65.6 MBq |
| Position (relative to BS) [m] | $[38.0, -18.7]$ | $[40.6, -19.3]$ |
| Distance to base line [m] | 5.7 | 7.5 |

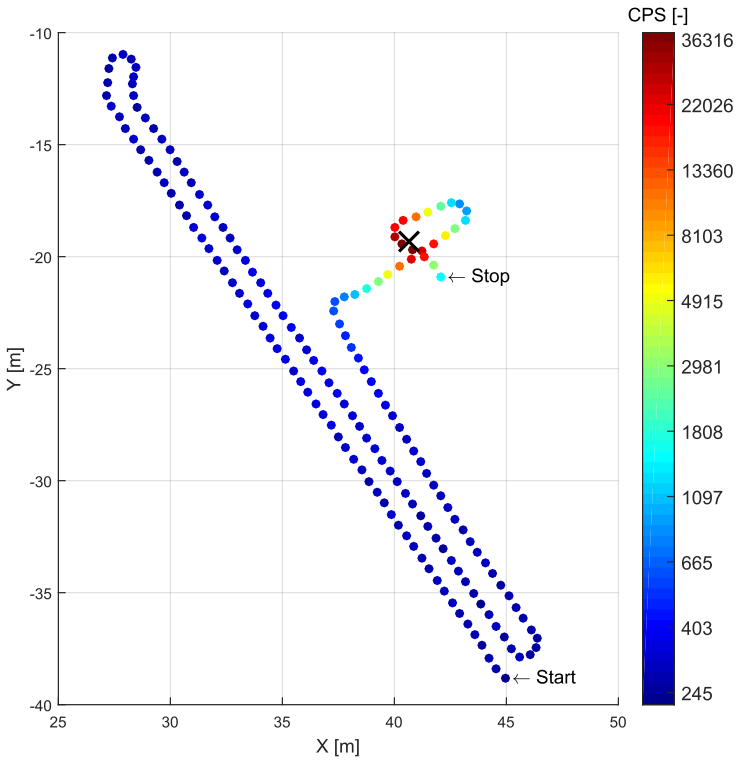


Fig. 5.3: Experimental result of the strong source search

within half a meter distance from the circle, therefore the loop may be skipped and the experiment is completed.

A setup for the fourth circular algorithm is divided into Tab.5.6 where six circles are defined, and Tab. 5.5 including description of the sources. All the circles are explored first, and then intersections of directional rays are evaluated. First experimental result is shown in Fig. 5.7. Estimations $E_2$ and $E_3$ are quire precise, but the error of estimation $E_1$ is approximately 2 meters. It is caused by wrong estimation of direction from data on circle $c_2$, probably due to their shift caused by a nearer source $S_2$. The sources were not localized precisely because the experiment was interrupted by software malfunction.

Tab. 5.3: Setup of the first and second circular algorithm experiment

| | 1st circ. alg. | 2nd circ. alg. | |
|---|---|---|---|
| | | $S_1$ | $S_2$ |
| Radionuclide | $^{60}$Co | $^{60}$Co | $^{60}$Co |
| Activity | 40.1 MBq | 7.8 MBq | 40.0 MBq |
| Position (relative to BS) [m] | [47.4, −24.6] | [47.4, −24.6] | [38.0, −18.7] |
| Position (relative to circle) | Outside | Outside | Outside |
| Distance to circle [m] | 6.0 | 6.0 | 10.6 |

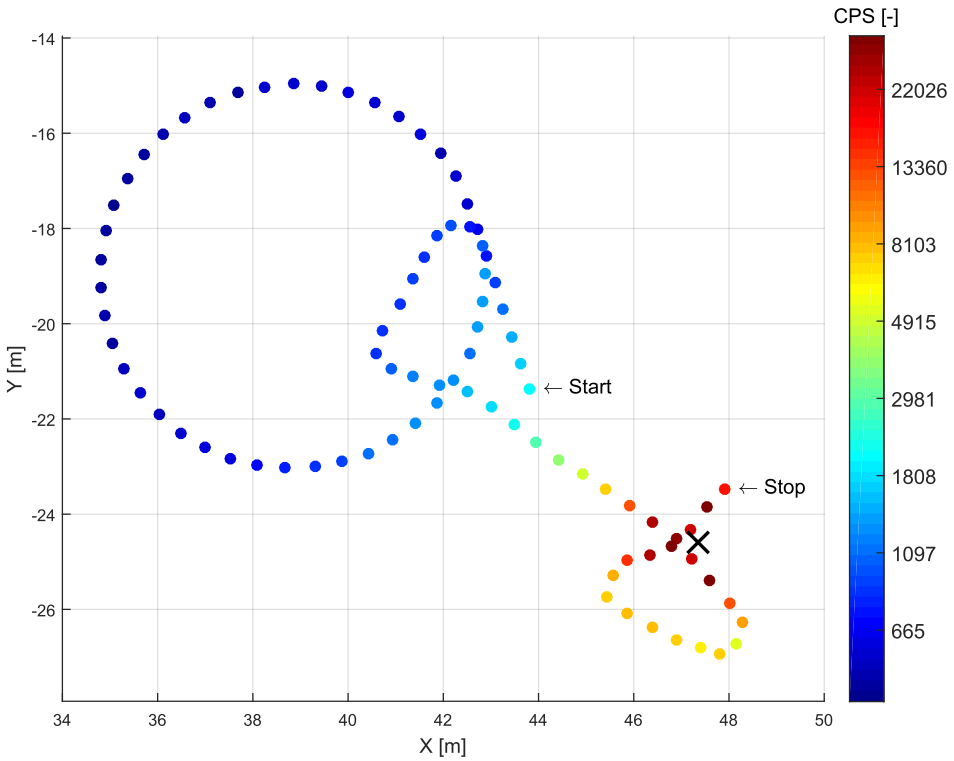


Fig. 5.4: Experimental result of the first circular algorithm

The second experimental result is shown in Fig. 5.8. In order to keep the figure well-arranged, only the last circle is displayed followed by approach to detected sources. One false positive detection of a non-existing fourth source marked as $E_4$ can be seen in the figure. Looping around sources has been disabled by configuration in this experiment. The purpose is to test if sources can be localized precisely enough purely by updating direction. The result shows that in case of the source $S_3$ it would be better to do a loop. Since the false estimation $E_4$ lies between two true sources, the algorithm is actually not much affected by it. The source $S_1$ was not found due

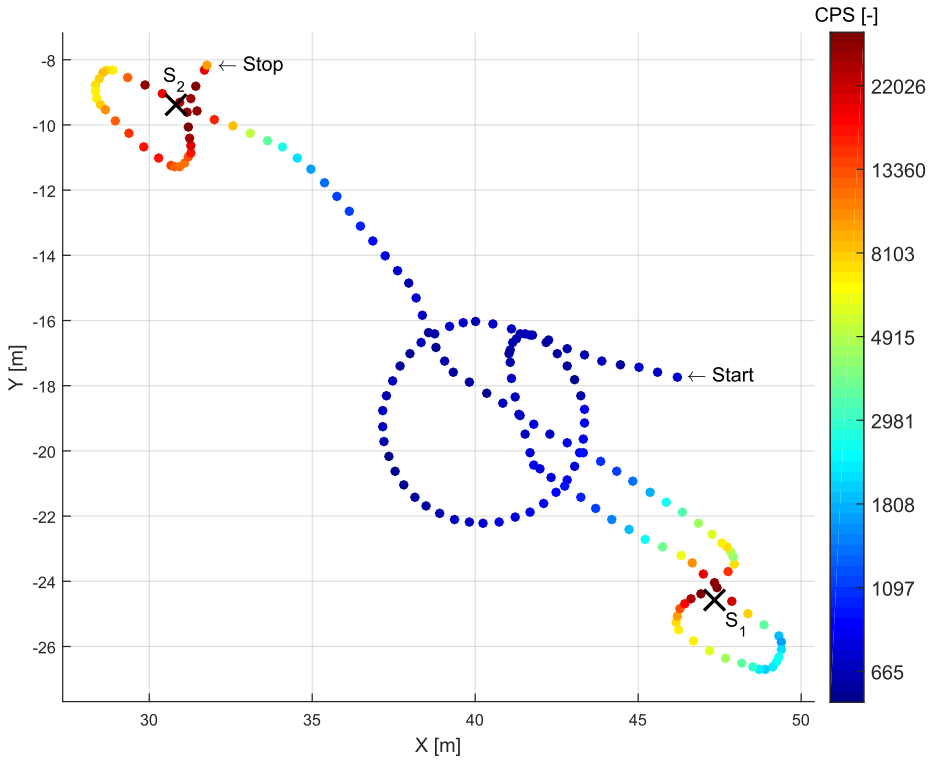


Fig. 5.5: Experimental result of the second circular algorithm

Tab. 5.4: Setup of circles for the third circular algorithm experiment

| | $c_1$ | $c_2$ | $c_3$ |
|---|---|---|---|
| Position of center (relative to BS) [m] | $[31.7, -9.7]$ | $[40.3, -19.1]$ | $[46.2, -28.7]$ |
| Radius [m] | 3.5 | 4.0 | 4.0 |

to poor initial estimation and low value of parameter $\Delta\phi$. There was not enough space to alter direction sufficiently.

Tab. 5.5: Setup of soruces for the third circular algorithm experiment

| | $S_1$ | $S_2$ | $S_3$ |
|---|---|---|---|
| Radionuclide | $^{60}$Co | $^{137}$Cs | $^{60}$Co |
| Activity | 40.0 MBq | 65.3 MBq | 7.8 MBq |
| Position (relative to BS) [m] | $[30.8, -9.4]$ | $[38.0, -18.7]$ | $[47.4, -24.6]$ |
| Nearest circle | $c_1$ | $c_2$ | $c_3$ |
| Position (relative to the nearest circle) | Inside | Inside | Outside |
| Distance to the nearest circle [m] | 2.5 | 1.7 | 0.3 |

Tab. 5.6: Setup of circles for the fourth circular algorithm experiment

| | $c_1$ | $c_2$ | $c_3$ |
|---|---|---|---|
| Position of center (relative to BS) [m] | $[31.4, -8.6]$ | $[34.6, -16.6]$ | $[40.9, -15.7]$ |
| Radius [m] | 3 | 2 | 3 |
| | $c_4$ | $c_5$ | $c_6$ |
| Position of center (relative to BS) [m] | $[39.3, -24.8]$ | $[47.8, -25.1]$ | $[45.0, -33.2]$ |
| Radius [m] | 2 | 3 | 2 |

Tab. 5.7: Setup of soruces for the fourth circular algorithm experiment

| | $S_1$ | $S_2$ | $S_3$ |
|---|---|---|---|
| Radionuclide | $^{60}$Co | $^{137}$Cs | $^{60}$Co |
| Activity | 39.3 MBq | 65.1 MBq | 7.7 MBq |
| Position (relative to BS) [m] | $[30.8, -9.4]$ | $[38.0, -18.7]$ | $[47.4, -24.6]$ |
| Nearest circle | $c_1$ | $c_3$ | $c_5$ |
| Position (relative to the nearest circle) | Inside | Outside | Inside |
| Distance to the nearest circle [m] | 2.0 | 1.2 | 2.4 |

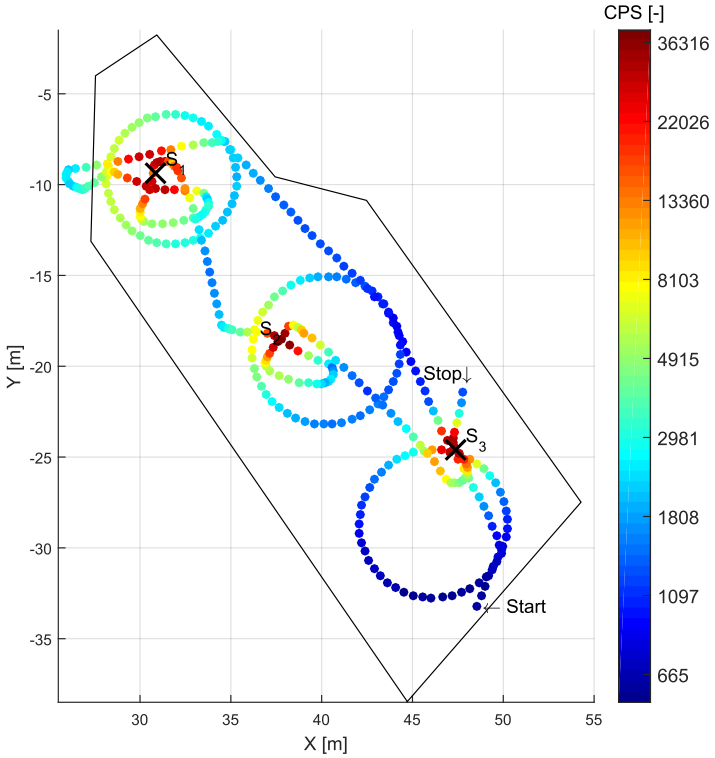


Fig. 5.6: Experimental result of the third circular algorithm

## 5.2 Comparison of the algorithms

The algorithms are mutually compared regarding time efficiency and precision of localization in Tab. 5.8. Beside the total time, average time needed for localizing one source is computed, and also how much time is needed to get initial estimation of the direction or location (it is equal to the time before the first update of trajectory). The localization error is a simple distance between a reference position and interpolated position. In case of algorithms where more sources are localized, a mean value is used.

In case of mapping, only total time is mentioned because the trajectory is not updated during the experiment, and therefore the needed time does not depend on a number of sources. In both experiments with strong source search algorithm, two lines were passed before the trajectory could be updated, and it took almost two minutes. Total time does not differ much – time needed for the final loop is almost constant, therefore the time depends mostly on length of the perpendicular line (assuming the same number of lines). Localization error was as good as in the mapping experiment in one case and worse by an order in the other case. It implies strong dependency of the error on accuracy of the initial estimation of the direction.

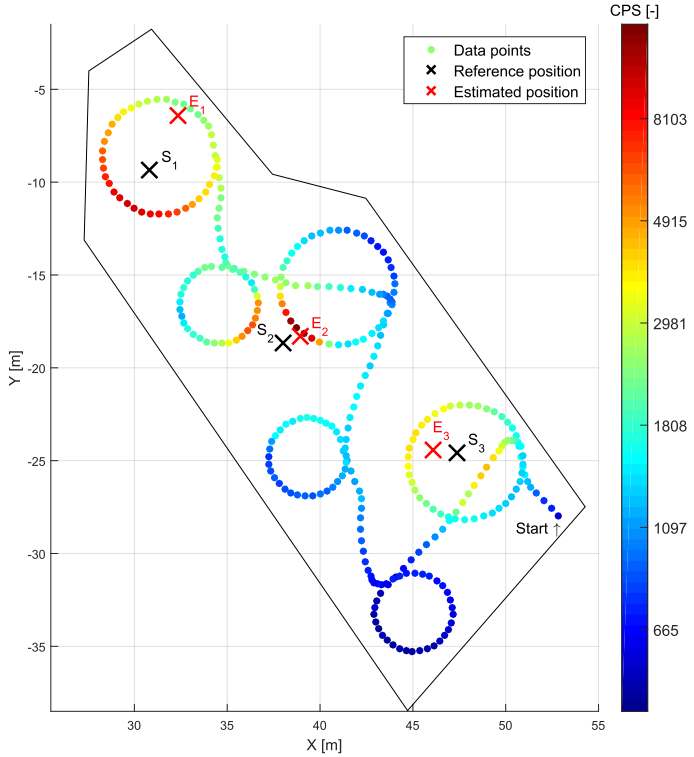


Fig. 5.7: Experimental result of the fourth circular algorithm I

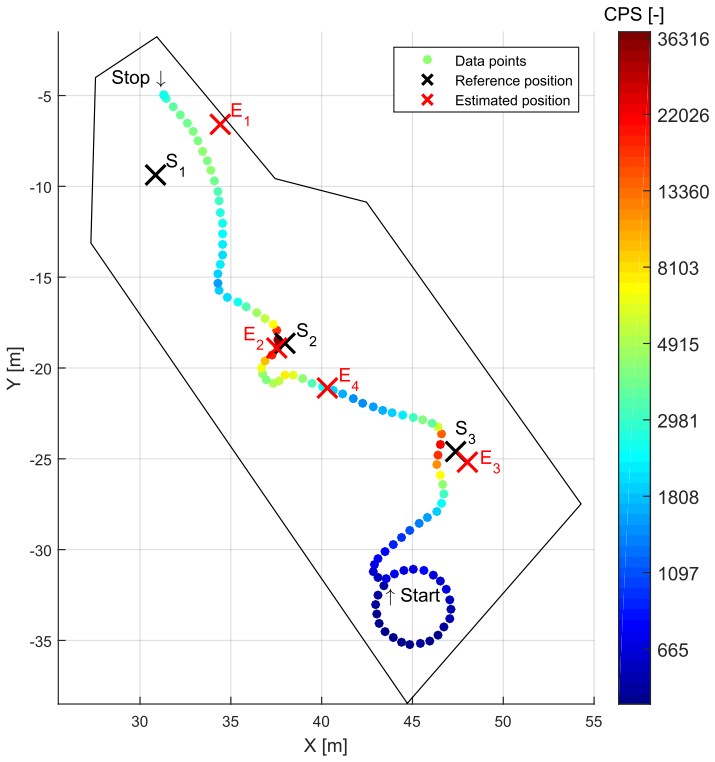


Fig. 5.8: Experimental result of the fourth circular algorithm II

The first and the second circular algorithms provide a very similar result. They need virtually the same time per source, and the localization error is in same order. The third circular algorithm is approximately by 40 % slower with similar localization error, but it covers the whole area of interest. Such increase of the needed time is a reasonable price for the coverage. The fourth circular algorithm requires more time to perform a basic exploration. Although the sum of circles' circumference is lower than in case of the third algorithm, time costs bonded with movement between the individual circles are higher. The localization error is not evaluated because no fully successful experiment has been realized yet.

Usage of the direction-sensitive detection systems seems promising in terms of localization of the lost radiation sources. All proposed algorithms that use dynamic update of trajectory provide better time efficiency than simple mapping. In comparison to the strong source search algorithm (which does not work with directional sensitivity), the circular algorithms based on estimation of direction have stable results for different type and number of sources. The circular algorithm based on estimation of location should provide the best time efficiency for higher numbers of sources, because it has the highest initial time costs which would pay back in situations where the previous algorithms probably fail due to their design. For example, if there was a source detectable from two circles in case of the third circular algorithm. However, it is currently a rather theoretical assumption than a proved fact. The algorithm has to be improved and more experiments need to be realized.

Tab. 5.8: Comparison of the algorithms

| | Total time [mm:ss] | Time per source [mm:ss] | Time to first trajectory update [mm:ss] | Localization error [m] |
|---|---|---|---|---|
| Mapping | 15:03 | – | – | 0.06 |
| Source search I | 2:47 | 2:47 | 1:54 | 0.94 |
| Source search II | 2:53 | 2:53 | 1:54 | 0.04 |
| 1st circ. alg. | 1:28 | 1:28 | 0:48 | 0.52 |
| 2nd circ. alg. | 2:54 | 1:27 | 0:48 | 0.40 |
| 3rd circ. alg. | 6:06 | 2:02 | 3:17 | 0.36 |
| 4th circ. alg. | 5:21 | 1:47 | 4:04 | – |

# CONCLUSION

In the first chapter, I have compiled a description of basic principles of radiation detection. I focused primarily on scintillation detectors, because their parameters best fit to the desired ones. Scintillators typically have both higher density and higher volume than other types of detectors, therefore their probability of interaction with gamma radiation is higher than in case of gas-filled detectors or semiconductor detectors. The sensitivity of the detector is crucial due to relatively large assumed distance from the sources of gamma radiation until they are found. A possible way to realize direction-sensitive system is discussed in the thesis.

The next chapter focuses on development of a complex system that can be used for testing localization algorithms. The system is based on reconnaissance robot Orpheus-X3 developed by Group of Robotics and AI at the Faculty of Electrical Engineering and Communication, Brno University of Technology. The robot may be equipped with RTK-GNSS receiver that provides precise self-localization. A module developed by Ing. Tomáš Jílek, Ph.D. is used for navigation and may be controlled externally by setting sequence of waypoints. A pair of scintillation detectors is used for measurement of the gamma radiation. I have created a library for communication with multichannel analyzers connected to the detectors. The sensory equipment is attached to the robot by custom mounting that I designed and made, using a 3D printer. Then I have developed software that periodically receives data from GNSS receiver and provides time synchronization for the multichannel analyzers. It also enables tracking the robot's motion along planned trajectory and invoke its update in defined moments. For setting the control software, I proposed a structure of a configuration file and implemented a parser for it.

I took an existing algorithm for mapping a distribution of a radiation field which was applicable in rectangular areas, and extended it to a more general polygonal area. It is based on a trajectory composed of parallel lines. I have designed a method for autonomous localization of radiological sources in the resulting radiation map. It is composed of custom detector of two-dimensional local maxima and interpolation function. The mapping is a time consuming process, therefore I suggested an alternative algorithm that evaluates measured data in real time, and enables altering of the trajectory in order to get near the source faster. It is applicable in a situation where more than one strong source is present in the area of interest. When there is no strong source, the result of the algorithm is the same as in case of mapping.

The chosen geometry of the system provides directional sensitivity which I quantified experimentally. I have improved the directional characteristics by placing a lead shielding between detectors. That gave me access to development of more intelligent localization algorithms. I suggested a circle as a basic geometric primitive

for initial exploration because it is more suitable for estimation of a direction in which the source can be found, than a line used in the previous algorithms. I developed them incrementally, beginning with the easiest case and ending with the most sophisticated solution. I proposed a method that allows estimating the direction of multiple sources from data collected on a circle. Once the direction is known, the robot may follow it. Under those conditions I suggested, the direction is continuously updated in order to localize the source as precisely as possible. The first three circular algorithms are based purely on estimation of the direction. The last one fuses directional information from multiple circles in order to get estimation of location of the sources. The directional information is described by rays which intersect in some points. I have designed a filter that lets pass only intersections that could correspond with a source.

I have developed a simulation suite for MATLAB that allowed me to test algorithms in the laboratory first. It helped me to find optimal values of several parameters which affect the behavior of the proposed algorithms. In simulation, all the algorithms worked as expected.

It is not feasible to include effects such as background contribution, motion and response of detectors, or kinematics of the robot into simulations all at once. Therefore, the algorithms need to be tested in real conditions with actual radiological sources as well. I implemented and integrated them all in the previously mentioned software creating an extensive control module. Then I tested them sequentially. Some of the assumptions based on simulations were disproved and both the program and parameters had to be altered to some extent. Eventually, all the algorithms provided satisfactory results except the last one – I have accomplished only a partial success with it. In the last section, I compared my algorithms regarding time efficiency and precision of localization. It is not possible to choose a single algorithm as the best one, since each provides better results in different situations.

I plan to continue in this research within my PhD studies. This area of research provides extensive area for further development. The proposed algorithms may exceed the state-of-the-art ones to some extent but there is still a lot work to do.

First, it is necessary to finish the last circular algorithm which covers the most cases but it has not been successfully tested yet. If proved efficient, it would signify that the circular algorithms are perspective. The next step would be a development of an algorithm that generates parameters of the circles optimally, given the definition of polygon and range of the detectors. Different types of detectors and geometries of a detector system should be tried and compared to the current solution. Even the mapping algorithm may be improved to be applicable in all types of polygons, even the ones with holes. At this point, only the point sources are assumed. It would be challenging to focus also on localization of line and area sources.

# BIBLIOGRAPHY


[1] *Chemical, Biological, Radiological, and Nuclear Response* [online]. Joint Publication 3-41. Joint Chiefs of Staff, 2016 [cit. 2017-05-13]. Link: `http://www.dtic.mil/doctrine/new_pubs/jp3_41.pdf`

[2] Radiological Dispersal Device Playbook. *Public Health Emergancy* [online]. Washing-ton, DC: U. S. Department of Health and Human Services, 2015 [cit. 2017-03-12]. Link: `https://www.phe.gov/preparedness/planning/playbooks/rdd/Pages/default.aspx`

[3] CONCA, James. Terrorism In Brussels Shadowed By Dirty Bomb Plans. *Forbes* [online]. 2016 [cit. 2017-05-13]. Link: `https://www.forbes.com/sites/jamesconca/2016/03/29/terrorism-in-brussels-shadowed-by-dirty-bomb-plans/#16f64d562bef`

[4] BATCHELOR, Tom. TERROR WARNING: ISIS plotting dirty bomb attack on UK city using drones. *Express* [online]. 2016 [cit. 2017-05-13]. Link: `http://www.express.co.uk/news/uk/739710/Terror-warning-ISIS-plotting-dirty-bomb-attack-UK-city-using-drones`

[5] FERGUSON, Charles D., Tahseen KAZI and Judith PERERA. *Commercial Radioactive Sources: Surveying the Security Risks* [online]. Occasional paper No. 11. Monterey, California: Monterey Institute of International Studies, Center for Nonproliferation Studies, 2003 [cit. 2017-05-13]. Link: `https://www.nonproliferation.org/wp-content/uploads/2016/09/op11.pdf`

[6] MORELANDE, Mark R. and Branko RISTIC. Radiological Source Detection and Localisation Using Bayesian Techniques. *IEEE Transactions on Signal Processing* [online]. 2009, 57(11), 4220-4231 [cit. 2017-05-13]. DOI: 10.1109/TSP.2009.2026618. ISSN 1053-587x. Link: `http://ieeexplore.ieee.org/document/5153354/`

[7] GUNATILAKA, Ajith, Branko RISTIC and Ralph GAILIS. On Localisation of a Radiological Point Source. *2007 Information, Decision and Control* [online]. IEEE, 2007, 57(11), 236-241 [cit. 2017-05-13]. DOI: 10.1109/IDC.2007.374556. ISBN 1-4244-0901-2. ISSN 1053-587x. Link: `http://ieeexplore.ieee.org/document/4252508/`

[8] SULLIVAN, Clair J. Radioactive source localization in urban environments with sensor networks and the Internet of Things. *2016 IEEE International Conference on Multisensor Fusion and Integration for Intelligent Systems (MFI)* [online]. IEEE, 2016, 57(11), 384-388 [cit. 2017-05-13]. DOI:

10.1109/MFI.2016.7849518. ISBN 978-1-4673-9708-7. ISSN 1053-587x. Link: http://ieeexplore.ieee.org/document/7849518/

[9] HITE, Jason M., John K. MATTINGLY, Kathleen L. SCHMIDT, Razvan STEFANESCU and Ralph SMITH. Bayesian metropolis methods applied to sensor networks for radiation source localization. *2016 IEEE International Conference on Multisensor Fusion and Integration for Intelligent Systems (MFI)* [online]. IEEE, 2016, 57(11), 389-393 [cit. 2017-05-13]. DOI: 10.1109/MFI.2016.7849519. ISBN 978-1-4673-9708-7. ISSN 1053-587x. Link: http://ieeexplore.ieee.org/document/7849519/

[10] HARTMAN, Jessica, Alexander BARZILOV and Ivan NOVIKOV. Remote sensing of neutron and gamma radiation using aerial unmanned autonomous system. *2015 IEEE Nuclear Science Symposium and Medical Imaging Conference (NSS/MIC)* [online]. IEEE, 2015, 57(11), 1-4 [cit. 2017-05-13]. DOI: 10.1109/NSSMIC.2015.7581763. ISBN 978-1-4673-9862-6. ISSN 1053-587x. Link: http://ieeexplore.ieee.org/document/7581763/

[11] ALEOTTI, Jacopo, Giorgio MICCONI, Stefano CASELLI, et al. Unmanned aerial vehicle equipped with spectroscopic CdZnTe detector for detection and identification of radiological and nuclear material. *2015 IEEE Nuclear Science Symposium and Medical Imaging Conference (NSS/MIC)* [online]. IEEE, 2015, 57(11), 1-5 [cit. 2017-05-13]. DOI: 10.1109/NSSMIC. 2015.7582264. ISBN 978-1-4673-9862-6. ISSN 1053-587x. Link: http://ieeexplore.ieee.org/document/7582264/

[12] JOSHI, Tenzing, Brian QUITER, Jonathan MALTZ, et al. Measurement of the Energy-Dependent Angular Response of the ARES Detector System and Application to Aerial Imaging. *IEEE Transactions on Nuclear Science* [online]. IEEE, 2015, 57(11), 1-1 [cit. 2017-05-13]. DOI: 10.1109/TNS.2017.2693988. ISBN 978-1-4673-9862-6. ISSN 0018-9499. Link: http://ieeexplore.ieee.org/document/7898808/

[13] CORTEZ, R., Xanthi PAPAGEORGIOU, Herbert TANNER, Alexei KLIMENKO, Konstantin BOROZDIN, Ron LUMIA and William PRIEDHORSKY. Smart radiation sensor management. *IEEE Robotics* [online]. IEEE, 2008, 15(3), 85-93 [cit. 2017-05-13]. DOI: 10.1109/MRA.2008.928590. ISBN 978-1-4673-9862-6. ISSN 1070-9932. Link: http://ieeexplore.ieee.org/document/4624587/

[14] DUCKWORTH, Dexter, Brandon SHREWSBURY and Robin MURPHY. Run the robot backward. *2013 IEEE International Symposium on Safety, Security,*

*and Rescue Robotics (SSRR)* [online]. IEEE, 2013, 15(3), 1-6 [cit. 2017-05-13]. DOI: 10.1109/SSRR.2013.6719372. ISBN 978-1-4799-0880-6. ISSN 1070-9932. Link: `http://ieeexplore.ieee.org/document/6719372/`

[15] KNOLL, Glenn F. *Radiation Detection and Measurement*. 3rd edition. Michigan: John Wiley & Sons, 2000, 802 p. ISBN 04-710-7338-5.

[16] AHMED, Syed Naeem. *Physics and engineering of radiation detection*. London: Academic Press, 2007. ISBN 978-0-12-045581-2.

[17] ULLMANN, Vojtěch. *Jaderná fyzika a fyzika ionizujícího záření* [online]. 2015 [cit. 2015-03-12]. Link: `http://astronuklfyzika.cz/Fyzika-NuklMed.htm`

[18] X-rays for Diagnosis. *Medical Physics Course Notes* [online]. 1995 [cit. 2017-01-06]. Link: `http://img.chem.ucl.ac.uk/www/kelly/medicalxrays.htm`

[19] SMITH, David S. and Michael G. STABIN. Exposure Rate Constants and Leas Shielding Values for over 1,100 Radionuclides. *Health Physics* [online]. IEEE, 2012, 102(3), 271-291 [cit. 2017-05-13]. DOI: 10.1097/HP.0b013e318235153a. ISBN 978-1-4799-0880-6. ISSN 0017-9078. Link: `http://www.doseinfo-radar.com/Exposure_Rate_Constants_and_Lead_Shielding_Values%204.pdf`

[20] NAPPI, Eugenio and Vladimir PESKOV. *Imaging gaseous detectors and their applications.* Michigan: John Wiley & Sons, 2013, 356 p. ISBN

[21] Photocathode technology. *Hamatsu Photonics* [online]. 2016 [cit. 2017-01-06]. Link: `https://www.hamamatsu.com/eu/en/technology/innovation/photocathode/index.html`

[22] SCHRAGE, Chris, Nathan SCHEMM, Sina BALKIR, Michael W. HOFFMAN and Mark BAUER. A Low-Power Directional Gamma-Ray Sensor System for Long-Term Radiation Monitoring. *IEEE Sensors Journal* [online]. 2013, 13(7), 2610-2618 [cit. 2017-05-13]. DOI: 10.1109/JSEN.2013.2258009. ISSN 1530-437x. Link: `http://ieeexplore.ieee.org/document/6497463/`

[23] ŽALUD, Luděk, Tomáš JÍLEK and Petra KOCMANOVÁ. Robotic Autonomous Field Gamma Radiation Measurement for Environmental Protection. *Recent Advances on Energy and Environment* [online]. 2015, 69–76 [cit. 2017-05-13]. Link: `http://www.wseas.us/e-library/conferences/2015/Budapest/EE/EE-09.pdf`

[24] *Trimble BX982: Dual Antenna GNSS Module for Precise Position and Heading Applications* [online]. Trimble Navigation Limited, 2016 [cit. 2017-05-13]. Link: http://intech.trimble.com/library/DS_BX982_US.pdf

[25] NMEA-0183 message: GGA. *Trimble BD9xx GNSS Receivers Help* [online]. 2017 [cit. 2017-01-06]. Link: https://www.trimble.com/OEM_ReceiverHelp/V4.44/en/NMEA-0183messages_GGA.html

[26] NMEA-0183 message: PTNL,AVR. *Trimble BD9xx GNSS Receivers Help* [online]. 2017 [cit. 2017-01-06]. Link: https://www.trimble.com/OEM_ReceiverHelp/V4.44/en/NMEA-0183messages_PTNL_AVR.html

[27] NUVIA. Product Catalogue. [online]. 2016 [cit. 2017-03-27]. Link: http://www.nuvia.co.uk/_includes/docs/Nuclear-Measurements-Catalogue.pdf

[28] MCB3: Uživatelský manuál. *NUVIA a.s.*. Version 0.95.0.

[29] JÍLEK, Tomáš. *Pokročilá navigace v heterogenních multirobotických systémech ve vnějším prostředí*: PhD thesis. Brno: Brno University of Technology, Faculty of electrical Engineering and Communication, Department of Control and Instrumentation, 2015. 176 p. Supervised by doc. Ing. Luděk Žalud, Ph.D.

[30] *Department of Defense World Geodetic System 1984: Its Definition and Relationships with Local Geodetic Systems* [online]. Third edition. U. S. Department of Defense, 2000 [cit. 2017-05-13]. Link: http://earth-info.nga.mil/GandG/publications/tr8350.2/wgs84fin.pdf

[31] WILHELM, Emilien, Sebastien GUTIERREZ, Nicolas ARBOR, Stephanie MENARD and Abdel-Mjid NOURREDDINE. Study of different filtering techniques applied to spectra from airborne gamma spectrometry. *2015 4th International Conference on Advancements in Nuclear Instrumentation Measurement Methods and their Applications (ANIMMA)* [online]. IEEE, 2015, 1-5 [cit. 2017-05-13]. DOI: 10.1109/ANIMMA.2015.7465616. ISBN 978-1-4799-9918-7. Link: http://ieeexplore.ieee.org/document/7465616/

[32] JILEK, Tomas. Radiation intensity mapping in outdoor environments using a mobile robot with RTK GNSS. *International Conference on Military Technologies (ICMT) 2015* [online]. IEEE, 2015, , 1-7 [cit. 2017-05-13]. DOI: 10.1109/MILTECHS.2015.7153755. ISBN 978-8-0723-1977-0. Link: http://ieeexplore.ieee.org/document/7153755/

[33] Calculate distance, bearing and more between Latitude/Longitude points. *Movable Type* [online]. Cambridge, 2017 [cit. 2017-05-13]. Link: http://www.movable-type.co.uk/scripts/latlong.html

[34] WILLIAMS, David R. *Earth Fact Sheet* [online]. NASA Space Science Data Coordinated Archive, 2016 [cit. 2017-05-13]. Link: https://nssdc.gsfc.nasa.gov/planetary/factsheet/earthfact.html

[35] KOČANDRLE, Milan and Leo BOČEK. Matematika pro gymnázia. 3. vyd. Praha: Prometheus, 2009. Učebnice pro střední školy (Prometheus). ISBN 978-807196-390-5.

[36] AMIDROR, Isaac. Scattered data interpolation methods for electronic imaging systems: a survey. *Journal of Electronic Imaging* [online]. 2002, 11(2), 157–176 [cit. 2017-03-27]. Link: http://molly.magic.rit.edu/~mac/test/paper_pdf.pdf

[37] EBERLY, David. Least Squares Fitting of Data. *Geometric Tools* [online]. 2016 [cit. 2017-03-27]. Link: http://www.geometrictools.com/Documentation/LeastSquaresFitting.pdf

[38] 3D least squares regression parabolic fit problem. *MATLAB Central* [online]. 2017 [cit. 2017-01-06]. Link: https://www.mathworks.com/matlabcentral/newsreader/view_thread/70368

[39] UHER, J., C. FROJDH, J. JAKUBEK, S. POSPISIL, G. THUNGSTROM a Z. VYKYDAL. Directional radiation detector. *2007 IEEE Nuclear Science Symposium Conference Record* [online]. IEEE, 2007, , 1162-1165 [cit. 2017-05-13]. DOI: 10.1109/NSSMIC.2007.4437213. ISBN 978-1-4244-0922-8. Link: http://ieeexplore.ieee.org/document/4437213/

[40] Fitting of a Polynomial using Least Squares Method. *Neutrium* [online]. 2015 [cit. 2017-05-13]. Link: https://neutrium.net/mathematics/least-squares-fitting-of-a-polynomial/

[41] Find local maxima: MATLAB findpeaks. *MATLAB Documentation* [online]. 2017 [cit. 2017-05-13]. Link: https://www.mathworks.com/help/signal/ref/findpeaks.html

[42] BANDARA, Ravimal. *Check if a Point is Inside the Polygon Using Ray-Casting Algorithm* [online]. CodeProject, 2013 [cit. 2017-05-14]. Link: https://www.codeproject.com/Tips/626992/Check-if-a-Point-is-Inside-the-Polygon-Using-Ray-C

[43] BUCZYK, Biyeun. *Poisson Distribution of Radioactive Decay* [online]. MIT Department of Physics, 2009 [cit. 2017-05-13]. Link: https://stuff.mit.edu/afs/sipb/user/biyeun/Public/8.13/poisson/poisson_statistics_biyeun.pdf

[44] DINOV, Ivo D. *Normal Approximation to Poisson(λ) Distribution* [online]. Departments of Statistics and Neurology, UCLA School of Medicine, 2015 [cit. 2017-05-13]. Link: http://socr.ucla.edu/Applets.dir/NormalApprox2PoissonApplet.html

[45] LAZNA, Tomas, Tomas JILEK, Petr GABRLIK a Ludek ZALUD. Multi-robotic Area Exploration for Environmental Protection. *8th International Conference on Industrial Applications of Holonic and Multi-Agent Systems HoloMAS 2017*. 2017

[46] WAGENAAR, Douglas J. Radioactive Decay. *Radiation Physics Principles* [online]. 1995 [cit. 2017-05-13]. Link: http://www.med.harvard.edu/jpnm/physics/nmltd/radprin/sect2/2.2/2_2.1.html

[47] LAURIDSEN, Bente. *Table of Exposure Rate Constants and Dose Equivalent Rate Constants* [online]. Technical University of Denmark, 1982 [cit. 2017-05-13]. Link: http://orbit.dtu.dk/files/56550773/ris_m_2322.pdf

# LIST OF ABBREVIATIONS

| | |
|---|---|
| ADC | Analog-to-digital converter |
| APD | Avalanche photodiode |
| ASCII | American Standard Code for Information Interchange |
| BS | Base station |
| CBRN | Chemical, biological, radiological and nuclear (defense) |
| Co | Cobalt |
| CPS | Counts per second |
| Cs | Caesium |
| GLONASS | Globalnaja navigacionnaja sputnikovaja sistěma |
| GM | Geiger-Müller |
| GNSS | Global navigation satallite system |
| GPS | Global Positioning System |
| HV | High voltage |
| IP | Internet Protocol |
| LLD | Lower level discriminator |
| LSB | Least significant byte |
| MCB | Multi-channel buffer |
| NaI(Tl) | Thallium doped soudium iodide |
| NMEA | National Marine Eelectronics Association |
| PD | Photodiode |
| PLA | Polyactid acid |
| PMT | Photomultiplier tube |
| RTK | Real Time Kinematic |
| TCP | Transmission Control Protocol |
| UAV | Unmanned aerial vehicle |
| UDP | User Datagram Protocol |
| ULD | Upper level discriminator |
| USB | Universal Seriál Bus |
| UTC | Coordinated Universal Time |
| WGS-84 | World Geodetic System 1984 |
| XML | Extensible Markup Language |
| XOR | Exclusive or |

# LIST OF APPENDICES

# A SAMPLE CONFIGURATION XML FILE

```
<?xml version="1.0" encoding="utf-8"?>

<radiation-config>
  <system-type>TwoDetector</system-type>
  <measurement-mode>Circle3</measurement-mode>
  <detector-config>
    <type>Main</type>
    <ip-address>10.0.70.100</ip-address>
    <port>17000</port>
    <high-voltage>605</high-voltage>
  </detector-config>
  <detector-config>
    <type>Secondary</type>
    <ip-address>10.0.70.101</ip-address>
    <port>17000</port>
    <high-voltage>505</high-voltage>
    <sensitivity>1.05</sensitivity>
  </detector-config>
  <timer-config>
    <measurement-period>1000</measurement-period>
    <measurement-time>1800</measurement-time>
  </timer-config>
  <gnss-config>
    <used>Yes</used>
    <port>8000</port>
    <update-rate>10</update-rate>
    <yaw-correction>-30</yaw-correction>
  </gnss-config>
  <meas-trajectory>
    <base-station>49.2284253,16.5715689</base-station>
    <polygon>
      <vertex>49.2280794023,16.5721840078</vertex>
      <vertex>49.2283073013,16.5719443535</vertex>
      <vertex>49.228389255,16.5719478359</vertex>
      <vertex>49.2284094344,16.5719942793</vertex>
      <vertex>49.2283392136,16.5720838814</vertex>
      <vertex>49.228327559,16.5721530872</vertex>
```

```
      <vertex>49.2281781275,16.5723155872</vertex>
    </polygon>
    <line-sep>1</line-sep>
    <waypoint-sep>0.6</waypoint-sep>
  </meas-trajectory>
  <navigation-config>
    <id>RD</id>
    <ip-address>127.0.0.1</ip-address>
    <port>18000</port>
    <nav-error>0.05,0.05</nav-error>
  </navigation-config>
  <circle-alg-params>
    <circles>
      <circle>
        <center>49.2281673,16.5722046</center>
        <radius>4</radius>
      </circle>
      <circle>
        <center>49.2282533,16.5721232</center>
        <radius>4</radius>
      </circle>
      <circle>
        <center>49.2283381,16.5720061</center>
        <radius>3.5</radius>
      </circle>
    </circles>
    <data-source>Both</data-source>
    <peak-threshold>0.8</peak-threshold>
    <peak-shift>-0.2</peak-shift>
    <peak-angular-prominence>20</peak-angular-prominence>
    <dir-prominence>1.1</dir-prominence>
    <yaw-change-deg>9</yaw-change-deg>
    <radius>1.5</radius>
    <loop-threshold>0.5</loop-threshold>
  </circle-alg-params>
</radiation-config>
```

# B CALIBRATION PROTOCOL

## Protokol o přejímací zkoušce URZ

Číslo protokolu: 92/13 Datum vystavení protokolu: 12.12.2013

| | |
|---|---|
| Název a adresa zkušební instituce:<br>IČ:<br>Číslo povolení:<br>Platnost do: | Eckert & Ziegler Cesio s.r.o.<br>Radiová 1, 102 27 Praha 10<br>45274584<br>SÚJB/OEHO/24466/2013<br>doba neurčitá |
| Název a adresa majitele zářiče: | Vysoké učení technické v Brně<br>Fakulta elektrotechniky a komunikačních technologií, Technická 3082/12, 616 00 Brno |
| Údaje o zkoušeném URZ:<br>Výrobce:<br>Typ zářiče:<br>Výrobní číslo:<br>Rok výroby:<br>Číslo osvědčení:<br>Druh radionuklidu:<br>Aktivita: | <br>Eckert & Ziegler Cesio s.r.o., Česká republika<br>A3015<br>CZ 4949<br>2013<br>118113<br>$^{60}$Co<br>100 MBq k 5.12.2013 |
| Dokumentace předložená ke zkoušce: | Podklady k osvědčení URZ č. 118113 |
| Zkušební postup (ISO 9978):<br>povrchová kontaminace URZ:<br>těsnost URZ:<br>vizuální zkouška: | výsledek: datum: soulad s požadavky:<br>< 10 Bq 11.12.13 ano-~~ne~~<br>< 10 Bq 11.12.13 ano-~~ne~~<br>vyhovuje 11.12.13 ano-~~ne~~ |
| Doporučení k provádění zkoušek dlouhodobé stability: | Zkouška se podle vyhlášky SÚJB č.307/2002 Sb. § 71odstavec 4 ve znění pozdějších předpisů **neprovádí** |
| Doporučení k provádění zkoušek provozní stálosti:<br>Rozsah zkoušky:<br>Interval provádění:<br>Záznam: | <br>Těsnost a povrchová kontaminace otěrem za vlhka<br>1 x za 3 měsíce<br>Protokol o zkoušce provozní stálosti |
| Použité přístroje a pomůcky (čísla ověřovacích listů): | CAPINTEC, INC., USA, výr. č. 252201<br>ověřovacího list č.: 9051-SM-U8335/2012 |
| Poznámky: URZ je klasifikován jako drobný zdroj ionizujícího záření.<br>Typové schválení SÚJB /OEHO/16906/2011.<br>Pro uživatele platí ohlašovací povinnost ve smyslu ust. § 21 a 22 zákona č. 18/1997 Sb. v platném znění. | |
| Výsledek přejímací zkoušky: | ☒ soulad s požadavky<br>☐ nesoulad s požadavky |
| Přejímací zkoušku provedl: | Ing. Věra Knězová |
| Podpis statutárního orgánu: | Ing. Ivan Šimmer<br>Eckert & Ziegler Cesio s.r.o.<br>Radiová 1, 102 27 Praha 10<br>DIČ: CZ45274584 |

# C ENCLOSED CD CONTENT

- `/` ..... root of the enclosed CD
  - `control software`
    - `RadiationController.sln` ..... VS solution of the control software
    - `RadiationController` ..... source codes
      - `config` ..... sample configuration files
      - `lib` ..... included libraries
  - `data processing`
    - `dataLog.csv` ..... sample data from real experiment
    - `main.m` ..... executable MATLAB script
  - `models` ..... SketchUp 3D models of mounting for detectors
    - `mounting_parts.skp` ..... model for 3D print
    - `mounting_assembly.skp` ..... final assembly
  - `text` ..... LaTeX source codes
    - `images` ..... all images included in thesis
    - `pdf` ..... included PDFs
    - `text` ..... individual parts of the thesis
    - `sablona-prace.tex` ..... main TeX document
  - `lazna_tomas_2017.pdf` ..... electronic version of this document